A Linear Electromagnetic Piston Pump

A Thesis
SUBMITTED TO THE FACULTY OF
UNIVERSITY OF MINNESOTA
BY

Paul H. Hogan

IN PARTIAL FULFILLMENT OF THE REQUIREMENTS
FOR THE DEGREE OF
MASTER OF SCIENCE

Dr. James D. Van de Ven

June 2017

Acknowledgements

I would like to acknowledge my advisor, Jim Van de Ven, for his continuous support throughout my research and time at Minnesota. Whenever I hit challenging spots with my work and got flustered, Jim was calm and collected and made helpful suggestions to keep me on track and making progress. I looked forward to our weekly meetings as a chance to catch up and share what progress, big or small, I'd made.

I would also like to acknowledge the other students in MEPS. Through several presentations and much time spent in the lab, I had the chance to learn a lot from all of you. I got some amazing feedback in those sessions and can only hope that I was able to do the same in return.

Thank you to Eric Severson for the help he offered a newbie in the world of electromagnetics. He was always patient with a range of questions, some better than others, and I appreciate all the help and encouragement he offered along the way.

Thank you to all the staff of the ME department for all you do under the scenes and for the help you've provided countless students, ranging from purchasing and payroll to graduate advising and reassuring me that I've hit all the requirements to graduation.

Thank you to Advanced Motion Controls for donating a servo drive to power the linear motor in my experimental setup. They were also very responsive and helpful with all of my emails asking for help on setup and troubleshooting.

Thank you also to the Minnesota Supercomputing Institute for runtime on the Mesabi supercomputing cluster for my optimization code.

Finally, thank you to my brother and my parents for all the support you've provided. I couldn't imagine this undertaking without you all by my side, and I appreciate it every step of the way.

Abstract

Advancements in mobile hydraulics for human-scale applications have increased demand for a compact hydraulic power supply. Conventional designs couple a rotating electric motor to a hydraulic pump, which increases the package volume and requires several energy conversions. This thesis investigates the use of a free piston as the moving element in a linear motor to eliminate multiple energy conversions and decrease the overall package volume.

A coupled model used a quasi-static magnetic equivalent circuit to calculate the motor inductance and the electromagnetic force acting on the piston. The force was an input to a time domain model to evaluate the mechanical and pressure dynamics. The magnetic circuit model was validated with finite element analysis and an experimental prototype linear motor. The coupled model was optimized using a multi-objective genetic algorithm to explore the parameter space and maximize power density and efficiency. An experimental prototype linear pump coupled pistons to an off-the-shelf linear motor to validate the mechanical and pressure dynamics models.

The magnetic circuit force calculation agreed within 3% of finite element analysis, and within 8% of experimental data from the unoptimized prototype linear motor. The optimized motor geometry also had good agreement with FEA; at zero piston displacement, the magnetic circuit calculates optimized motor force within 10% of FEA in less than 1/1000 the computational time. This makes it well suited to genetic optimization algorithms. The mechanical model agrees very well with the experimental piston pump position data when tuned for additional unmodeled mechanical friction.

Optimized results suggest that an improvement of 400% of the state of the art power density is attainable with as high as 85% net efficiency. This demonstrates that a linear electromagnetic piston pump has potential to serve as a more compact and efficient supply of fluid power for the human scale.

Table of Contents

List of Tables

List of Figures

1 Introduction

In recent years, advances in technologies ranging from hydraulically-assisted prostheses to human-scale robotics have demanded increased power density and efficiency in hydraulic power generation and delivery. Hydraulic actuators have a distinct advantage over electric actuators at the human-scale due to their force and power density, but electric energy storage remains superior in many applications. As such, mobile hydraulic systems require efficient electric-to-hydraulic conversion at human-scale power in a compact package. In this work, a linear electromagnetic piston pump is presented. This technology converts electric energy to hydraulic energy directly by applying an electromagnetic force to a piston. To properly understand the dynamics and system performance of such a pump, a dynamic coupled model was developed that combines quasi-static electromagnetic force generation with mechanical and pressure dynamic equations.

This introductory chapter will begin with a background section to introduce the reader to the linear electromagnetic piston pump concept and to provide motivation for the study of electric-to-hydraulic energy conversion. It will next include a literature review that examines other examples of electric to hydraulic energy conversions, targeting 100 to 1,000 W of output power. Prior work ranges from mobile hydraulic power units that couple a rotating electric motor to a conventional piston pump, to novel piezoelectrically actuated and linear motor-based piston pumps. The chapter will conclude with an overview of the topics covered in this thesis.

1.1 Background

Due to the high force density of hydraulic actuators, they are seeing increased usage at the human-scale of power, defined as 100 W to 1 kW. This scale is often associated with robotics and prosthetics. For such applications to be viable in uses ranging from rescue and military missions to recovering the quality of life for amputees, systems tethered to a centralized power station are impractical. The power supply must be carried along with the device, whether it be an ankle-foot orthosis or a humanoid robot.

Since the volume and mass is critical in these applications, maximum power density is a must.

For example, the ATLAS robot developed by Boston Dynamics is a humanoid comparable in size to a human. For its motion, ATLAS relies on extremely compact and power dense hydraulic actuation. The demands are so great that the robot uses "3D-printed, integrated hydraulic actuators" developed by Moog for increased compactness [1]. These are driven by a variable-pressure electrically-driven pump connected to a 3.7 kW-hr lithium-ion battery pack [2]. While the hydraulic actuators are making leaps and bounds in increased power density through the use of additive manufacturing techniques and creative design, there is little indication that the hydraulic power supplies used in the ATLAS are following a similar trajectory.

Along similar lines, academic research is studying the use of hydraulic actuators for medical applications like an ankle foot orthosis [3] or powered prostheses [4]. Passive prostheses exist, which recycle energy from the user by using spring-damper systems, but research suggests that patients walking with these systems require as much as 60% more metabolic energy than healthy subjects [5]. Powered systems are able to rectify this deficiency. However, any extra bulk in the hydraulic power units powering these devices will literally weigh down the user, so maximizing power density and compactness are necessary in component sizing. Additional weight at an extremity results in asymmetries in patient gait, and, depending on placement of active prosthesis mass, the metabolic cost could go up by 5% to 12% [6].

Typical conversion of electric to hydraulic energy takes advantage of modularity in component specification. Hydraulic pumps require a delivery of torque to an input shaft, and this is generally supplied by a rotating electric motor. Such a process requires multiple energy conversions, as depicted in Figure 1. First, electric energy is converted into rotational shaft energy within the electric motor. Rotating electric machinery reaches peak efficiencies at high angular speeds, which are generally too large for human powered machinery. This requires a gear reduction or a lower efficiency operating point. Next, power is transferred via the shaft into the hydraulic pump. Within the pump, some

sort of mechanism is required to convert the rotating mechanical energy into the oscillating motion of a piston (or other pump mechanism) that generates hydraulic energy. This configuration can be easy to design, and is often specified with components from multiple venders. However, for this same reason it can be needlessly bulky, and the additional energy conversions introduce losses. Each mechanical energy conversion also introduces a potential for wear and friction, such as within the pin connections of a linkage or the rolling contact of bearings. In addition, bulky and complex conversions can be noisy. This is also detrimental to the quality of a device, particularly in medical device applications.

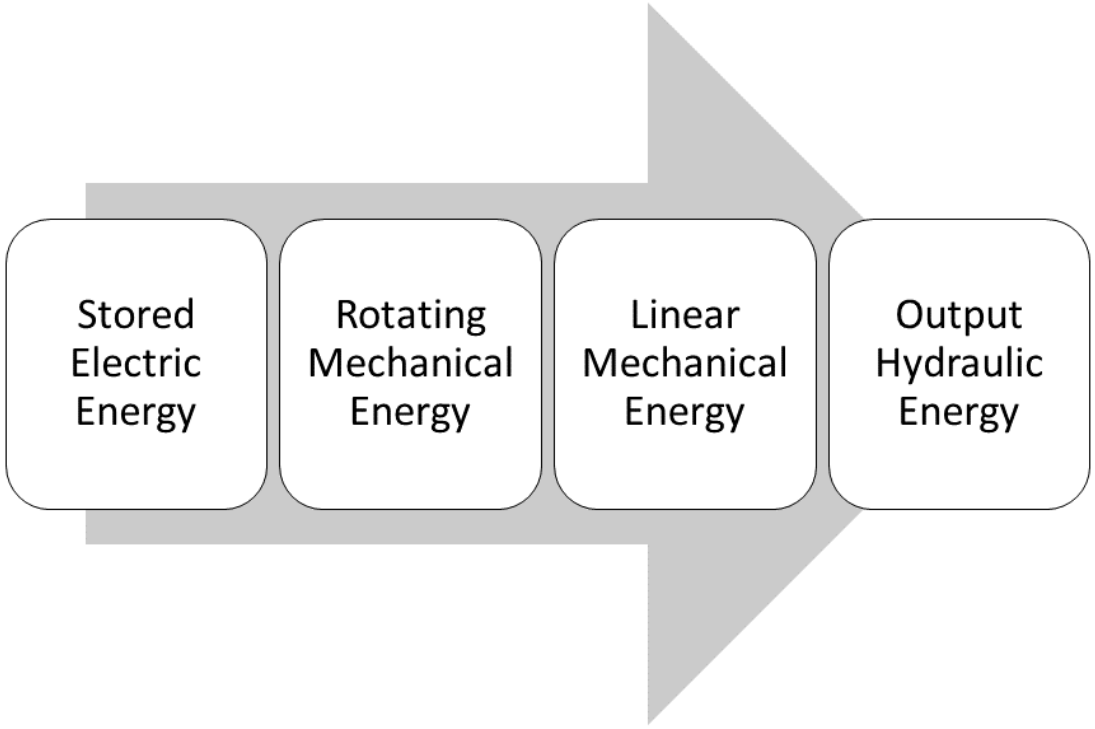

Figure 1: State of the art for electric-to-hydraulic energy conversion

In a market that places increasingly high demands on compact and efficient delivery of fluid power, an improved method for hydraulic power generation is needed. This thesis attempts to decrease conversion losses and reduce package volume by removing as many energy conversions as possible. The intermediate rotating mechanical energy domain is removed by applying an electromagnetic force directly to the piston, as

opposed to a rotating shaft. This eliminates losses associated with converting the rotation of a shaft into the timed oscillation of multiple pistons. Bypassing this conversion also eliminates the need for gear reductions or a crankshaft, which could each increase the volume and weight of the hydraulic power unit. By using the piston itself as the moving element in a linear motor, the hydraulic output energy is generated within the package volume of the electric motor. The linear electric motor and the hydraulic pump together become one compact component instead of the modularized two-component systems found in the state of the art. This design allows for more compact and direct conversion of electric to hydraulic energy.

Figure 2 presents the general concept of the directly driven linear electromagnetic piston pump. The pump consists of a moving-magnet type linear motor that pumps chambers on either side of the piston. Return springs allow operation at a mechanical resonance defined by the moving mass and spring constants. The cylinder sleeves are the bearings for the linear motor. Operation of multiple double-ended cylinder units in parallel would increase power output and reduce flow ripple. In addition, with multiple units, the net output could be varied to allow a continuously variable output while individual units operate at their most efficient resonant conditions.

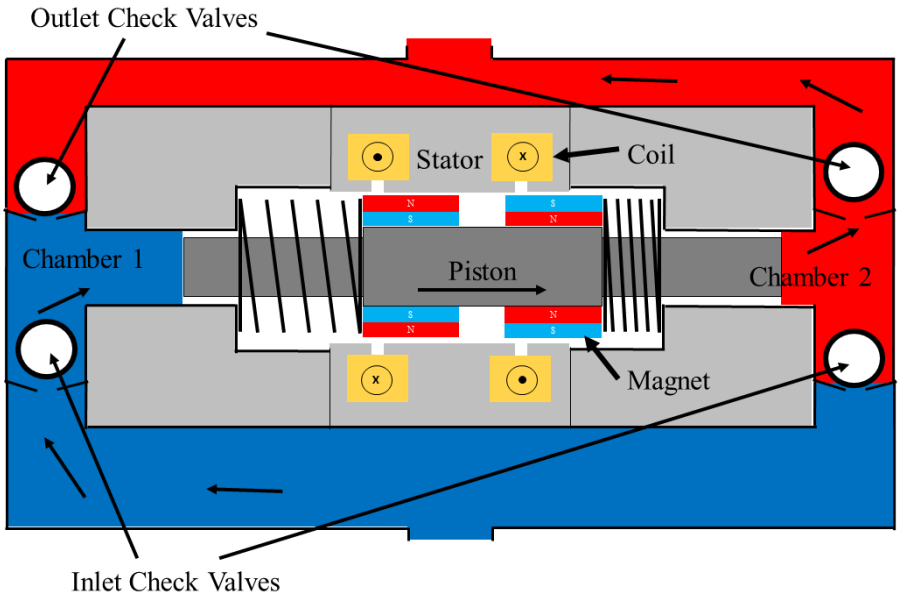

Figure 2: Linear electromagnetic piston pump concept.

Proper understanding of the mechanics of the linear electromagnetic piston pump requires a model that accurately accounts for both the electromagnetic and mechanical aspects of the pump motion. The dynamic model couples the quasi-steady state force-vs-displacement profile of the actuator to a time-domain solution of the mechanical and pressure dynamics equations. The variables used as inputs to the coupled model include the geometry of the linear motor, the piston diameter, the spring constant, and the driving frequency.

1.2 Literature Review

Mobile hydraulic power units at the human-scale of power already exist in many forms, and research is continuously being done to increase their power output, compactness, and efficiency. As a result, a number of different designs have been put forward in the literature. This literature review will attempt to cover recent developments in academic research and industry products for mobile hydraulic power supplies. The review is divided into four parts to cover different approaches to generating flow. First, mobile hydraulic power units that incorporate a rotating electric motor with a compact hydraulic pump will be covered. Second, research in piezoelectrically actuated pumps,

also known as piezo pumps will be discussed. Third, linear motor-driven cryocooler compressors will be presented as an example of a moving magnet type linear motor driving a double-ended piston. Finally, some available off-the-shelf linear diaphragm pumps will be discussed along with their advantages and drawbacks.

1.1.1 Mobile Hydraulic Power Units

One application that sees hydraulic power usage at the human-scale is in ankle-foot orthosis (AFO). Passive devices simply recycle the patient's energy, which can be a simple solution. However, the fixed motion control of these devices can impede gait in certain times during the stepping cycle, limiting their effectiveness for many patients [7]. This has opened the door to active designs that use a power source to artificially support the ankle and provide additional strength in the case of deteriorated muscle groups. Many pneumatically-powered systems have been proposed, often using a compressed air supply such as in Shorter et al. [7] The advantage of hydraulic actuation in an active AFO is its high power density, assuming that either the operating pressure or system power are high enough, as shown in [8]. This permits a design that is lightweight and compact, while still providing ample system power. These active systems can improve the performance benefits for patients using an orthosis or prosthetic and provide a distinct advantage over passive systems, which simply recycle user energy but do not actively support a walking gait.

The Durfee group at University of Minnesota has researched a hydraulic powered AFO that incorporated a built-in hydraulic power supply for increased compactness, as documented in Neubauer et al. [3]. Their supply incorporated a DC brushless motor and controller connected through a gearbox and flexible coupler to an axial piston pump, as pictured in Figure 3. The system used a single 3300 mAh, 29.6 V battery to power the motor and electronics. The pump had a fixed displacement of 0.4 cc/revolution and had simulated output up to about 35 cc/sec, while the pressure was simulated up to about 117.2 bar (1700 psi). Experimental efficiency approached 45% at about 44.8 bar (650 psi). The power density was not reported, but was around 33 W/kg.

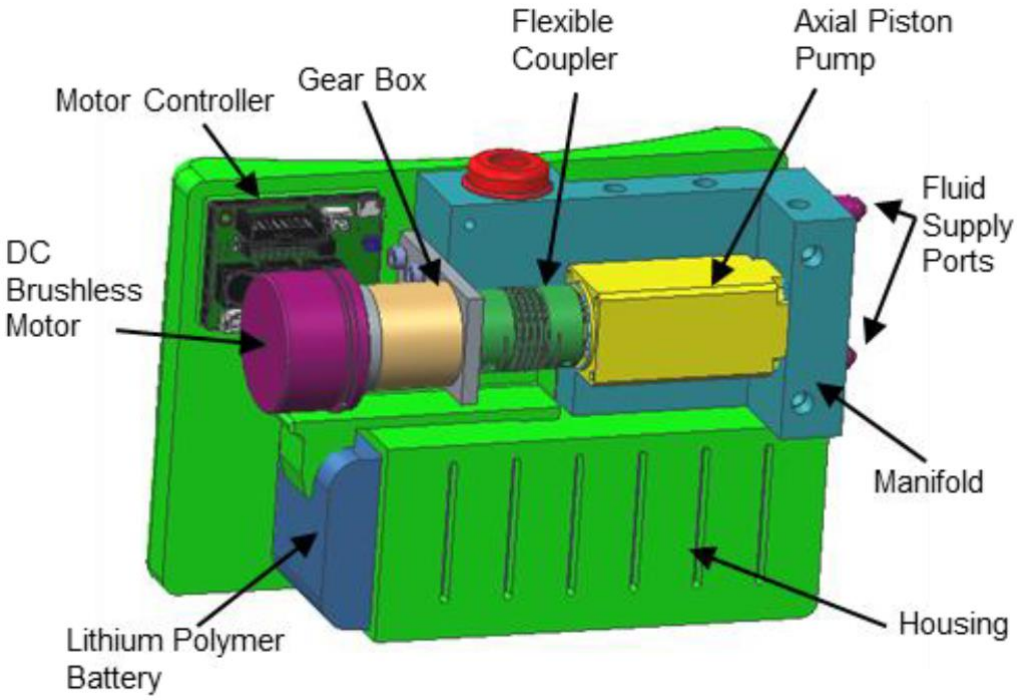

Figure 3: Hydraulic power supply used in AFO from Neubauer et al. [3]

Limited discussion in the paper is spent on the component specification for the power supply itself, but the system as a whole was designed based on a torque requirement for hydraulic assist at the ankle and a bound on maximum angular displacement. Each of these requirements was determined from medical studies of the mechanics of ankle motion. A fixed displacement axial piston pump was selected that could deliver the anticipated flowrate, which is dependent on the selection of hydraulic actuators and design requirements for ankle motion. Based on the selected pump, a motor and gearbox were paired based on a root-mean-squares approach to limit heat dissipation during intermittent motor operation. This modular component selection is more flexible than that offered by the linear electromagnetic piston pump concept in that a motor can in theory be paired with pumps of varying sizes to properly match the necessary load. However, this could result in diminished efficiency at lower output because the electric motor is oversized to the pump.

Other researchers have seized on the power density advantage of hydraulics in the realm of active medical devices. Yu et al. present an alternative prototype powered prostheses that utilized a 100 W nominal brushless DC motor to drive a 0.45 cc/rev fixed displacement gear pump [4]. Their integrated motor-pump unit increased compactness by decreasing the length of the shaft coupler and removing the gearbox found in the Neubauer design. The high-torque motor itself appears to be larger, although no details on package volume were presented.

The Yu design suffered from an inefficient conversion from motor output to pump output. For a test case of 162.8 W supplied, the motor was 93% efficient and outputted 151.8 W. This level of efficiency is typical in electric machinery. However, of the power delivered to the pump, only 77.7 W are delivered in hydraulic power, representing a conversion efficiency of just 51% in the pump alone. The overall efficiency from electric source to pump output was 47.7%. It is unclear whether these losses stem from mechanical or volumetric inefficiency.

A variety of designs are available off the shelf for human scale mobile hydraulic power supply. These designs use an electric motor coupled to a hydraulic pump. As one example, Concentric allows the designer to specify the motor and pump together, and the unit will be packaged into one “power pack” [9]. As far as modular designs go, the pump from Concentric makes a strong case for a compact design. The area taken up by the shaft coupling is miniscule, as the pump and motor are packaged adjacent to one another. Although not quoted explicitly, the power packs are roughly 0.15 W/cc power density at 1 hp output.

Hurst is a manufacturer of rescue spreaders, a hydraulically powered mechanism that is capable of delivering extremely high forces to pry open sealed metal spaces. Their most portable power supply, the P 600 OE, supplies 690 bar (10,000 psi) at between 0.64 lpm on the low setting to 2.4 lpm on the high setting. For a package volume of 21,500 cc, this equates to a power density of approximately 0.03 to 0.13 W/cc. Efficiency is not reported. The device is battery powered, with an option for wired power.

Based on this review, the advantage of coupling a rotating electric motor to a hydraulic pump is that it allows easy specification of a flowrate and integration with the rest of the hydraulic circuit. Each design presented above used a fixed-displacement pump coupled to a DC brushless motor, where the pump has been sized to the maximum flowrate demands of the system and the motor to the r.m.s. pressure demands of the system. The designs allowed the researchers to demonstrate proof-of-concept and reach benchmarks for component weight. The downside of utilizing a modularized hydraulic power supply was increased package bulk as a result of the motor and pump being two separate units. In the case of Yu et al., the conversion efficiency in the pump itself was also quite low.

1.1.2 Piezo Pumps

As mentioned above, the modularized hydraulic power supply can be quite bulky. This is due in large part to the pump and electric motor occupying different spaces in the overall package. In an attempt to package the pump and electric drive together, some researchers have turned to pumps driven by a piezoelectric stack, also known as “piezo pumps”. Piezoelectric materials experience a change in strain under an applied voltage. They are attractive candidates for driving pistons in pumping applications due to their very high blocking forces and actuation speeds; forces on the order of 70 kN and driving frequencies of 400 Hz are achievable, as simulated by Henderson et al. [10].

Chaudhuri et al. present a thorough review of piezo pumps [11]. They discuss a variety of designs with power output of up to 34 W, as well as the different techniques for modeling them. Since the strain rate of piezoelectric materials is so small, they must be combined in series to form a “piezo stack”. Even with such an arrangement, piston displacements were on the order of just 50-180 μm, which required very high frequencies to generate reasonable power output [11].

Recent piezo pump designs are starting to reach power output that is comparable to the human-scale. Henderson et al. have simulated piezo pump operation up to nearly 1 kW, which is at the upper range of what might be considered human-scale. Their schematic for a piezo pump utilizing passive check valves is pictured in Figure 4. This

piezo pump targeted high output power by taking advantage of very high piezoelectric blocking forces [10]. The piezo stack allowed a free (unloaded) displacement of 180 µm. Even with this relatively long displacement, by piezo stack standards, a high driving frequency was still required. This resulted in a deterioration in check valve performance because inefficiencies increased drastically at driving frequencies above 400 Hz [10]. According to Henderson et al., the losses at high frequencies were due to vortex formation at the outlet and finite valve response time resulting in greater pressure drops and flow reversal. Fluid inertia and valve resonance also played a role in reducing efficiency. Simulations nonetheless demonstrated power output up to 840 W at a 90 bar pressure rise. Although efficiency was not reported for this simulation, their introduction states that overall efficiencies for other cited designs were below 10%.

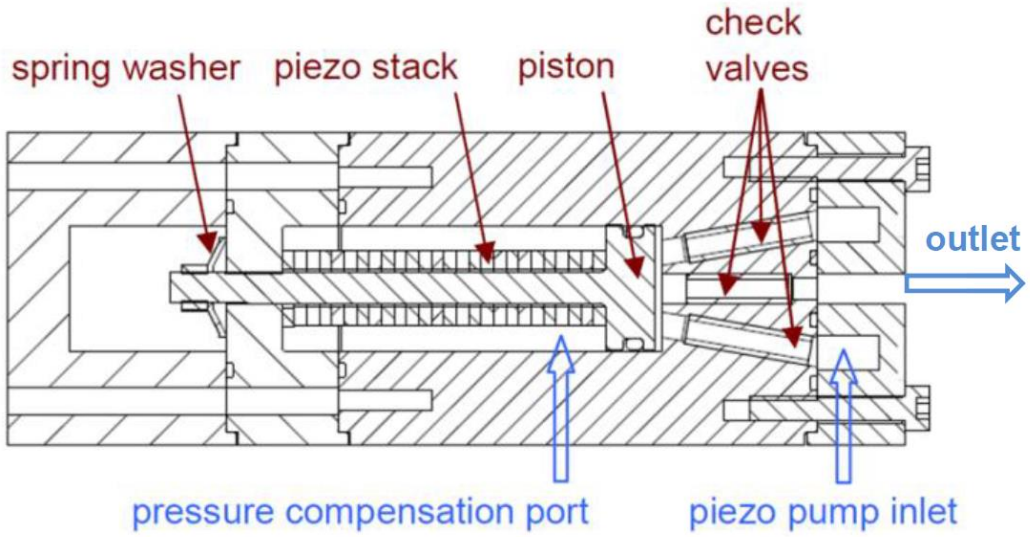

Figure 4: Piezo pump with passive check valves [10]

To avoid the issue of poor passive valve performance, Lee et al. studied the use of active valves in a piezo pump that uses piezoelectric unimorph disc valves [12]. Active valves allow timing independent of pressure, which lets the valves open and close at the ideal times to minimize backflow and transition losses. The unimorph disc valve is a metal disc with a piezoelectric layer which deforms under an applied voltage, thus deforming the metal disc and opening the valve. Instead of a sliding piston, this pump

used a piezo stack to actuate a moving diaphragm. Their study used a combination of static finite element analysis (FEA) and dynamic computational fluid dynamics (CFD) and FEA to study the detailed motion of the piezo-actuated diaphragm at driving frequencies as high as 20 kHz. The paper has ample documentation of the design concept and experimental prototype, as well as techniques for optimizing design parameters, but limited information on the actual pump performance. The authors claim a bandwidth up to 15 kHz without fluid, with volumetric flowrates of 3.4 cc/s, specific power density of 12 W/kg, and a stall pressure of 8.3 MPa.

Other groups have done similar work with active valving for piezo pumps. Tan et al. modeled the performance of a small-scale single-ended piezo pump with piezoelectric active valves and a bandwidth on the order of 1 kHz [13]. Their quasi-static steady flow model predicts peak pressures over 41 bar (600 psi) and power output on the order of 4 W. Their models agreed reasonably well with experimental measurements, particularly when predicting the driving frequency of peak power. No mention was made of modeled or experimental efficiency. For comparison, Cadou et al. modeled a similar piezo pump design with passive check valves using a quasi-static fluid model and estimated peak output of about 1 W and efficiency around 60% [14].

Piezo pumps show some promise as a hydraulic power source for human-scale mobile hydraulic applications. The piezo stack can extend and retract at very high frequencies and supplies high blocking forces, and therefore delivery pressures. Despite the low piston stroke, the high frequency operation theoretically enables the required flow rates. The challenge for piezo pumps remains valving and flow rectification at high frequencies. Initial work in active valves, particularly in piezoelectrically actuated valves that are capable of very fast response times, has shown promise for increasing the volumetric efficiency of these devices. However, piezo pumps to this point have demonstrated very low efficiencies. Improved volumetric efficiency and therefore power output are necessary to make piezo pumps a viable option for human-scale hydraulic power.

1.1.3 Linear Motor-Driven Cryocooler Compressors

Another field of research that has explored the use of compact pumps utilizing a linear motor for actuation is in pulse tube cryocoolers. These devices are used for cooling parts that behave as concentrated heat sources and must be maintained at low working temperatures, such as high performing electronics or superconductors. Since target applications are often mobile, such as military infrared sensors or spacecraft components, compactness and efficiency are design priorities [15]. A number of designs have been proposed, ranging from those in Karunanithi et al. [16] and Ruhlich et al. [17] that used an un-valved dual-piston, moving magnet style, to that in Wang et al. [18] which used a single-ended piston and reed valves.

Although the pulse tube cryocooler contains additional components for achieving refrigeration that are not relevant to this thesis, the heart of the device is a linear motor-driven piston pump, as in Figure 5. This linear motor driven compressor, presented by Karunanithi et al. [16], was used to supply an oscillating pressure to a “coldfinger,” a short rod which acts as a heat sink for the cooling target [17]. The linear motor driving this compressor used a moving radial magnet geometry with stationary, axisymmetric coils. Instead of springs and bearings located at either end of the compressor, the motor uses a C-shaped flexure, which is an aluminum bracket that restricts radial motion and generates a spring force in the axial direction. This permitted the motor to maintain the precise, small air gap that is required for high performance, while offering a means of energy recapture for efficient resonant operation. Based on experimental power factor results, the resonant frequency was about 29.5 Hz. The motor was driven by a 140 W, variable frequency PWM supply, and it was capable of actuator forces of over 15 N at 7

A of current [16].

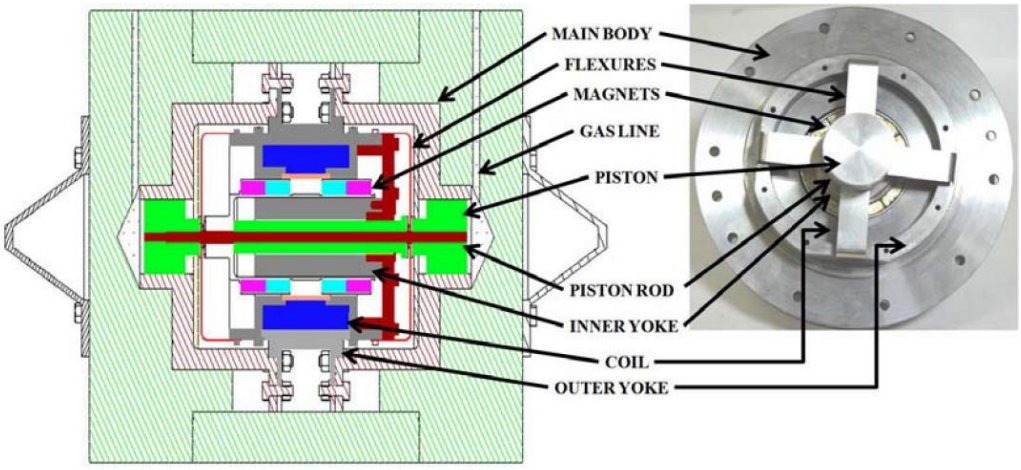

Figure 5: Schematic and image of a cryocooler compressor [16].

The compressor itself did not incorporate any valving, so the mean flow was zero [16]. Very few pump-related performance metrics are provided. However, the article provides a reasonable level of detail on construction of a prototype moving-magnet linear motor. This includes construction of the moving magnet yoke, assembly of the segmented radial magnets into a single approximate radial ring magnet, and the testing of the magnetic field around the moving magnets to compare with FEA predictions.

Ruhlich et al. present a similar compressor as part of an overall cryocooling system [17]. Their innovation on the compressor was to flip the pistons to face inwards, such that there is a single outlet in the center, as pictured in Figure 6. To increase compactness further, they used a spring instead of a flexure. This resulted in an increased cooling load per unit volume, which was their metric for cooling performance.

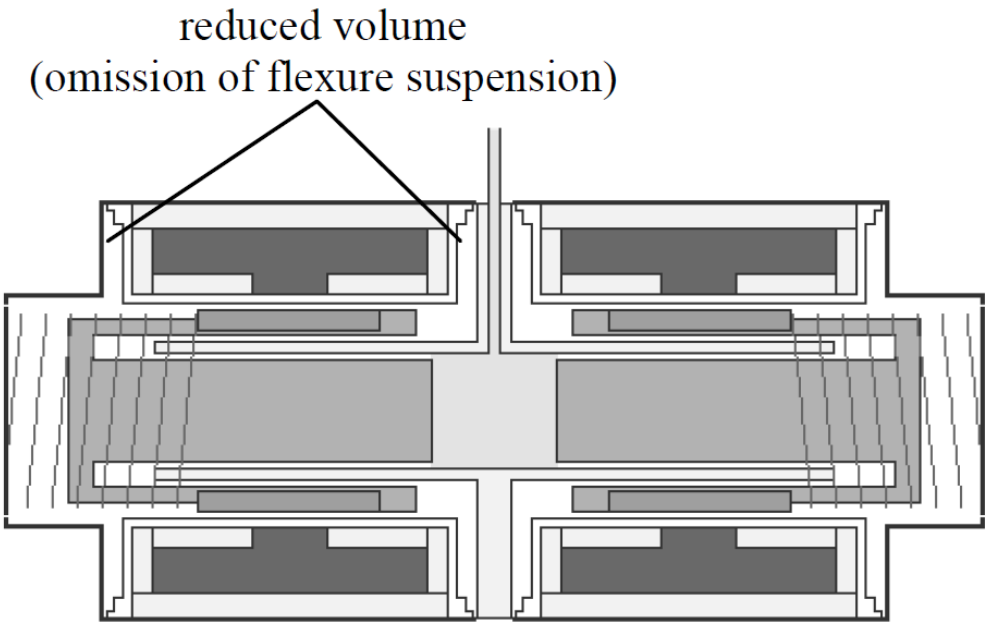

Figure 6: Flipped pistons for increased compactness [17]

To summarize, pulse tube cryocoolers have different design metrics than those for the human-scale mobile hydraulics applications studied in this thesis. This makes direct comparisons difficult. However, they offer creative methods of generating flow in a very compact package, as evidenced by the variations on linear motor-driven piston pumps found in the literature. Such techniques include aluminum flexure bearings to precisely locate the piston shaft in the center of the linear motor and to provide an axial restoring force. Alternative designs have shown increased compactness by using springs to supply the restoring force and relying on the piston clearance seal as the linear bearing.

1.1.4 Off-the-shelf Linear Pumps

This literature review would be incomplete without mention of various linear pumps already available on the market. Linear diaphragm pumps use a moving magnet-type linear motor to actuate a diaphragm and drive flow through passive check valves, as seen in Figure 7. As the coil is energized, the piston retracts to the left, pulling back the diaphragm and drawing fluid into the chamber. As the coil is energized with the opposite polarity, the diaphragm moves to the right, discharging the flow out the delivery check

valve. One such design is manufactured by Gast [19]. Their highest power model, the DBMX200, can deliver up to 190 W of compressed air with a pressure differential of 0.20 bar. This low pressure is impractical for human-scale applications requiring greater amounts of force.

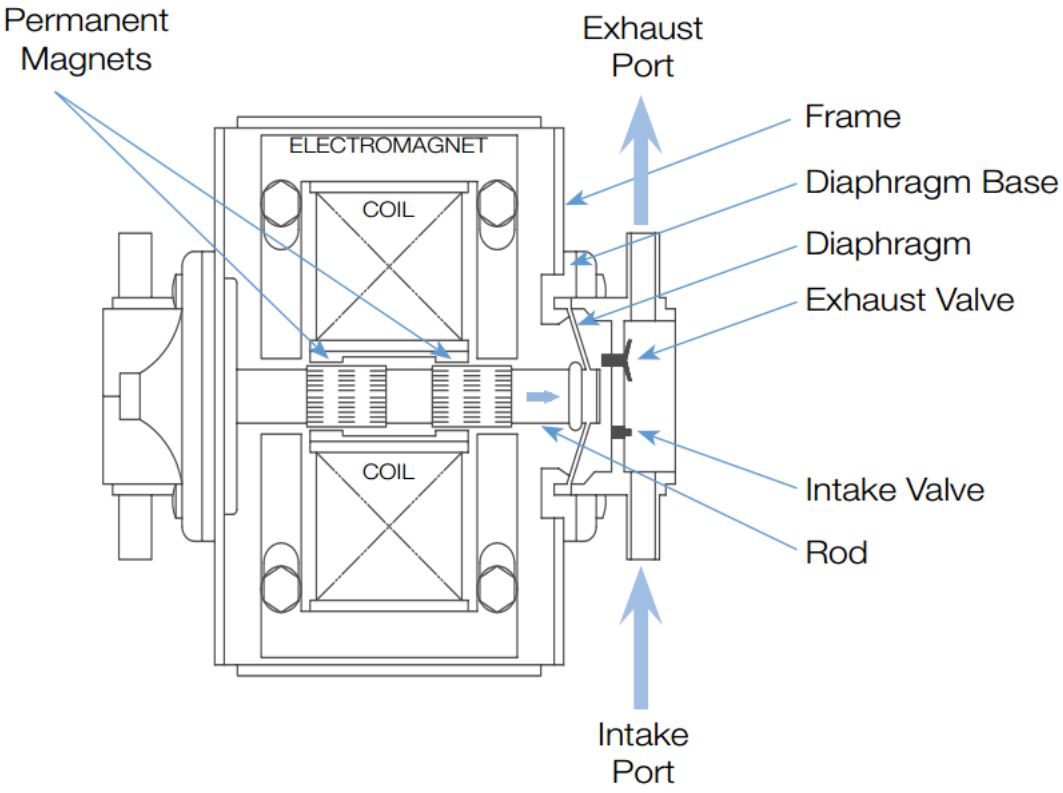

Figure 7: Linear diaphragm pump schematic from Gast [19]

Thomas also sells a linear diaphragm and vibrating armature pump [20]. The moving element floats between restoring springs, operating at a resonance. It displaces a flexible diaphragm as it oscillates, passing up to 625 lpm of peak free flow through passive check valves. Like the Gast model, it also has a low pressure difference of just 0.7 bar.

Finally, Nitto-Kohki has a line of air compressors that are capable of higher pressures that use a linear free piston design [21]. Their rated flowrate is 8 lpm at 2.0 bar,

which results in 27 W of power delivery. Again, this is not a particularly high power output. Like the hydraulic Thomas and Gast devices, the pneumatic Medo device claims very high reliability and efficiency with only a single moving part. In addition, it passes the fluid intake over the electromagnetic coils, resulting in some cooling that permits higher electric current, and therefore higher force and pressure. Nitto-Kohki also manufactures an off-the-shelf piezo pump for liquid applications, but its scale is too small to be considered here.

Advantages of off-the-shelf linear diaphragm and free piston pumps are their high efficiency, low noise, very low maintenance and high reliability due to very few wearing parts, and low power consumption. The significant disadvantage for human-scale applications is that despite the high flow rate, power output is still relatively low. Thomas claims that the low pressure is limited by the strength of the magnetic force, and this may be the case for the other designs as well.

Beyond these examples of low pressure linear diaphragm compressors and linear free piston air compressors, there is limited availability of off-the-shelf linear piston pumps. The examples found here tend to be very limited in their power output, such that for human-scale applications in mobile hydraulics they would be undersized. However, they have advantages that show promise for further research in linear piston pumps. Specifically, the low number of moving parts is often mentioned. This means increased reliability and efficiency, since there are fewer sources of friction that could lead to energy losses and premature wear. Another advantage of these off-the-shelf pumps is their low noise. Again, this is likely due to the limited number of moving parts and reduced friction.

1.3 Overview

This first chapter introduced the reader to the topic of mobile hydraulics with particular attention to human-scale power applications. Typical methods of electric-to-hydraulic energy conversion were discussed along with their merits and drawbacks. The concept of the linear electromagnetic piston pump for reducing conversion losses and increasing power density was introduced. A literature review visited a wide array of

publications that attempted to address the challenge of generating hydraulic power for mobile hydraulic applications, ranging from more conventional techniques that use rotating electric machinery to novel approaches that take advantage of piezoelectric materials or linear motors.

The second chapter will present a quasi-static electromechanical model for predicting linear motor force and inductance. The linear motor will be introduced along with a variety of techniques available for design. A literature review will focus on the design of linear electric motors and actuators from a general standpoint as well as on axisymmetric tubular moving magnet design analyzed in this thesis. Preliminary finite element analysis will be presented for establishing baseline performance metrics. The magnetic equivalent circuit method of magnetics modeling will be used for computationally efficient approximation of motor performance for a wide variety of designs. An experimental linear motor prototype was constructed to validate FEA and the MEC models. Finally, the chapter will conclude with a discussion of the agreement between finite element analysis, magnetic circuit analysis, and the experimental prototype.

The third chapter will discuss the dynamic pump model and design optimization. The lumped parameter dynamic model that solves the mechanical dynamics of the piston motion and the pressure dynamics of the cylinder and load pressures will be presented. The setup, results, and implications of the multi-objective genetic algorithm will be discussed. Model agreement between the finite element and magnetic circuit solutions for the optimized solutions will be presented.

The fourth chapter will document the experimental testing conducted on a linear pump that consists of a linear servo motor connected to pistons and cylinders. Component selection, pump design, and hydraulic circuit design will be presented. Results of the piston displacement, node pressures, and output power will be presented for varied loading and control conditions. The results and their implications for future work on the linear electromagnetic piston pump concept and model will be discussed.

The fifth and final chapter will conclude with the important takeaways from the model performance and results. These takeaways will be tied together with the experimental results to draw conclusions about the linear electromagnetic piston pump. Recommendations for future work will be presented.

2 Quasi-Static Electromechanical Model

2.1 Introduction

2.1.1 Linear Motors

With improvements in magnetic materials and power electronic controls, linear electric motors are seeing increased use in applications historically reserved for pneumatic or hydraulic actuators. Linear electric machinery can use designs that are analogous to many rotating electric machinery concepts. Likewise, the designs are suited to a wide variety of different tasks.

Linear motors are essentially an unrolled rotating motor. They can be rectangular or axisymmetric, with the stator on the inside or the outside. The stator consists of a number of poles that interact electromagnetically with the poles on the shaft to generate a force. The stator or shaft electromagnetic poles sometimes include permanent magnets to set up the flux field that produces force. For many designs, the electric current sent to the stator and/or shaft windings must be commutated. Commutation is when the current polarity is adjusted based on the position of the shaft, or more specifically, the position of the shaft poles relative to the stator poles. This allows greater travel from the motor.

By applying spring return forces to the shaft, linear motors can be configured as an oscillator to operate at a resonant frequency. With a low drag linear bearing, this allows kinetic energy recovery from the piston. The linear electric oscillators found in the literature are typically non-commutated DC, meaning that they take a simple DC input and have limited travel.

In this thesis, a linear motor is designed to use a piston as the moving element. Operation at a mechanical resonant condition permits higher piston stroke than quasi-static operation. To understand the operation of a linear motor in this arrangement, it is important to fully explore the design space to determine the impact of different parameters and evaluate performance. This requires a numerical model that is capable of

reasonable accuracy but fast computation time, coupled to a pump model for use in a system design optimization.

2.1.2 Literature Review

2.1.2.1 Existing linear motor technology

Boldea and Nasar provide an overview of the wide variety of existing linear motor architectures and a foundation to various design techniques [22]. Simple devices to generate a linear force include field alignment devices, such as an iron core near an electric coil. When the coil is energized, the iron will slide such that the magnetic field aligns to the position of lowest potential energy. This concept, applied to a number of adjacent stationary windings and a series of iron teeth, becomes a simple linear motor. Switching the polarity of the current supplied to the windings as the shaft passes positions of zero potential will allow greater travel; this commutation can be achieved with brushes or an electric drive. Other linear motors use multiple coil phases to achieve extended travel, such as the AC linear induction motor modeled in [23]. Permanent magnets can also be used in three-phase linear machines, like their rotating counterparts, as in [24].

Alternative linear motor designs for very short travel can use a non-commutated, brushless DC input. Solenoids and voice coils are two examples of this type of design. They are suitable for short travel, high force density applications. By using return springs, they can be readily converted into linear oscillators. Voice coils in particular have low inductance and therefore have a very fast electrical response. This is desirable for use in an oscillating piston. Axisymmetric motors are able to make better use of a package volume as opposed to a rectangular geometry. Moving magnets, as opposed to coils, make for a more reliable mechanical design. For these reasons, an axisymmetric tubular moving magnet linear motor, such as that presented in [25], was selected.

2.1.2.2 Axisymmetric tubular moving magnet linear motors

Axisymmetric tubular moving magnet linear motors are capable of high force density, fast electrical response, and simple power electronic requirements. The many

variations on such a design are detailed by Wang et al. [26]. Tubular linear motors take a rotating motor, unroll it, and re-roll it along the perpendicular axis. The coils wrap concentrically around a shaft in opposite directions. Radial magnets on the shaft alternate between outward and inward orientations.

A variety of techniques exist for predicting the performance of linear motors, ranging from analytical techniques to finite-element analysis. The objectives of this model are an acceptable level of accuracy across a wide range of geometry and fast computation times for use in design optimization. Analytical techniques are presented for this electric motor architecture in Chen et al. [25] Their analytical model was derived under the assumption of an infinitely long motor, which neglects effects of flux leakage out the ends of the motor. Many other geometrical considerations were neglected. To account for magnetic saturation, they used a correction factor based on the performance of a static magnetic circuit. The model was reasonably accurate when compared to a test case in FEA and experiments, but does not account for cogging effects. Other analytical methods are presented in Zhu et al. [27] and Jang et al. [28] These techniques likewise allowed fast and accurate calculations of the motor force, but they did not allow for a wide range of motor geometries or take account of nonlinear magnetic saturation.

2.1.2.3 Finite element analysis

Finite element analysis (FEA) provides a very good understanding of the performance of a linear motor. It can be very accurate, but at an expense of an order of magnitude higher computational cost. As discussed later, FEA techniques in this thesis required nearly a minute per individual solution of a simple 2D axisymmetric solution. When expanded to a large-scale study, such as that in Tariq et al. to map motor efficiencies, the solution can take hours [29]. Chen et al. used FEA to validate their analytical models and compare with experiments [25], and Hsieh and Hsu used it for magnetic circuit validation [30]. Each paper acknowledged that FEA was too computationally expensive for extensive design work, which was their motivation for pursuing alternate models.

2.1.3 Overview of Motor Design

An axisymmetric view of the motor architecture may be found in Figure 8. Radial permanent magnets set up a magnetic flux path through the stator teeth, and energization of the axisymmetric coils results in a net linear force acting on the piston. The chosen design utilizes a quasi-Halbach array of permanent magnets on the piston to minimize magnetic saturation and allow use of a hollow shaft to reduce moving mass [26]. The number of stator coil windings may be any even number.

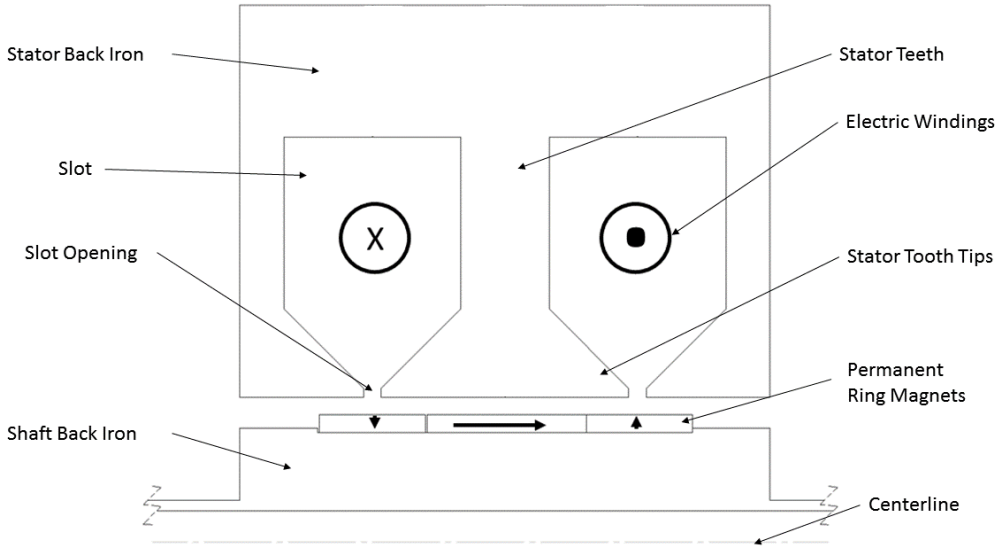

Figure 8: Axisymmetric view of 2-pole linear motor as modeled

As mentioned previously, the advantages of this design are high force density, relatively low inductance and hence fast electrical response, easy and reliable construction as compared with a moving coil design, and a simple DC electric input. The disadvantages of this design are its higher moving mass due to the magnets on the shaft and limited travel as compared to the commutated design.

One expected tradeoff in the design of this device is the wire diameter. Larger wire diameter reduces the number of turns and therefore inductance, while smaller diameter wire is easier to work with in practice and allows for a larger packing factor, the fraction of slot area occupied by coil. Another tradeoff is in stator tooth tip dimensions.

Fatter tooth tips results in a flatter force-vs-displacement profile at the cost of increased inductance.

2.1.4 Chapter Overview

In this chapter, the rationale for the selection of the axisymmetric tubular moving magnet motor design is discussed. Finite element analysis was conducted to establish performance baselines. The magnetic equivalent circuit method for modeling power magnetic systems is presented in the context of this linear motor problem. The performance of the FEA and MEC models is compared using flux density, force, and inductance metrics. Finally, an experimental prototype of the linear motor is built and its excitation force measured for comparison with the FEA and MEC calculations.

2.2 Finite Element Analysis

An initial study of the linear motor was conducted using FEA to establish baselines for expected performance and to explore the influence of different design parameters.

2.2.1 Model Definition

A dimensioned drawing of the linear motor is presented in Figure 9. The linear motor geometry is specified in terms of ratios of these values with respect to the outer radius, R_o, as presented in Table 1. The rationale for this is explained more fully in Chapter 3, but it allows design variables to have natural limits. For instance, the ratio α_{pm} must be between 0 and 1 because it does not makes physical sense for the magnet thickness to be less than 0 or greater than R_m.

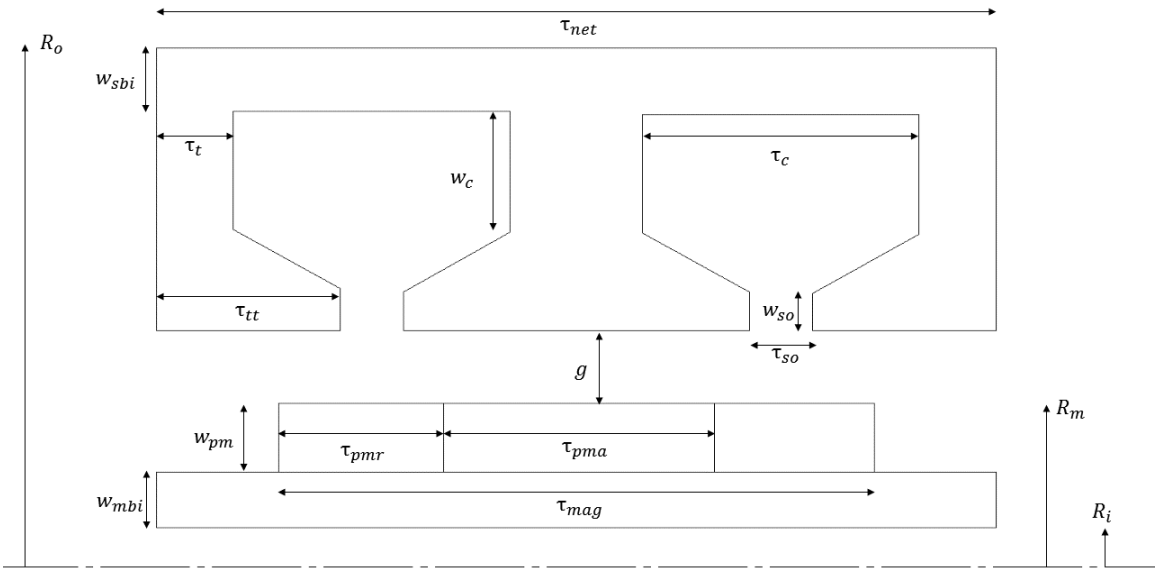

Figure 9: Dimensioned drawing of linear motor

The specifications for a modeled tubular linear motor are presented in Figure 8. The air gap was set to 1 mm, and the slot between the stator tooth tips was set to 2 mm. The stator back iron, or thickness of the stator outside the coils, was set to 4 mm.

Table 1: Design parameters for baseline FEA study

Variable	Value	Description
D	6.00 mm	piston diameter
f	45 Hz	driving frequency
k	20 kN/m	spring constant
n_{pole}	4	number of stator poles
R_o	50 mm	stator outer radius
α_{net}	1.50	τ_{net}/R_o
α_{mag}	0.63	τ_{mag}/τ_{net}
α_{pmr}	0.33	τ_{pmr}/τ_{mag}
α_m	0.35	R_m/R_o

α_{pm}	0.13	w_{pm}/R_m
α_i	0.30	R_i/R_o
α_t	0.50	τ_t/τ_{tt}
d_{wire}	1.35 mm	wire diameter

The motor was modeled using the Ansys Maxwell electromagnetics package, with a 2D axisymmetric magnetostatic solver. The solution uses an adaptive technique to refine the mesh in regions of high gradients down to 0.1% error, and the nonlinear magnetic solution is solved to a residual of 10^{-4}. The boundary region was 400% of the motor size and was set to a zero vector potential boundary condition. The magnets are NdFe35, and the magnetic steel is Hiperco50. The solution swept a design space of quasi-static piston displacements at 1 mm increments from -10 mm to 10 mm to generate the force-vs-displacement profile for the motor geometry.

2.2.2 Results

The computation time for the FEA was 22 minutes for 21 different piston displacements using a virtual Windows machine through the Minnesota Super Computing Institute (MSI) with an Intel Xeon CPU at 2.70 GHz with 8 processors and 61 GB of RAM. The force-vs-displacement profile is shown in Figure 10. For this motor geometry, the force is relatively constant near the center of travel before falling off beyond 5 mm. There is another leveling off of the force between +/- 8 mm and 10 mm, but at this displacement the performance is clearly diminished.

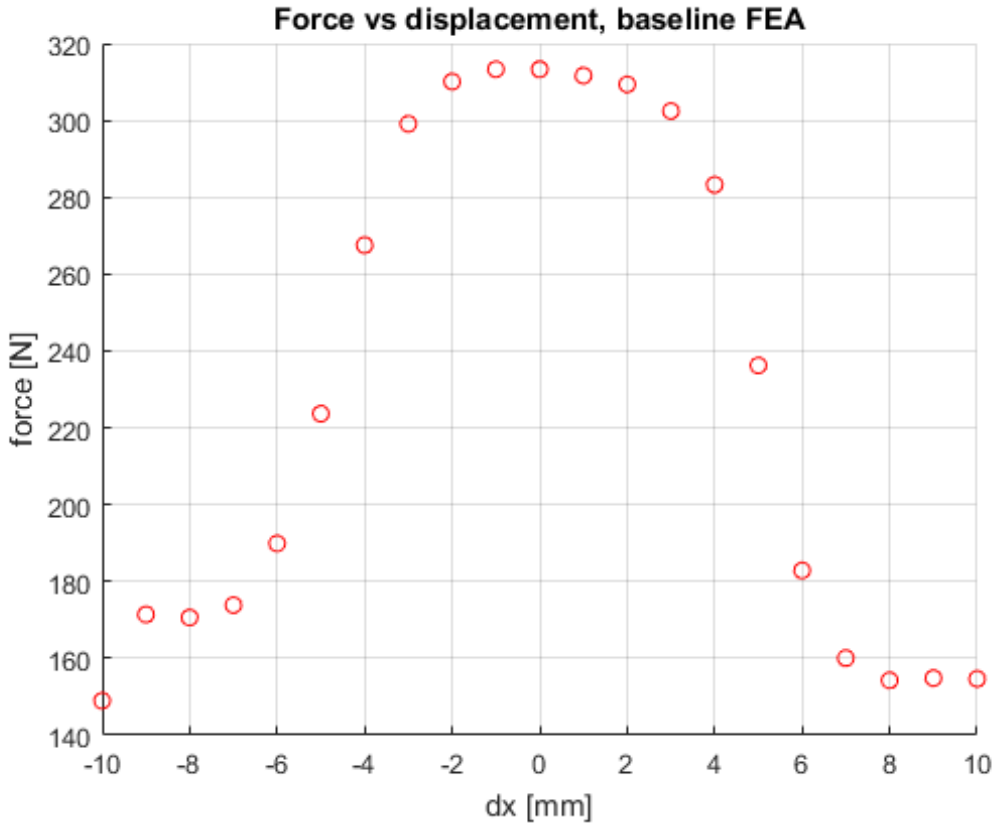

Figure 10: Force vs displacement for FEA solution

The motor has an inductance of 82 mH at zero displacement, with very minimal change as the piston is displaced, as seen in Figure 11. The inductance is slightly asymmetrical with position, with a slightly higher value at -10 mm than at 10 mm shaft displacement.

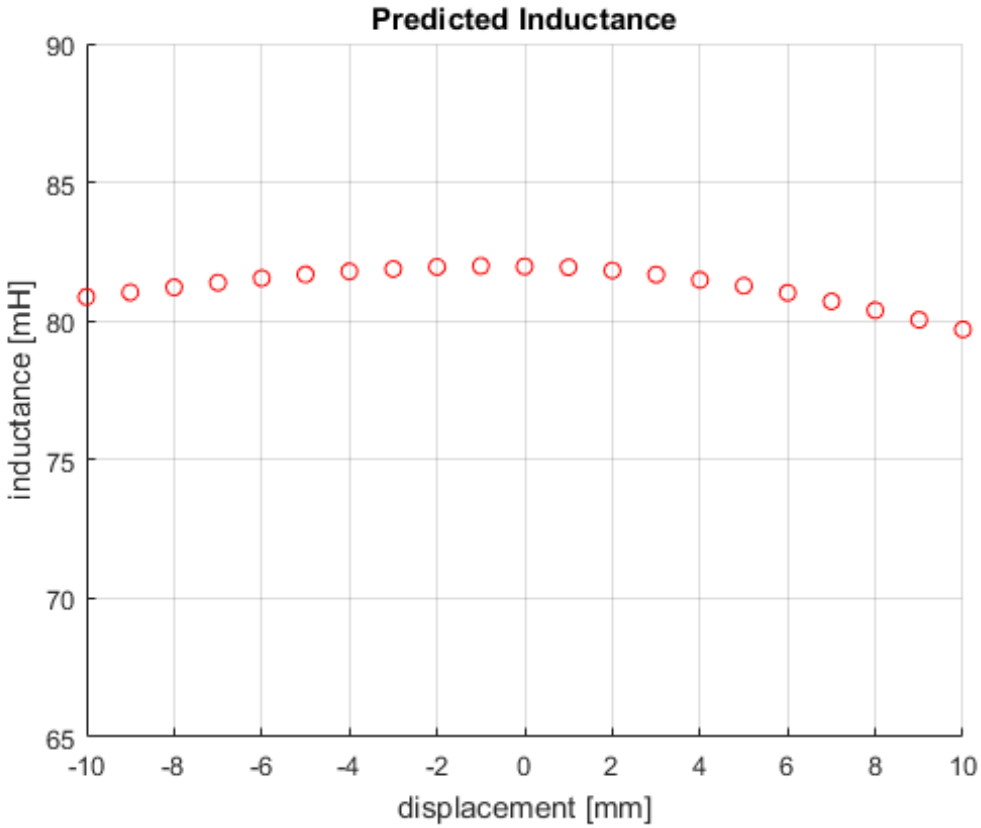

Figure 11: FEA solution for inductance-vs-displacement

The FEA solution for magnetic flux density is shown in Figure 12 and the flux lines in Figure 13. The magnetic flux is analogous to electric current and represents the flow of magnetic energy in a device. Flux is the output of the MEC reluctance network

solution and is the basis for all force and inductance calculations using the MEC.

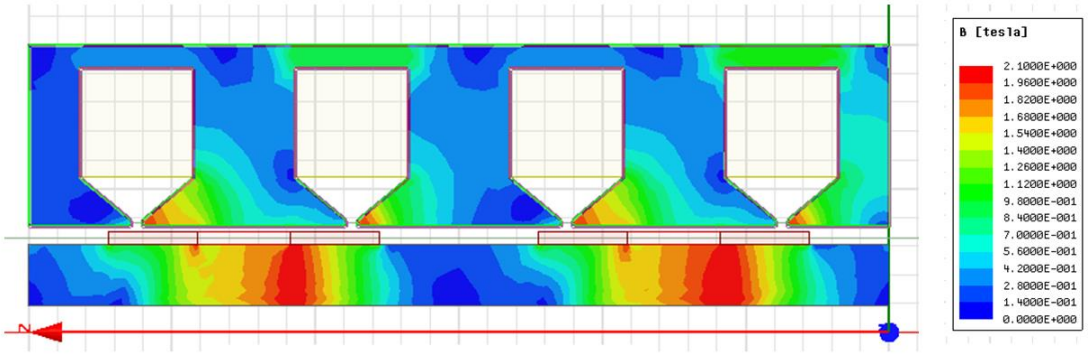

Figure 12: FEA solution for flux density

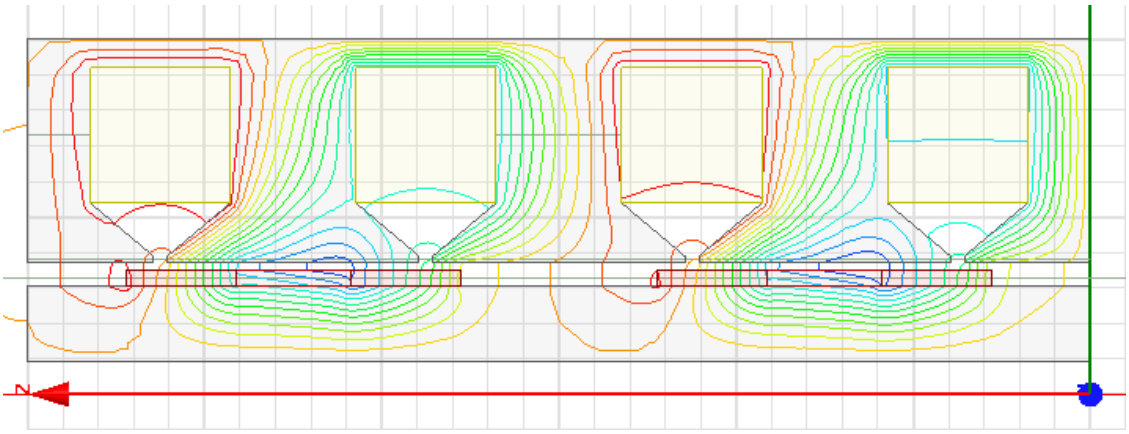

Figure 13: FEA solution for flux lines

Saturation for Hiperco50 occurs at approximately 2.1 T, so there are regions of the shaft for this design that have saturated. Magnetic saturation means that increasing magnetic field intensity results in a limited increase in magnetic flux density and is a limit to a material's performance. Increasing the cross-sectional area or reducing the field intensity are two methods of reducing saturation in a design. The flux in this linear motor design generally circulates around the slots, which contain the electric windings. Some leakage occurs across the slots and around the magnets, but due to the low saturation in the stator this leakage is kept to a minimum.

2.3 Magnetic Equivalent Circuit

Despite the advantages of FEA, it is too computationally intensive for use in parameter space exploration or design optimization. A balance between analytical and FEA modeling techniques is a magnetic equivalent circuit (MEC), as described by Ostovic [31]. An MEC can better capture the effects of different geometrical parameters and saturation than analytical techniques, while solving in at least an order of magnitude less time than FEA. This makes it ideally suited for use in a design optimization involving electromagnetic components.

An MEC uses a network of reluctances and magnetomotive forces (mmf) to model the flow of magnetic flux in a magnetic circuit, much like a resistor and emf network is used for electric circuits. The reluctances are known as branches, and they are connected to nodes. The solution of the MEC uses the same techniques as used to solve non-linear electric circuits. The MEC toolbox 3.2 for MATLAB, developed by Scott Sudhoff, was extremely useful for solving the magnetic circuit developed in this thesis [32].

2.3.1 MEC Literature Review

Many examples of electromagnetics and, more specifically, MEC modeling exist in the literature. Hanselman provides a good introductory reference to the design of rotating electric machinery [33]. His introductory chapter offers a qualitative foundation to the design of rotating electric machinery, establishing a basis for the mechanisms behind torque production and the need for commutation or three-phase designs for continued motion. His second and third chapters discuss fundamentals of electromagnetic modeling and electromechanical relationships, with a light magnetic circuit discussion. His explanation of magnetic materials is helpful as well. The later chapters focus on the analysis and design of different specific types of rotating machinery. Overall, Hanselman's book provides a good conceptual foundation for fundamentals, but is lacking somewhat in detailed MEC concepts and methods for modeling linear machinery.

For a more detailed discussion of MEC modeling, Sudhoff's book on power magnetic machinery is a very good reference [34]. He provides very detailed explanations of magnetic circuit construction, including derivations for different flux leakage terms in Cartesian coordinate systems, straightforward methods of force and inductance calculation, and a few different methods for estimating core loss in magnetic steel. His introductory chapter also provides very useful information about optimization algorithms, which is helpful for establishing a conceptual basis for the NSGA-II genetic algorithm discussed in Chapter 3 of this thesis. As in Hanselman, later chapters in Sudhoff focus on modeling rotating machinery. For a reader already familiar with electromagnetic concepts, this is an excellent resource. It is perhaps too detailed for a first read, however.

Certain challenging aspects of MEC construction for a linear motor are documented in the literature, albeit often for rotating machinery. One subject that has seen a number of publications is that of dealing with relative motion within the model. This is challenging for two reasons. First, reluctances cannot go to infinity, or the MEC solution fails. Second, the number of branches may change depending on where the rotor and stator are. Bash et al. present detailed techniques for rebuilding the MEC network in the presence of motion [35]. Their method, for a synchronous machine, pre-defines a series of nodes on the stator and rotor tooth tips. Based on the position of the rotor with respect to the stator, the shape of the air gap branches can be determined. The number of possible shapes is limited, so the modeler can pre-define all the possible mesh branch shapes and use the algorithm to select the proper definitions. They do not provide any comparison with FEA, although similar mesh based techniques perform well in quasi-static analysis. The significant downside to modeling the reluctances in this manner is that fringing flux off the stator and rotor teeth must be captured in the same expression. The derivation for such an expression is infeasible for the axisymmetric linear motor modeled in this thesis modeled in cylindrical coordinates.

Severson et al. offer a similar approach for dealing with air gap branches that accounts for the fringe flux [36]. Instead of using a single branch spanning the entire air

gap, they split the air gap in two such that the stator side fringe flux terms are constant when the rotor is moving. The mesh branches in the moving air gap are calculated based on the overlap of different stator and rotor nodes. Their results agree quite well with FEA solutions and experimental results for a number of measurements, including flux density in the stator teeth and torque. This technique of modeling the air gap was modified for use in the linear motor presented in this chapter.

Limited literature exists on the use of MEC modeling for the axisymmetric linear moving magnet tubular design presented in this thesis, although Chillet et al. [37] and Batdorff et al. [38] present detailed derivations of magnetic flux leakage and fringing permeances in cylindrical coordinates that were helpful.

2.3.2 MEC construction

The MEC used in this model is shown in Figure 14 for two poles. The pattern can be replicated out to an arbitrary even number of poles. In constructing the MEC, lists of mesh branches and mesh fluxes are identified. Each branch has a material, a cross sectional area, and a length associated with it. They may also have a magnetomotive force, or mmf, which is a result of electric windings or permanent magnets. The MEC toolbox for MATLAB, coordinated by Sudhoff, uses this information to calculate the reluctance for each branch and iteratively solves the nonlinear matrix equation for the mesh fluxes

$$\Im = \Phi\mathcal{R}(\Phi) \tag{1}$$

where $\Im$ is an mmf, Φ is the flux, and $\mathscr{R}(\Phi)$ is the nonlinear reluctance [32]. Note that this expression is analogous to Ohm's law for electrical circuits.

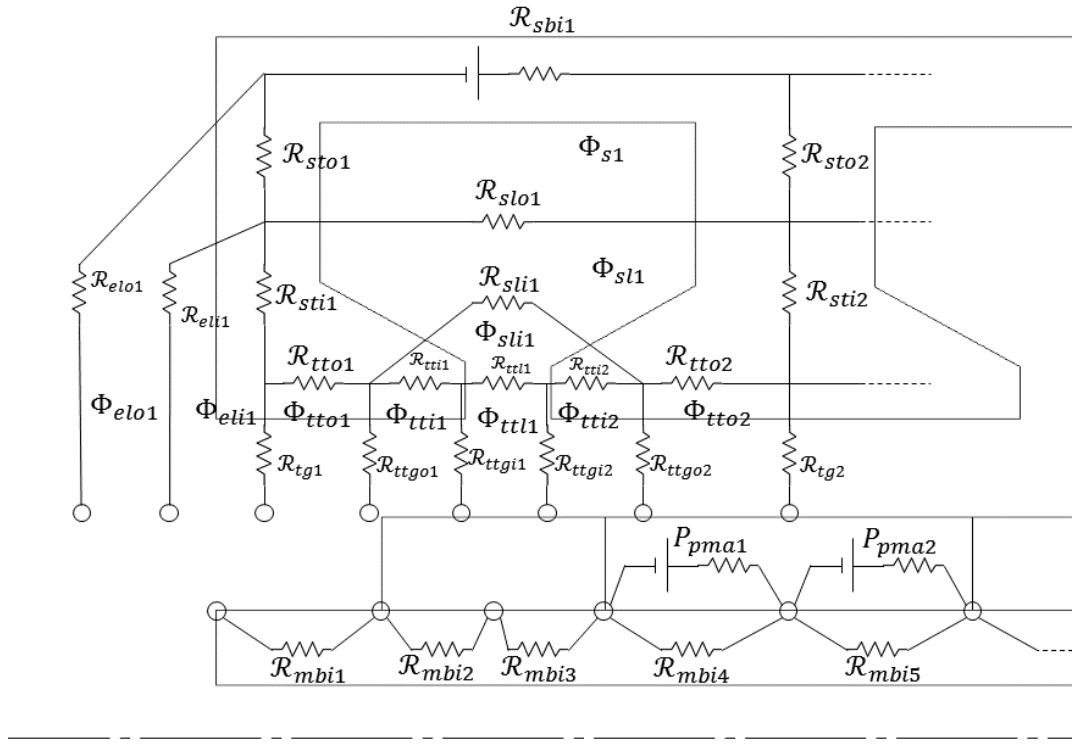

Figure 14: Portion of the magnetic equivalent circuit model

When expressing the different reluctances in an MEC, the key assumption is that all the magnetic flux through a branch enters at one end and exits at another, passing through what is known as a flux tube. For the reluctance to be valid, the flux cannot cross the outer boundary of the flux tube. The dimensions of this flux tube are what enter into the reluctance equation.

2.3.3 Reluctance Definitions

The magnetic flux is related to the mmf drop by a reluctance, analogous to an electrical resistance. In a general case, the reluctance is defined as

$$\mathcal{R} = \int \frac{dx}{\mu_p(B)A} \tag{2}$$

where $\mu_p(B)$ is the nonlinear permeability of the material and is a function of the flux density B, which is the magnetic flux per unit area. A is the cross-sectional area. Using the above equation, reluctances were defined for each branch of the magnetic circuit to discretize the geometry into the reluctance network.

For the most part, the effective cross sectional area and length were derived independently for each branch because the branches took on a number of different profiles. Many of the branch reluctances are derived in the literature for axisymmetric linear actuators, such as Chillet et al. [37] and Batdorff et al. [38] As a case study, the derivation for the effective area of $\mathscr{R}_{\text{sto}}$ will be presented below, starting with Equation 2. The remaining steel flux tubes are defined in Figure 16.

2.3.3.1 *Derivation of $\mathscr{R}_{sto}$*

The flux tube for the outer stator tooth mesh branches is shown in Figure 15. The flux tube is oriented in the radial direction, and starts midway through the slot opening and terminates midway through the stator back iron. These radii are denoted R_{in} and R_{out}, respectively. The axial width is constant and is equal to the tooth thickness, τ_t.

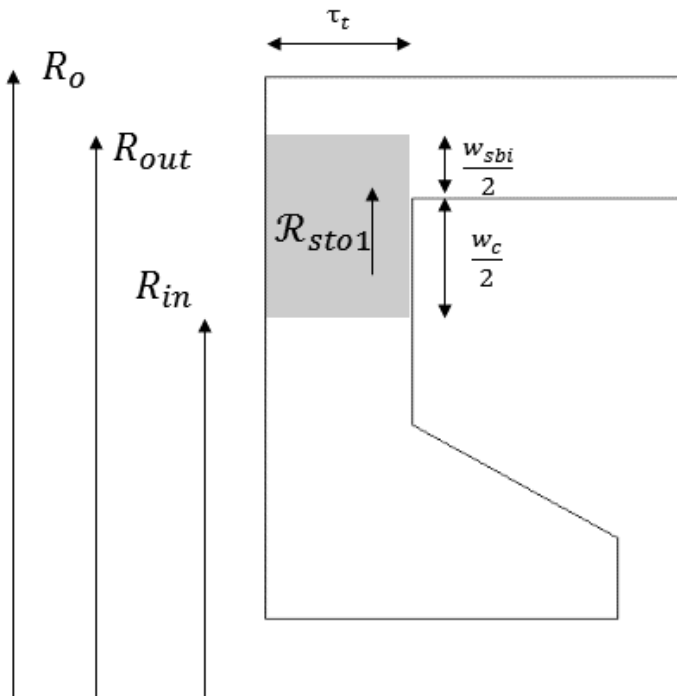

Figure 15: Dimensions of Rsto flux tube.

Starting with Equation 2, we integrate from R_{in} to R_{out} with $A(x) = \tau_t 2\pi x$. The result gives

$$\mathcal{R}_{sto} = \frac{\ln\left(\frac{R_{out}}{R_{in}}\right)}{\mu(B)2\pi\tau_t} \tag{3}$$

Since an effective area and length are required to build the mesh branch, and since an effective area is also needed to estimate the flux density *B*, this equation must be re-written in terms of an effective area and length. These can be written as follows:

$$l_{eff} = R_{out} - R_{in} \tag{4}$$

$$A_{eff} = \frac{2\pi\tau_t l_{eff}}{\ln(\frac{R_{out}}{R_{in}})} \tag{5}$$

2.3.3.2 *Flux tube definitions*

Figure 16 gives the positioning and dimensions of the stator-side flux tubes. The effective areas and lengths for each flux tube are derived in a similar manner to $\mathcal{R}_{sto}$.

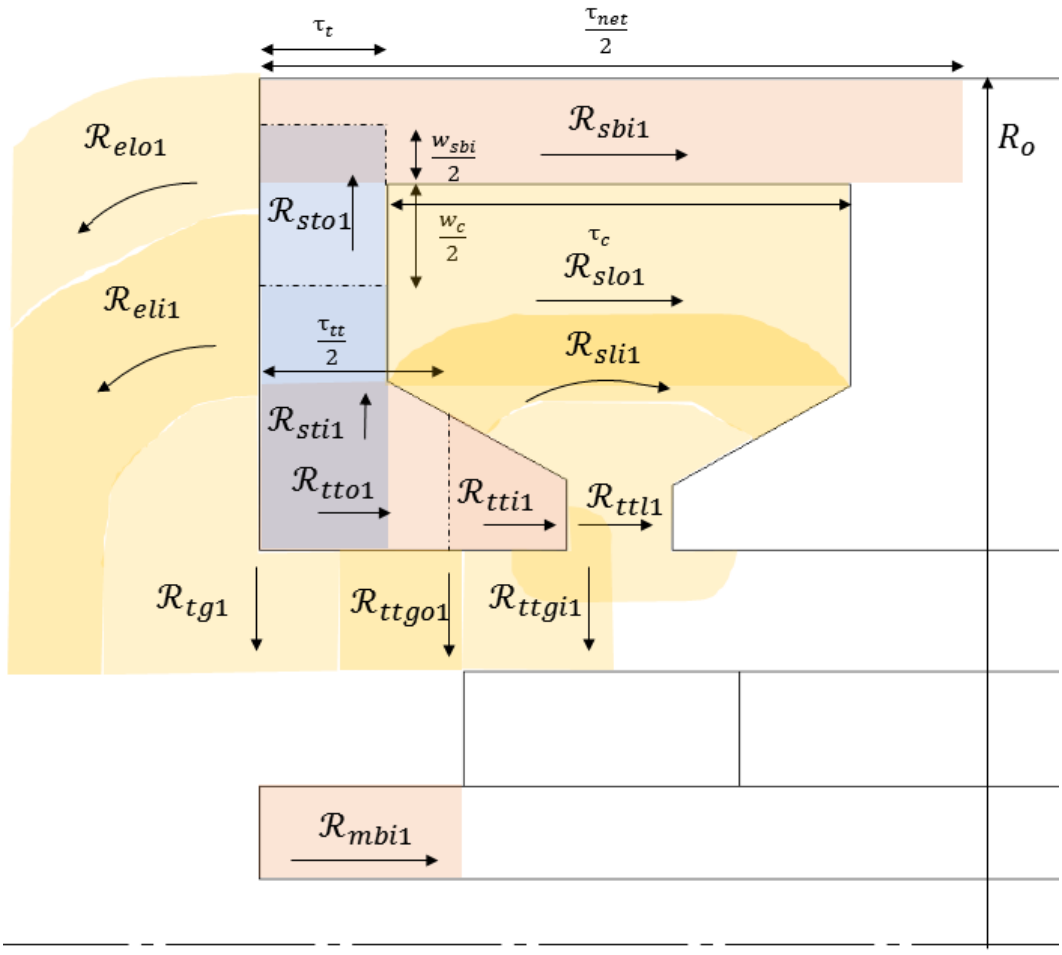

Figure 16: Flux tube definitions

2.3.4 Evaluation of Air Gap with Motion

The 3.2 version of the MEC toolbox allows for a mixed mesh- and nodal-based solution. To this point, a mesh-based solution technique has been discussed. Nodal based solutions use permeance, the inverse of reluctance, instead to solve Ohm's law for magnetics. The difference between the two techniques is analogous to the difference

between Kirchoff's voltage and current laws: mesh techniques require the sum of the mmf drops around a closed loop to be zero, while nodal techniques require the net flow of flux into each node to be zero. In a purely mesh-based solution, the reluctance cannot be set to infinity to "turn off" a particular branch. On the other hand, in a nodal-based solution, the permeance can be set to zero to block off branch of the MEC.

This is useful for evaluating the permeance of the air gap between the shaft and the stator. When the shaft moves relative to the stator and branches are getting connected or disconnected, the nodal-based solution allows unused permeances to be set to zero, blocking off a branch of the MEC. This allows every possible combination of air gap permeances to be defined, but by default set to zero unless there is an overlap.

The approach used by Severson et al. to account for motion was adapted to a linear design using this mixed nodal- and mesh-based solution [36]. The stator side of the air gap is constant, so fringing flux can be accounted for independently of the shaft motion. Different branches of the MEC within the permanent magnets were connected and disconnected based on the overlap of nodes on the stator and shaft sides. Each node on the stator and shaft has a position and range of influence associated it. The shaft node positions depend on the displacement of the shaft.

In the MEC solution at each displacement, a loop runs through each possible combination of stator and shaft nodes. If there is an overlap between a pair of stator and shaft nodes, the permeance for that branch is evaluated, as is the case between x_{s-1} and x_m in Figure 17. The permeance $\wp_{s-1,m}$ is evaluated based on the amount of overlap. If the overlap also includes a radial permanent magnet as is the case between x_s and x_m, then a flux source will also be applied to the branch in parallel with a permeance. The magnitude of the flux source is equal to the product of the magnet remanence, B_r, and the effective cross-sectional area of the overlap.

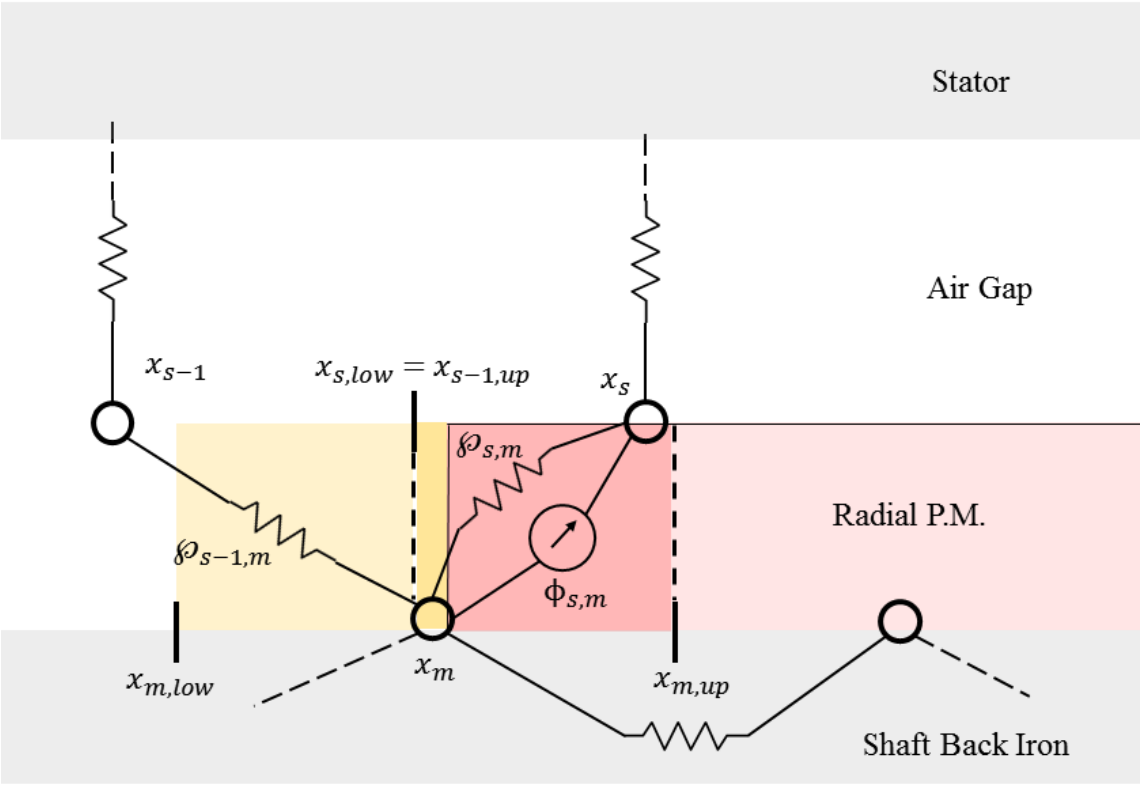

Figure 17: Evaluation of air gap permeance with shaft motion

2.3.5 B-H Curve: Material Definition

Essential to the material definition for MEC and FEA solution is the B-H curve. This highly nonlinear curve gives the flux density *B* as a function of field intensity *H*. In other words, it provides the permeance μ of a material as a function of the strength of the magnetic field, where $B=\mu H$. It is important that materials not exceed their saturation flux density, at which point the permeability becomes closer to that of a vacuum. Not only is saturation detrimental to performance, it also encourages flux to deviate from its intended path. This increased flux leakage is difficult to model accurately with an MEC.

Using a B-H curve in an MEC requires that the function follow a very precise form, which may be curve-fit as in Shane et al. [39] The B-H curves for the high-performing Hiperco50 from Carpenter Steel, provided in the Appendix of Sudhoff [34], and the low carbon steel used in the prototype, based on values given in Ansys Maxwell,

are given in Figure 18, along with their curve-fits. Note the significantly lower saturation of the low carbon steel.

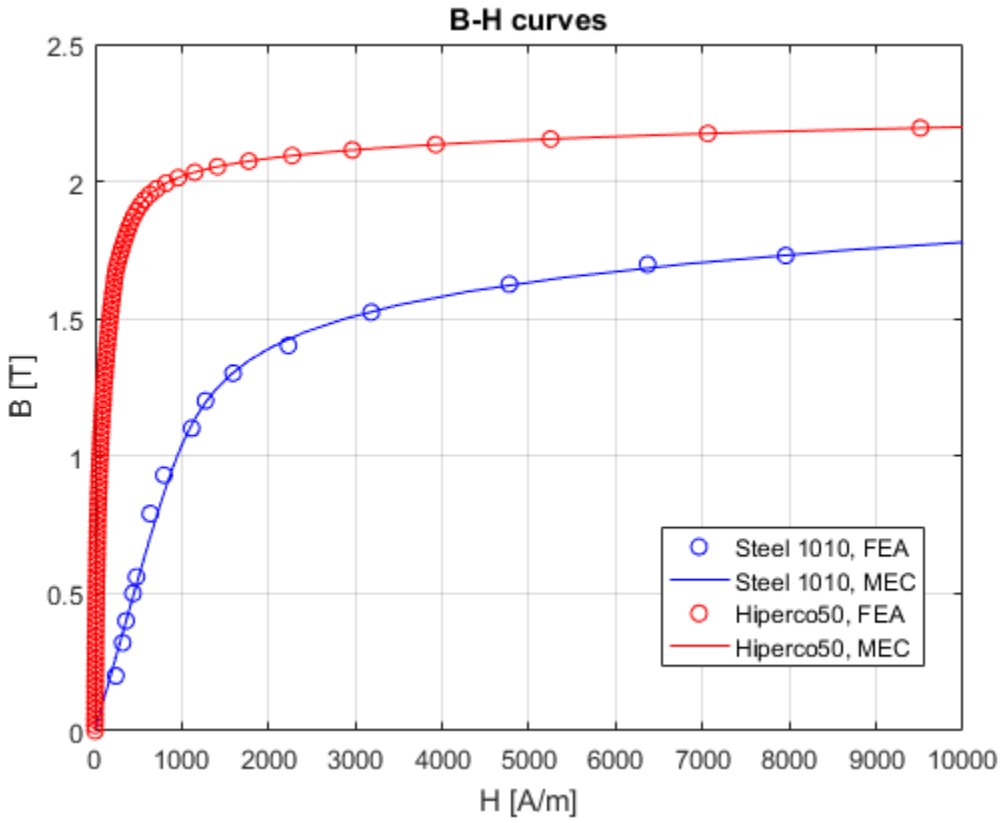

Figure 18: B-H curves used in MEC and FEA

2.3.6 MEC Solution

A solution to the MEC assumes operation at quasi-steady state, with electrical current input. These assumptions are justified by the relatively low inductance, and hence low $L\frac{di}{dt}$ term, which represents the voltage required to charge and discharge the coils. As long as this charging voltage is below a reasonable value, assuming a current input to the linear motor is reasonable as well. The limiting charge voltage is assumed based on maximum capabilities of power supplies.

The MEC is used to evaluate the force-vs-displacement characteristic of the actuator geometry, which is an input to the mechanical dynamics model. It also evaluates

the motor inductance, which validates the quasi-steady state assumption, and the magnetic losses, a consequence of the magnetic hysteresis and induced eddy currents in the magnetic steel.

2.3.6.1 Force evaluation

The total electromagnetic force can be expressed as:

$$F_{act} = \sum_j i_j \frac{d\lambda_j}{dx} - \frac{\partial W_f}{\partial x} \tag{6}$$

where x is the shaft displacement, λ_j is the flux linking the j-th coil, i_j is the current in the j-th coil, and W_f is the total field energy. The flux linkage is the amount of flux passing through a coil, multiplied by its number of turns. It represents the amount of energy stored in the form of inductive energy within the coil. The second term represents the change in energy stored in each branch of the magnetic circuit. It was found that the field energy contribution to force for this type of linear motor is relatively small, within 4% percent error 5 mm displacement if the magnets are not too large, so the total force was assumed to be the change in flux linkage with respect to displacement. As is found in section 2.4, this was a good assumption, as confirmed by FEA. The assumption starts to break down for very thick magnets, which exhibit much larger cogging forces as the field energy attempts to minimize itself at certain positions.

The flux linkage is calculated using

$$\lambda_j = N\Phi_j \tag{7}$$

where the j-th branches correspond to the mesh branches that contain the mmf terms for the coils and Φ_j is the flux, which is a direct output of the MEC solution. The evaluation for λ_j is smoothed using a moving average, since the MEC solution has several discontinuities in its slope due to air gap permeances switching on and off.

The flux linkage is used in Equation 6 with field energy set to zero to find the force. The force is fit to a piecewise Hermite cubic polynomial for faster evaluation than a simple interpolation.

2.3.6.2 Inductance evaluation

The inductance for a multi-winding machine is expressed as a matrix, where the diagonal terms are the self-inductances and the off-diagonal terms are the mutual inductances. For instance, for a two-winding machine the inductance matrix is as follows:

$$L = \begin{bmatrix} L_{11} & L_{12} \\ L_{21} & L_{22} \end{bmatrix} \tag{8}$$

where the total inductance is the sum of all the self- and mutual-inductances [40]. The inductance matrix relates the flux linkage λ and current i:

$$\begin{bmatrix} \lambda_1 \\ \lambda_2 \end{bmatrix} = \begin{bmatrix} L_{11} & L_{12} \\ L_{21} & L_{22} \end{bmatrix} \begin{bmatrix} i_1 \\ i_2 \end{bmatrix} \tag{9}$$

To evaluate each self- and mutual-inductance, the windings are each excited individually by a unit 1 A-turn and the MEC solved with magnets turned off. For instance, current i_1 is set to 1 A-turn and i_2 set to 0 A-turn. Plugging these values into equation 9 gives two equations:

$$\lambda_1 = L_{11} \tag{10}$$

$$\lambda_2 = L_{21} \tag{11}$$

The flux linkage is calculated as discussed in equation 7, section 2.3.6.1, giving the self-inductance L_{11} and the mutual-inductance L_{21}. By exciting each winding in turn, the full inductance matrix can be calculated. These equations and the solution technique can be generalized to any number of windings.

2.4 FEA/MEC Model Agreement

To validate the MEC model, the same design specifications as documented in Table 1 were used to replicate the FEA results. These results were primarily quasi-static analysis to determine the force and inductance as functions of piston displacement, as well as measurements of the magnitude of the flux density in different parts of the motor. A transient analysis was used to estimate losses in the steel and compare with those computed using a quasi-static MEC.

2.4.1 Quasi-static analysis

2.4.1.1 Flux density in stator teeth

Comparisons of the flux density in the motor are important to ensure that the MEC is evaluating the flux within the circuit correctly. The three comparisons listed here use the FEA results in Figure 19 with the lineouts as illustrated. A "lineout" is a slice of sample points through the geometry.

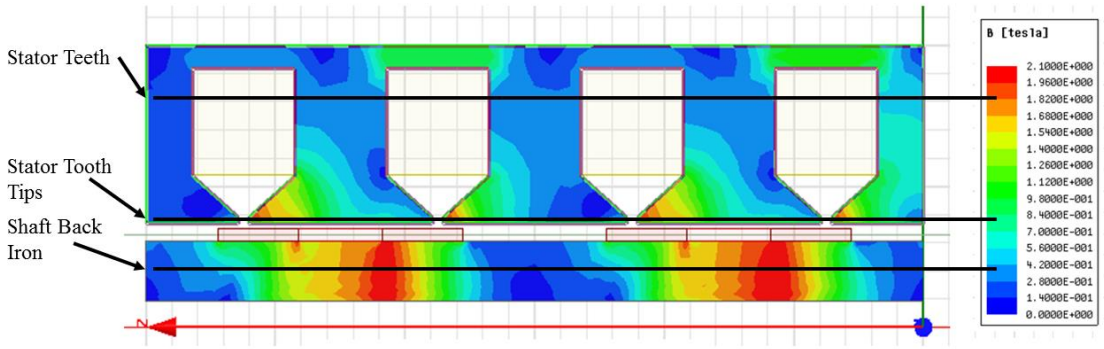

Figure 19: FEA-modeled flux density with lineouts for data sampling labeled

The flux density in the stator teeth has important implications for the performance of the motor, since this is related to the flux linked by the winding and therefore the force produced by the motor. A lineout taken across the stator teeth from left to right sampling the FEA solution for flux density magnitude is compared with the MEC results in Figure 20.

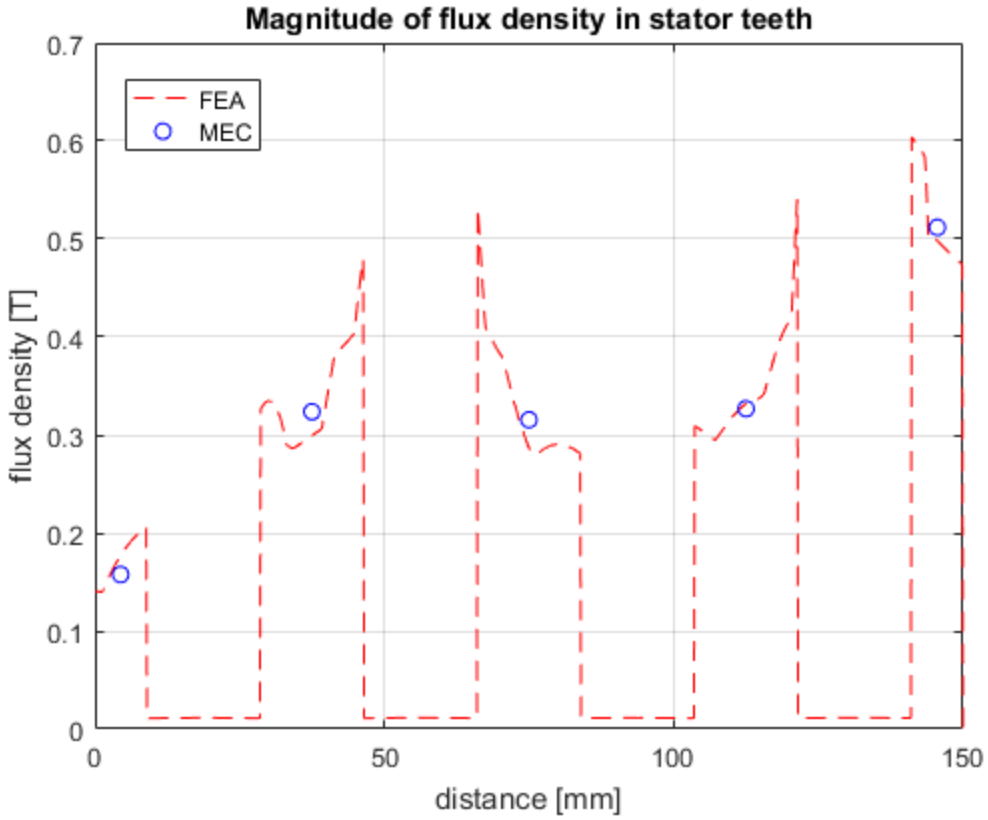

Figure 20: Flux density in stator teeth

The MEC predicts the flux density in the stator teeth very well. Since it does not have the resolution of FEA, it does not pick up the same peaks near the edges of the slot, but these are not important for evaluating the performance of the motor.

2.4.1.2 Flux density in stator tooth tips

The flux density in the stator tooth tips is also important for force calculation, as it's an indicator of the amount of magnetic flux traveling from stator to shaft. The agreement in the tooth tips captures the correct trends, but is too low, as seen in Figure 21.

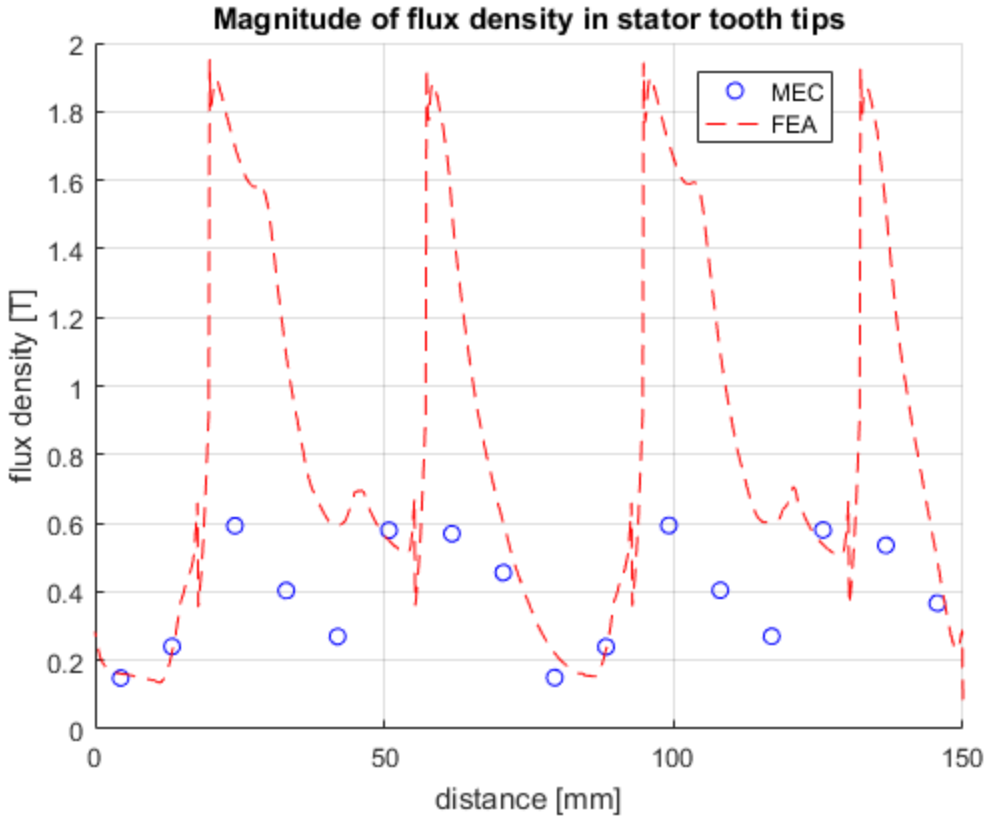

Figure 21: Flux density in stator tooth tips

The flux density is likely too low in the MEC because the area varies significantly through this mesh branch, as shown in Figure 19, so the flux density is highly dependent on where it is calculated. In this case, it is calculated at the midpoint of the branch. Peak flux density occurs at the very tip, as shown by the deeper orange spots in Figure 19. Calculation at a position with a smaller area would significantly increase the flux density. This error could still have an effect on the estimated linear motor performance because saturation in the steel is related to flux density, and the FEA clearly comes much closer to saturation in the tooth tips than the MEC would predict.

2.4.1.3 Flux density in shaft back iron

The flux density in the shaft back iron agrees much better with the FEA solution, as shown in Figure 22.

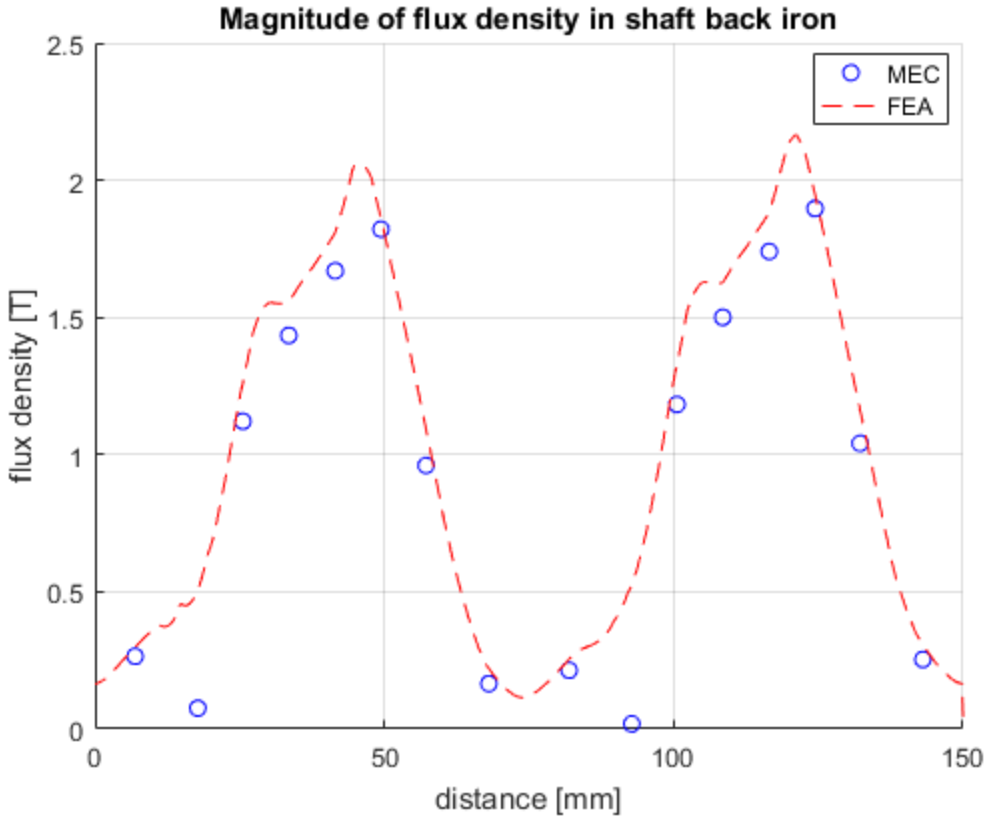

Figure 22: Flux density in shaft back iron

This agreement is important because the shaft back iron is a short circuit connecting the radial magnets together. As a result, a large amount of magnetic flux flows through the shaft back iron. Accurately predicting the flux density in regions of high flux is important, and Figure 22 demonstrates the agreement with FEA.

2.4.1.4 Force-vs-displacement

A comparison of the MEC and FEA calculations of force for this motor geometry are shown in Figure 23. Note that MEC results are now a solid line, since many more MEC data points were collected than FEA solutions.

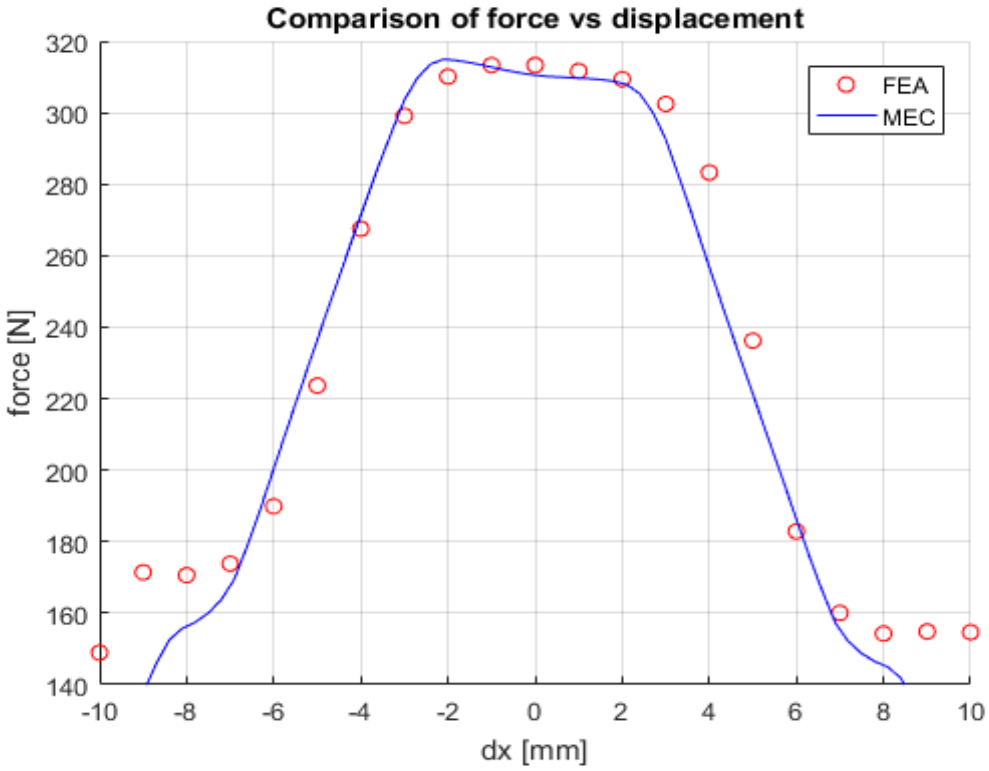

Figure 23: Force vs displacement for FEA and MEC solutions

The force computed by the MEC at zero displacement is within 2% of FEA results. It also correctly predicts that the force will start to fall off around +/- 3 mm. The error starts to increase at larger displacements; the MEC begins to capture the flat force from 8-10 mm, but still has about 12% error. However, this is not critical since it is not expected that the linear motor will need to displace this far. Also, when operated with return springs, the spring forces will begin to dominate in this region.

2.4.1.5 Inductance-vs-displacement

The MEC and FEA evaluation of inductance is relatively constant at about 82-84 mH. Although the magnitude of the MEC inductance calculation is off by about 2.5%, it does a good job of capturing the relative change across the range of travel.

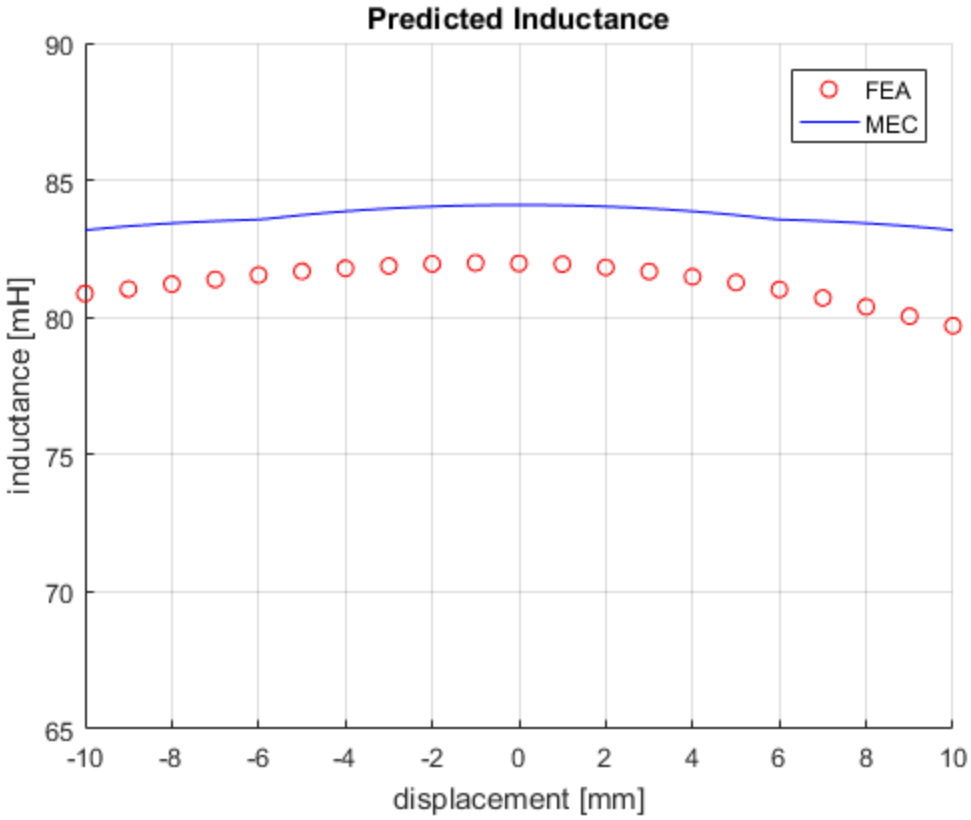

Figure 24: Comparison of inductance vs displacement

The FEA solution for inductance is slightly asymmetrical with displacement, which is not captured by the MEC. This discrepancy is insignificant, considering that the MEC still predicts inductance within about 5% at that displacement. Like FEA results, the MEC still captures a peak at 0 mm and very flat profile with displacement.

A summary of the key comparisons between the FEA and MEC solutions is presented in Table 2.

Table 2: Summarized comparison of FEA and MEC solutions

Parameter	FEA	MEC	Error
Force @ dx = 0 mm	313 N	311 N	-0.6%
Force @ dx = 5 mm	236 N	220 N	-6.8%
Inductance @ dx = 0 mm	82 mH	84 mH	2.4%

E.M. solution time	20 min	1.5 sec	

Overall, in this baseline case the MEC does a very good job capturing force and inductance characteristics observed in FEA. As a final point, the solution time for FEA was 20 minutes for 21 data points, or about 57 seconds per solution. The MEC required 1.5 seconds for 101 data points, or just 15 ms per solution. Taken together with the accuracy of the solution, MEC modeling is an excellent substitute for FEA in design optimization.

2.4.2 Transient Analysis

The objective of transient analysis of the linear motor was to estimate the magnitude of losses within the stator. As the flux density within a magnetic steel varies, it undergoes different power losses. The first is hysteresis loss, which is due to the hysteresis in material B-H curves. As the flux density changes, the material traverses the B-H curve in different directions. The gap between the two curves manifests itself as a power loss. The second core loss is due to eddy currents, which form in reaction to a changing magnetic field. Eddy currents are real flows of electrical current in the magnetic steel, and come with an associated ohmic loss.

The FEA transient analysis was conducted with a finite rise-time square-wave current input at 45 Hz. The material, Hiperco 50, was configured as a magnetic steel with $K_h=74.5$ and $K_e=0.0302$, the same coefficients defined for the MEC model. The resulting average power loss for a cycle was 1.04 W.

The MEC quasi-static loss analysis was conducted using a combination of eddy current loss density and the Modified Steinmetz Equation (MSE) as presented in Sudhoff [34]:

$$\rho_j = k_h f_{eq}^{\alpha-1} \left(\frac{\Delta B_j}{2}\right)^{\beta} f + k_e f \int_0^T \left(\frac{dB_j}{dt}\right)^2 dt \tag{12}$$

where ρ_j is the power loss density by volume of the j-th MEC element, k_h, k_e, α, and β are material properties, f is the driving frequency, T is the period, B_j is the flux density of the j-th element, and f_{eq} is an equivalent frequency defined as

$$f_{eq} = \frac{2}{\Delta B^2 \pi^2} \int_0^T \left(\frac{dB}{dt}\right)^2 dt \tag{13}$$

The material properties are presented by Sudhoff for a variety of materials. For Hiperco50, the material constants were $k_h = 74.5$, $k_e = 0.0302$, $\alpha = 1.08$, and $\beta = 1.86$. The flux densities were smoothed with a moving average for a cleaner numerical gradient and integration. The power density given by equation 12 is multiplied by the volume of the mesh branch. To calculate the total power loss, these individual power losses are summed.

This MEC evaluation gives a mean cycle power loss of 2.4 W, compared to the FEA result of 1.04 W. This is a considerable amount of error. The use of a square-wave driving current could have contributed to error in this calculation. The MSE is intended for excitations that are more sinusoidal, so the use of a square wave could be a significant source of error. The magnitude of 1 – 2 W is insignificant compared to the level of power output considered in the pump model later in this thesis, so this discrepancy is not a concern.

2.5 Experimental Validation

An experimental version of the linear motor was constructed to validate the use of both the MEC and FEA models.

2.5.1 Motor Design

The experimental linear motor was designed to validate the models. Since it was not intended to be part of a pump, it was designed in the simplest configuration possible for measuring the force output. It has two stator poles, wrapped in opposite directions. The remainder of the design parameters are presented in Table 3.

Table 3: Design parameters for linear motor experimental validation

Variable	Value	Description
n_{pole}	2	number of stator poles
R_o	61 mm	stator outer radius

w_{sbi}	15 mm	τ_{net}/R_o
α_{net}	0.98	τ_{mag}/τ_{net}
α_{mag}	0.7	τ_{pmr}/τ_{mag}
α_{pmr}	0.29	R_m/R_o
α_m	0.24	w_{pm}/R_m
α_{pm}	0.14	R_i/R_o
α_i	0	τ_t/τ_{tt}
α_t	0.24	wire diameter
d_{wire}	1.5 mm	number of stator poles
N	100 turns	turns in each coil

A CAD rendering of the linear motor is in Figure 25, and an axisymmetric section view in Figure 26. For ease of manufacturing, the stator consists of four identical sections that were cut on a 3-axis CNC mill out of a 1018 steel 5" rod stock. The stator back iron is oversized to allow ¼"-20 screws to pass through, linking all the stator sections together. The shaft is also 1018 steel rod stock, with grooves cut for the magnets and tapped holes on each end for attachment to a load cell. Teflon bushings are used as linear bearings to support the shaft. The aluminum end caps on each end act as bearing housings and as mechanical stops for the shaft.

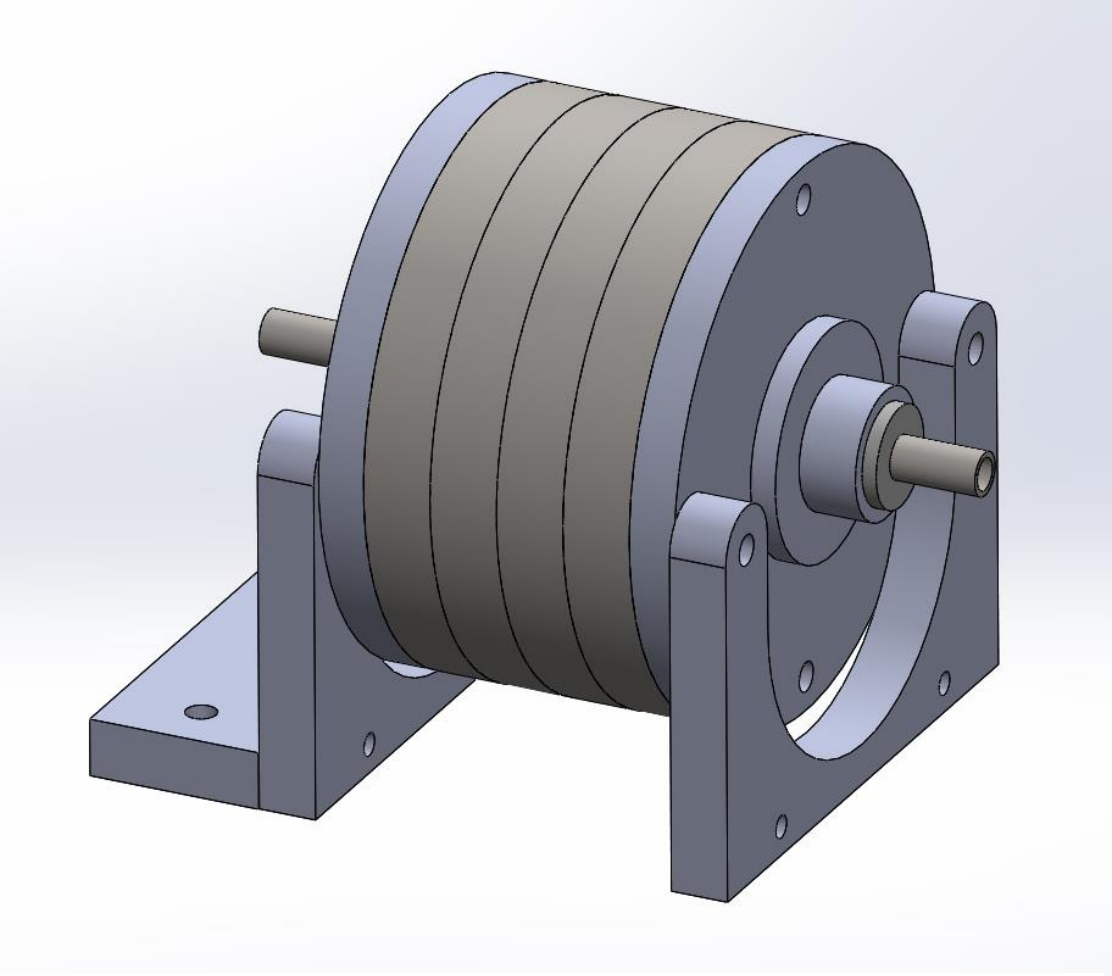

Figure 25: CAD of experimental linear motor and mount

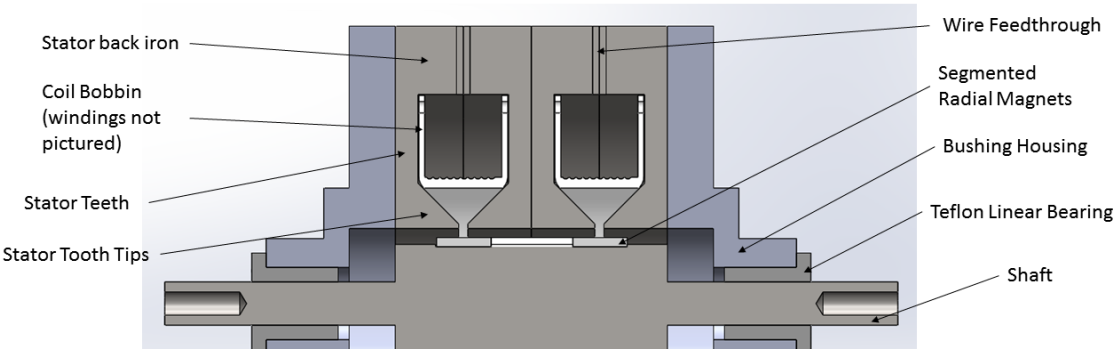

Figure 26: Section view of experimental linear motor

Figure 27 depicts the 3D-printed coil bobbin and wire wrapping placed within the stator section. Note the cutouts that act as feedthroughs for the magnet wire to pass out of

the stator. The winding was wrapped on a lathe. 15 AWG wire was selected for its high current-carrying capacity and to minimize the number of turns to keep the inductance low.

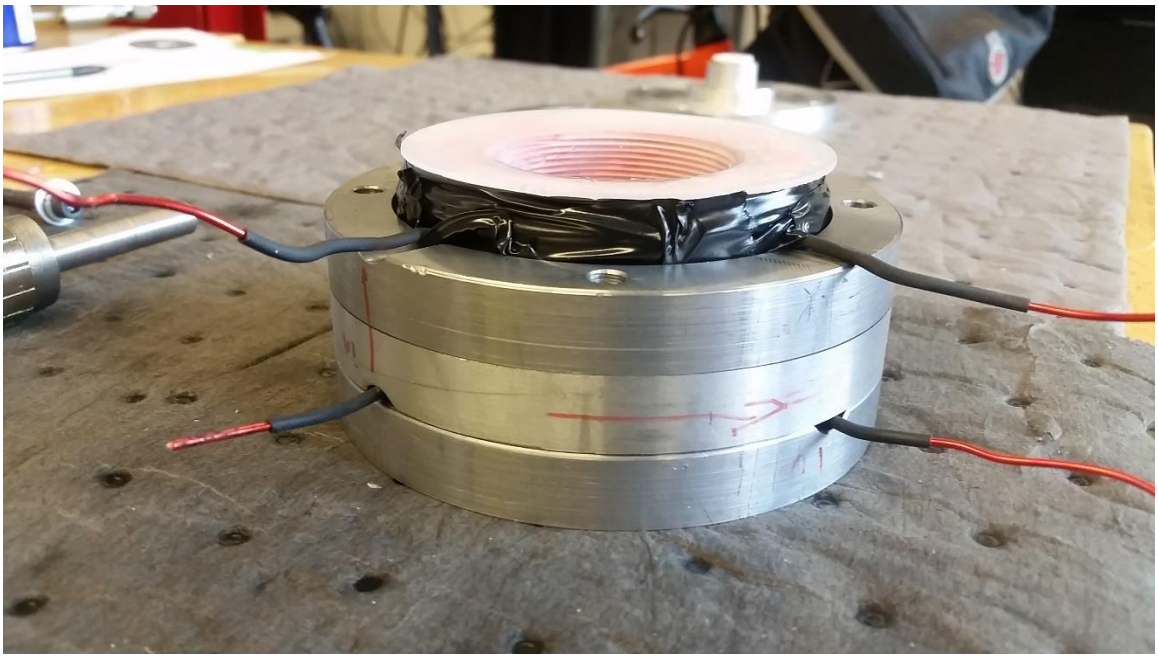

Figure 27: Winding placed within stator section.

In Figure 28, 14 segmented N50 Neodymium arc magnets from Super Magnet Man were fixed to the shaft using Loctite 326, an acrylic adhesive formulated for bonding ferrites and permanent magnets.

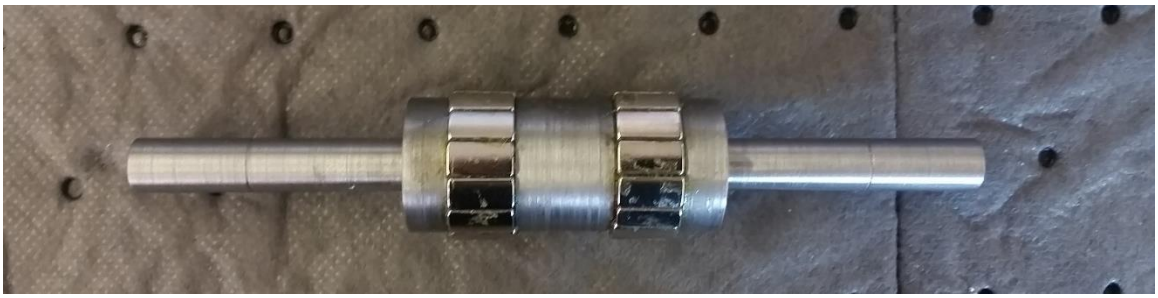

Figure 28: Shaft with N50 magnets adhered

Once the shaft was completed and the stator sections bolted together, the shaft was dropped into place, as shown in Figure 29. The shaft tended to deflect outwards

when the opposite bushing was not in place. The bushing housing was adjusted using shims to ensure collinear alignment between the two bushings and to minimize stiction on the motor shaft.

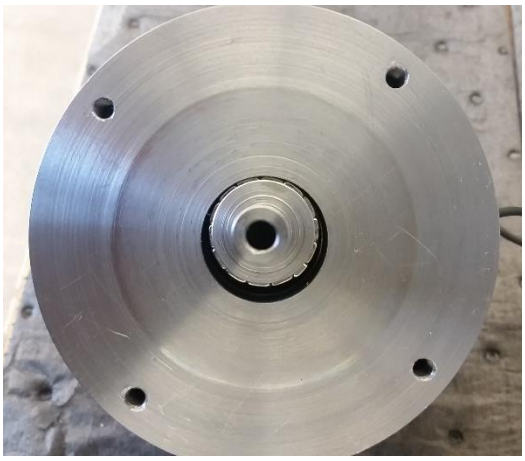

Figure 29: Shaft within stator

2.5.2 Testing

The static force was measured at three different supply voltages and eight different axial positions. To maintain a constant displacement while the motor was under load, the experimental test stand in was built. The vise is used to position the shaft, and the coil is excited by the power supply. A Futek FSH02634 0-1000 lbf load cell was used, with an LT1920 difference amplifier at a gain of 1526 for signal amplification.

The transducer was calibrated at low loads using a set of precision weights to obtain a voltage-weight relationship for eight different points ranging from 0 to 24 lbf. A linear fit was used to find a sensor sensitivity of 93.6 N/V (21.1 lbf/V) at an R^2 of 0.995.

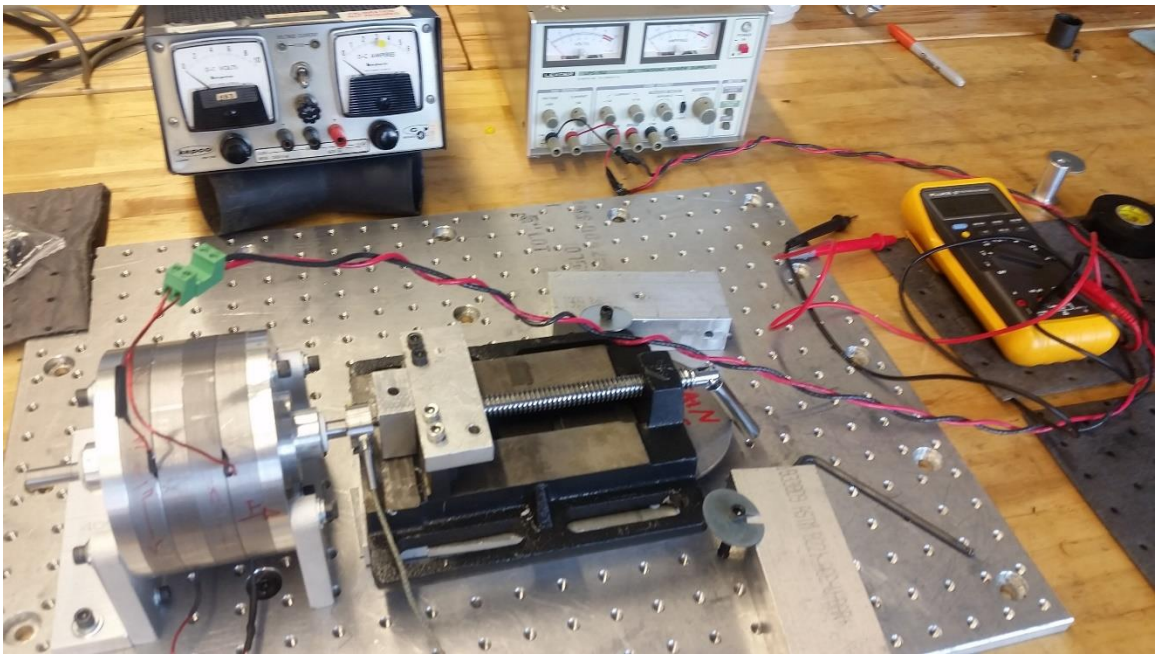

Figure 30: Experimental test stand for linear motor characterization.

The DC resistance of the coil was found to be 0.899 Ω. By supplying voltages of 2.10 V and 3.05 V, supply currents of 2.34 A, and 3.39 A were sent to the motor.

The procedure for measurement was as follows:

1. Ensure supply voltage is at 0.
2. Set shaft position using vise. Unload the vise by reversing the lead screw slightly.
3. Shake the load cell to ensure that no preload is applied to the load cell.
4. Increase voltage to first set point. Record force.
5. Increase voltage to second set point. Record force.
6. Repeat 1 – 5 for each shaft position.

2.5.3 Results

The results comparing measured force-vs-displacement with the FEA and MEC solutions for this actuator geometry are shown in Figure 31.

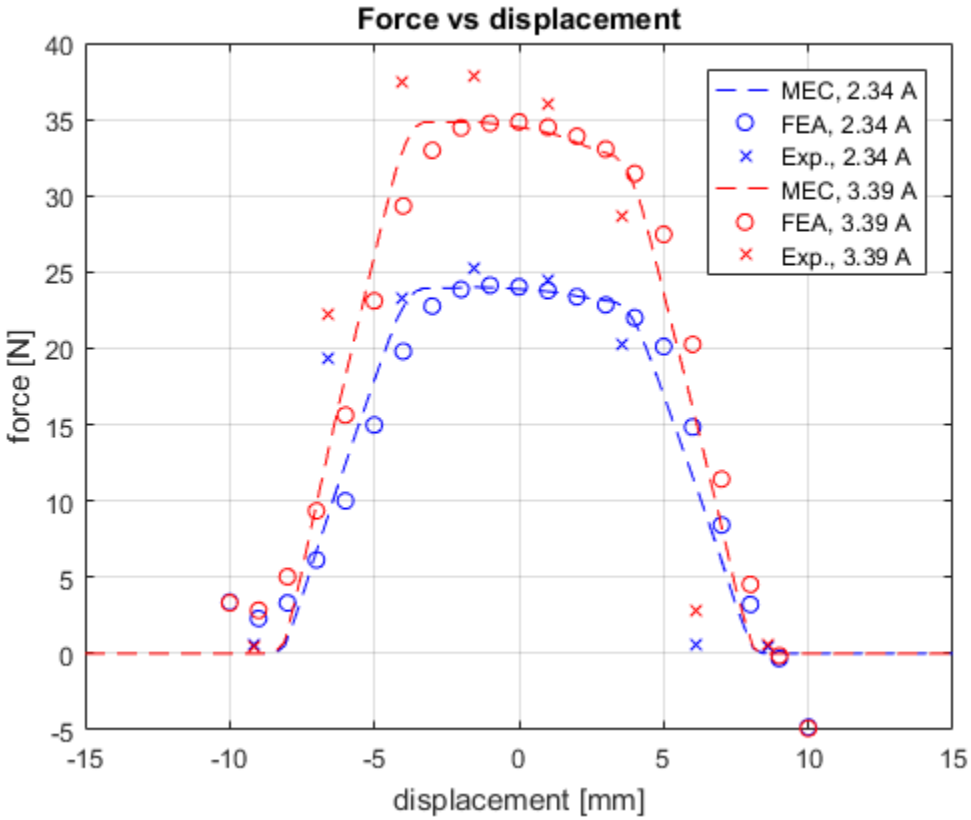

Figure 31: Comparison of experimental, FEA, and MEC force calculations

Based on the results above, the experimental data agree reasonably well with both FEA and MEC. Peak forces generated by the motor are of the same magnitude, with a flat region of force generation of approximately +/- 4 mm. The models predict the fall-off in experimental results well, but there is an offset of about 1 mm in the experimental data. This could be due to asymmetry in the linear motor fabrication. Particularly when the offset is accounted for, the zero-crossing of the motor force is predicted well by both FEA and MEC calculations. The MEC had very little error compared with FEA.

Other discrepancies may be due to the use of segmented magnets as opposed to a true ring magnet, which results in a distortion of the magnetic field in the vicinity of the air gap and unmodeled behavior. Another source of error may be the vise used to position the shaft. Any preload applied to the shaft could translate into an increased or decreased measured force at the load cell.

2.6 Conclusion

The magnetic equivalent circuit has been shown to be an adequate substitute for analytical and finite element techniques for electromagnetic modeling in the linear electromagnetic piston pump. Analytical techniques can be extremely fast, but they require assumptions about motor geometry and material properties that can yield inaccuracies. Finite element analysis is very thorough and provides a large quantity of detailed information, but can be very computationally intensive and is therefore not suitable for use in a design optimization. Magnetic equivalent circuit modeling is reasonably accurate compared to finite element analysis, especially for designs that stay away from magnetic saturation and unrealistic magnet specifications. From a computational time perspective, it is comparable to analytical techniques and orders of magnitude faster than FEA. For these reasons, it is a suitable method for evaluating linear motor properties in a design optimization.

The magnetic circuit showed very good agreement in most cases with the flux density measurements. It predicts the locations of peak flux density within the stator teeth, stator tooth tips, and shaft back iron. With the exception of the stator tooth tips, it also predicts the magnitude of these peaks with good accuracy. In the stator tooth tips, the magnitudes are off significantly. As explained above, this is likely due to the variable area along the length of these branches. Since flux density is inversely related to cross-sectional area, the MEC evaluation is sensitive to where it is being evaluated.

The MEC also showed very good agreement with FEA for force and inductance as functions of shaft displacement. The error was less than 2% for displacements less than about +/- 3 mm. The displacement where the force begins to fall-off is also predicted well, and the error does not substantially increase until much larger displacements. Inductance evaluations maintain less than 3% error for the full range of travel. Most importantly, the MEC and FEA each predict a very flat inductance with a slight, steady decrease as the piston is displaced.

An experimental linear motor was designed to the specifications of a simplified geometry for validating the MEC and FEA models of excitation force as a function of

displacement. The models do a good job of predicting force production from the experimental prototype, in particular the shape of the profile. There are discrepancies in the position of the experimental force fall-off, which is likely to a slight asymmetry in manufacturing or shaft position.

Transient analysis of the cyclic magnetic steel losses in the linear motor using the MEC have a substantial amount of error when compared with FEA. However, just a few Watts of power loss over the course of a cycle is insignificant compared to the linear motor output and the magnitude of other losses in the system.

Overall, the use of an MEC for estimating linear motor performance is very promising for the quasi-static electromagnetic component of the coupled pump model. The model is shown to be very accurate with respect to FEA for a few baseline cases, with solution times several orders of magnitude faster. The model predictions of force output as functions of displacement were experimentally validated with a prototype linear motor.

3 Dynamic Pump Model and Optimization

3.1 Introduction

In this chapter, the dynamic coupled pump model is discussed. The electromagnetic force calculated using the MEC, as discussed in Chapter 2, is used as a driving force in the pump mechanical model. The dynamic coupled model uses a lumped parameter model of the piston and pressure nodes. An Euler-step approximation is used to solve for the time domain system response.

The model was used to 1) optimize the pump parameters for maximum power density and efficiency, 2) explore the design space, and 3) determine the best anticipated performance for the linear electromagnetic piston pump.

3.1.1 Chapter Overview

The first section of this chapter will discuss the lumped parameter dynamic model used to solve for the piston motion and pressure dynamics. The forces acting on the piston and their calculation are presented. The model is tied back to the quasi-static magnetic circuit linear motor force calculation discussed in Chapter 2. The hydraulic circuit and pressure nodes are modeled in the time domain to solve for flowrate and pressure. The model results of the motor actuation force using the MEC and more accurate FEA are compared and found to have very good agreement. Finally, a multi-objective genetic algorithm (MOGA) is used to optimize the design for maximum power density and efficiency. Again, the model results comparing the MEC and FEA force predictions are compared and found to have reasonable agreement.

3.2 Lumped Parameter Dynamic Model

The linear electromagnetic piston pump relies on operating at a resonant condition that is defined by the spring constants of the opposing springs and the moving mass of the pistons and motor shaft. This operating condition maximizes the energy transfer from the electrical domain to the piston, and therefore the fluid, by allowing for a greater piston travel than a steady-state force balance would predict.

3.2.1 Mechanical Dynamics of Piston

The mechanical dynamics model accounts for electromagnetic force, viscous friction, spring forces, and pressure forces. The electromagnetic force is an output of the electromagnetics model and is a function of electrical current sign and piston displacement. Its evaluation is the focus of Chapter 2 and will not be repeated here.

The viscous friction force assumes parallel-plate flow within the clearance seal between the piston and cylinder wall and, using the definition of viscosity, is calculated as

$$F_{drag} = \dot{x}\frac{\pi\mu L_f D}{c} \tag{14}$$

where $\dot{x}$ is the piston velocity, μ is the dynamic viscosity of the fluid, L_f is the length of the clearance seal, D is the diameter of the piston, and c is the radial thickness of the clearance seal. The spring force is calculated using the spring constants of each spring in parallel. The pressure force is calculated as

$$F_{pressure} = (p_1 - p_2)A_{piston} \tag{15}$$

where p_1 and p_2 are the two cylinder pressures and A_{piston} is the cross-sectional area of the piston.

The net force balance on the piston is

$$m\ddot{x} = F_{EM} + F_{pressure} - F_{drag} - k_{eff}x \tag{16}$$

where m is the mass of the piston and k_{eff} is the effective spring constant of two parallel return springs.

3.2.2 Pressure Dynamics

The hydraulic circuit is modeled similarly to the experimental construction documented in Chapter 4. The inlet to the system comes from an atmospheric tank and is split into two lines that are delivered to the two manifolds. The manifold outlets pass through relatively long lines before joining at a tee. An accumulator at the tee smooths out the fluctuating pressure and flow coming from the cylinders to maintain a constant load pressure.

3.2.2.1 Model construction

The pressure dynamics model uses lumped pressure nodes for the hydraulic circuit pictured in Figure 32.

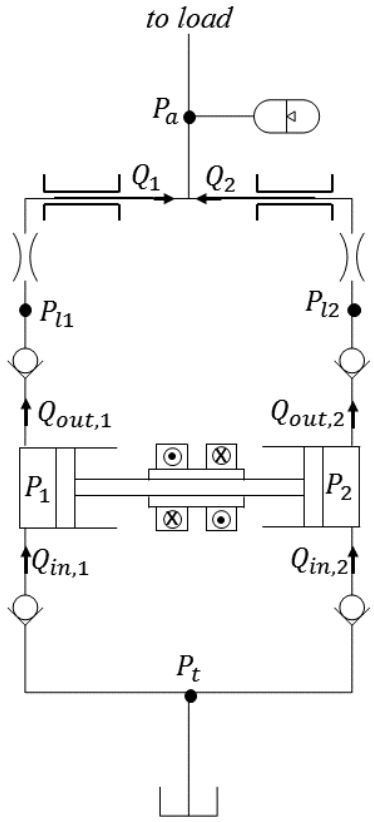

Figure 32: Hydraulic schematic as modeled

The tank pressure is assumed constant atmospheric, and is located immediately upstream of the inlet check valves. The accumulator pressure is assumed constant at 6.9 MPa. A pressure node is located immediately downstream of the outlet check valve. The fluid volume assigned to this node is half the volume of the inertance tube. The inertance is in series with a pipe loss resistance term, where

$$\dot{Q}_\iota = \frac{p_{li} - p_a - p_{mji}}{I} \tag{17}$$

governs the flow rate delivered to the load. p_{li} is the load pressure on the i-th cylinder, p_a is the accumulator pressure, and p_{mji} is the major loss pressure drop associated with the resistance R.

The rate of pressure change for each pressure node is modeled using the definition of the bulk modulus:

$$\dot{p} = -\frac{\beta(p)}{V}(\dot{V} + Q_{out} - Q_{in}) \tag{18}$$

with the effective bulk modulus, *β(p),* given by Cho et al. as

$$\beta(p) = \frac{R + (\frac{p}{p_o} + 1)^{\frac{1}{\gamma}}}{\frac{R}{\gamma}\frac{\beta_o}{p + p_o} + \left(\frac{p}{p_o} + 1\right)^{\frac{1}{\gamma}}}\beta_o \tag{19}$$

where *R* is the entrained fraction of air by volume at atmospheric pressure, *p* is the pressure of the switched volume, p_o is the atmospheric reference pressure, γ is the heat capacity ratio of air, and β_o is the bulk modulus of oil without air [41].

The cylinder clearance seals are assumed to contribute a negligible leakage flow rate to the pressure dynamics, but they are accounted for in the net power output calculation. The check valves are assumed to operate ideally and instantaneously, with a 0.07 bar pressure drop across the inlet and a 0.21 bar pressure drop across the outlet valve at peak flowrate. The cracking pressure is 0.07 bar for each valve. These values correspond with the Hawe check valves used in the experimental setup discussed in Chapter 4.

3.2.3 Model parameters

The solution of the mechanical and pressure dynamics is initialized at zero displacement, zero velocity, atmospheric pressure in the cylinders, and the accumulator at load pressure. An Euler timestep of 0.5 μs was used for numerical integration of the time domain system dynamics. The solution continues until cyclic steady state is reached, defined as when the output power for four consecutive cycles is within 1%.

3.2.4 Model Results

The lumped parameter coupled model was run for a baseline design documented in Table 4, with the linear motor dimensions defined in Figure 33.

Table 4: Design parameters for baseline study

Variable	Value	Description
D	6.00 mm	piston diameter
f	45 Hz	driving frequency
k	20 kN/m	spring constant
n_{pole}	4	number of stator poles
R_o	50 mm	stator outer radius
α_{net}	1.50	τ_{net}/R_o
α_{mag}	0.63	τ_{mag}/τ_{net}
α_{pmr}	0.33	τ_{pmr}/τ_{mag}
α_m	0.35	R_m/R_o
α_{pm}	0.13	w_{pm}/R_m
α_i	0.30	R_i/R_o
α_t	0.50	τ_t/τ_{tt}
d_{wire}	1.35 mm	wire diameter

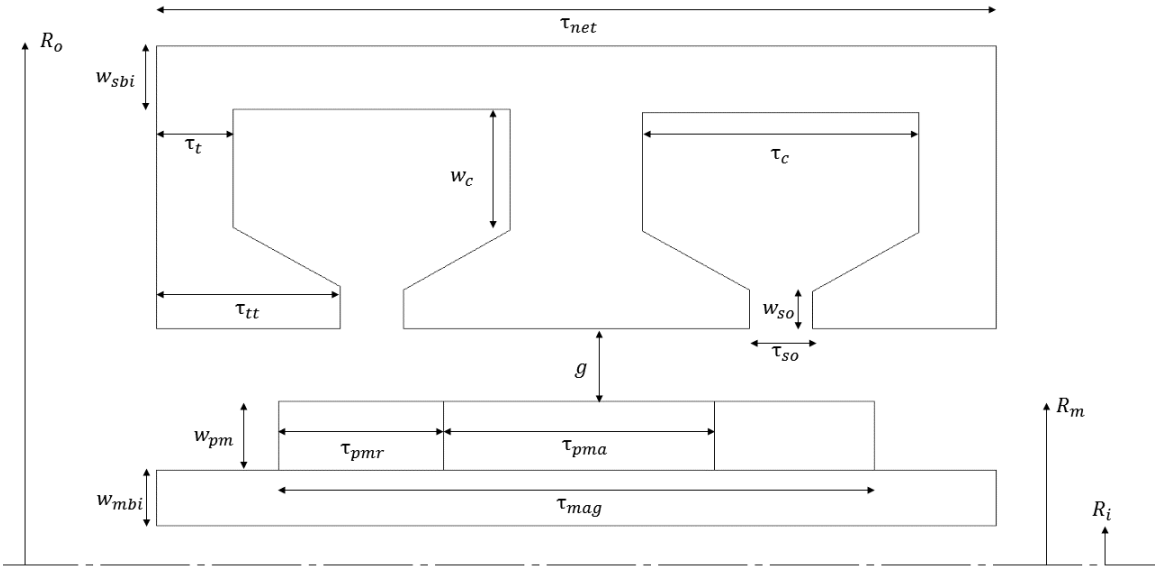

Figure 33: Dimensioned linear motor

The MEC- and FEA-modeled force as a function of displacement for this baseline geometry was discussed in Chapter 2, and is shown again in Figure 34. The agreement is very good for a range of displacements from 0 to +/- 8 mm. The MEC predicts the drop in force accurately at +/- 3 mm. It does not capture the force as accurately for the very large displacements, with error of about 12%. This error is not a concern since the piston does not travel this far.

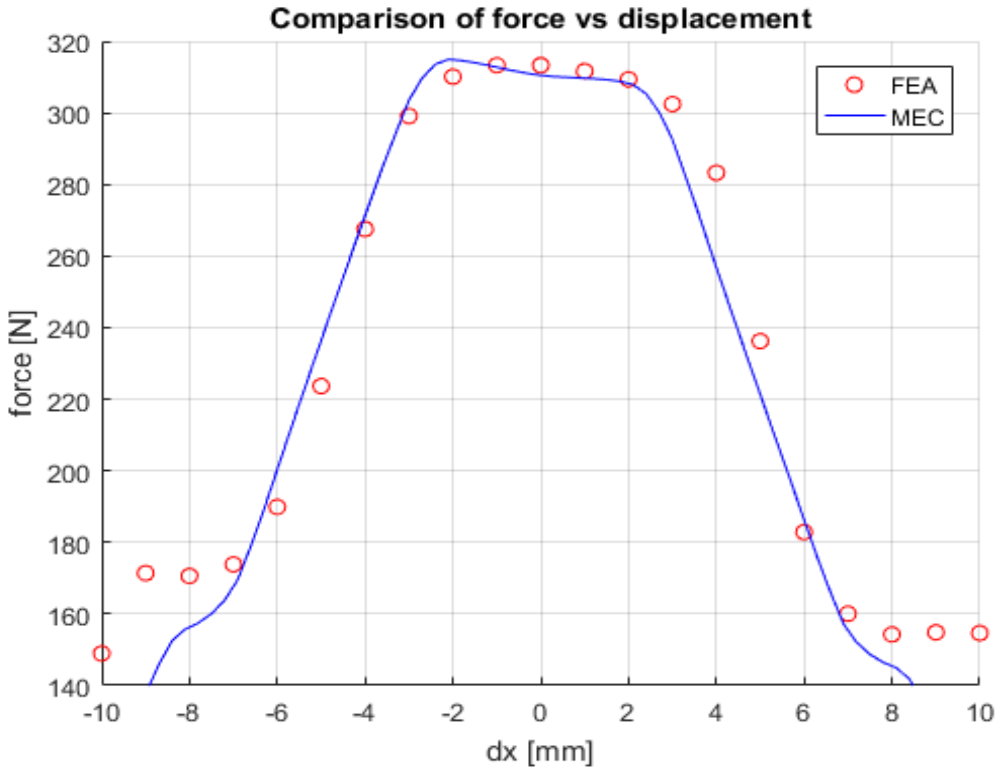

Figure 34: Force vs displacement for FEA and MEC solutions

A comparison of the piston displacement for the use of FEA and MEC force calculation is shown in Figure 35. Despite a small amount of error at peak displacement, the MEC does very well as a force input to the mechanical dynamics model. The MEC-modeled force tends to overpredict the piston trajectory by a very small amount. As a result, the peak velocity is slightly higher in the MEC-modeled case but the difference is not significant.

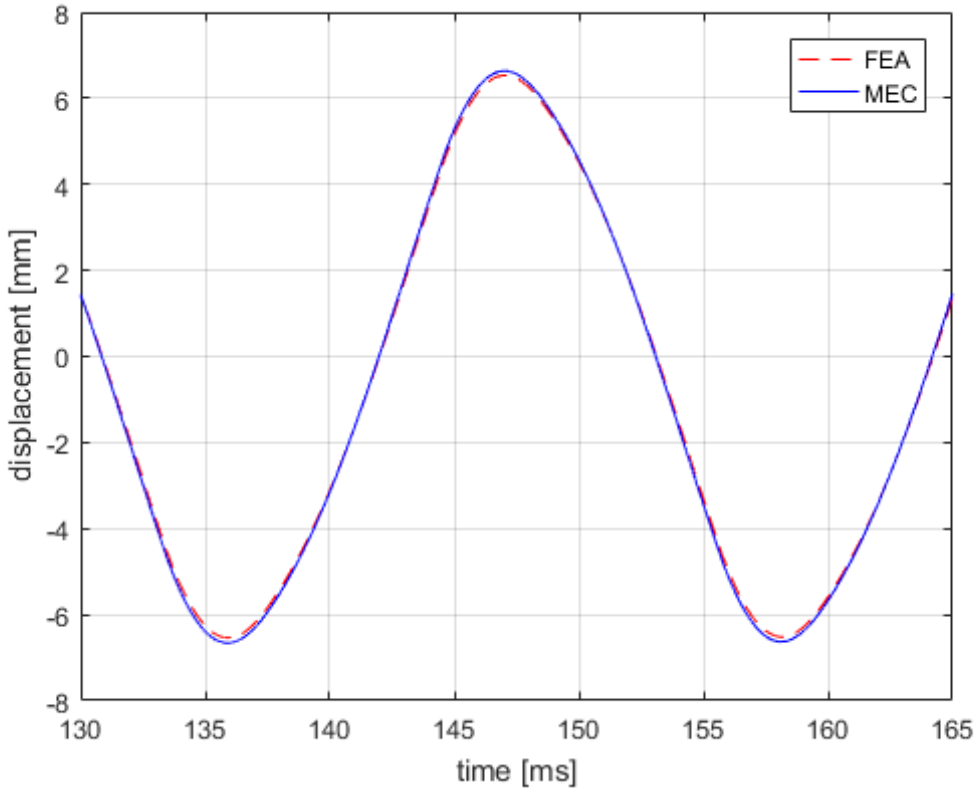

Figure 35: Comparison of piston position vs time for FEA and MEC force models

The pressure dynamics inside one of the cylinders is plotted in Figure 36 for each of the two force models. Again, the agreement is very good. There is virtually no difference between the two pressure dynamics results. The ringing in the cylinder pressure is a result of the inertance of the long delivery lines connecting the delivery check valves to the load.

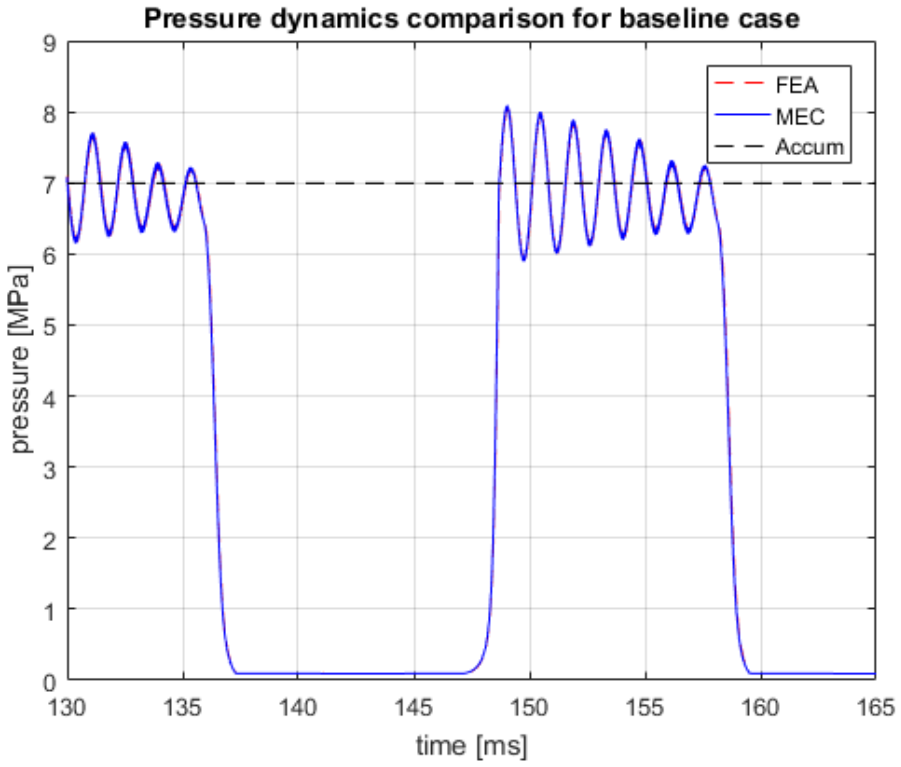

Figure 36: Pressure dynamics comparison between FEA and MEC for cylinder 1

A comparison of the results of the two solution methods is presented in Table 5. For comparison purposes, the Concentric power pack is a commonly used mobile hydraulic power supply at the human power level and has a power density of roughly 0.15 W/cc [9]. This value is estimated based on power output and overall package volume.

Table 5: Comparison of unoptimized results using the FEA and MEC solutions

Parameter	**FEA**	**MEC**	**Error**
Force @ dx = 0 mm	313 N	311 N	-0.6%
Force @ dx = 5 mm	236 N	220 N	-6.8%
Inductance @ dx = 0 mm	82 mH	84 mH	2.4%
E.M. solution time	20 min	1.5 sec	

Cycle power density	0.187 W/cc	0.19 W/cc	1.8%
Cycle efficiency	73%	73%	0.3%

Based on the pressure dynamics, there is very minimal difference between the pump results when using FEA and MEC modeling for the motor force. In addition, Table 5 shows that there is less error in power density and efficiency evaluations than in force or inductance. This suggests that the 6.8% error in motor force evaluation when the piston is displaced does not necessarily translate into a substantial error in the cycle power density. Once the piston is oscillating at resonant frequency and reaches large displacements, the linear motor force is insignificant compared to the large spring force. The MEC predicts motor force very well at zero displacement, where spring forces are zero. The drag forces are at a maximum at zero displacement, since this is when the piston reaches its maximum velocity, but the drag is low compared to the motor force.

3.3 Multi-Objective Genetic Algorithm Optimization

Since the linear electromagnetic piston pump model couples the electrical and mechanical domains, it is expected that the solution space may numerous local minima that would produce challenges for typical gradient based optimization approaches. These challenges could arise from the large number of design variables used, spanning pump and motor definition.

3.3.1 Introduction to Genetic Algorithms

A genetic algorithm uses concepts of evolutionary biology and survival of the fittest to search a design space for the optimal solution. Each generation is composed of a population of individuals that are represented by a string of binary variables that encode the design variables assigned to that chromosome. The design variables associated with each individual are converted into real numbers and used to evaluate an objective function; in this case, the linear pump model. The objective function outputs the fitness of each individual, considering any constraints or penalty factors. Based on their performance in the objective function, individuals are ranked and the least fit are

removed from the population. Remaining individuals can mutate and recombine, much like in the equivalent biological processes. This process continues for a specified number of generations.

Genetic algorithms are well-suited to design spaces that are highly non-linear with discontinuities or contain many local minima because they have a degree of randomness built in. Unlike gradient-based methods, genetic algorithms avoid getting stuck in local minima and seek out the global minima for a given range of design variables. The downside is that there is no convergence criterium or assurance that the optimized solution is the true global minimum. It is often recommended that multiple genetic algorithms be run to confirm convergence to a global minimum.

The algorithm used in this study is the multi-objective elitist non-dominated sorting genetic algorithm II (NSGA-II) as developed in Deb et al. [42] and coded for MATLAB by Sullivan [43]. The multi-objective add-on is based on the genetic algorithm toolbox developed at the University of Sheffield [44]. Elitist strategies ensure that a certain number of the best solutions in each generation are carried over, minimizing the risk that good solutions are thrown out. Non-dominated solutions are those that lie on a Pareto-optimal front, which is a collection of individuals in a multi-objective optimization problem that are superior in one objective to all other individuals with comparable performance in their other objectives. For instance, Figure 37 demonstrates the distinction between dominated and non-dominated solutions for a generic two-objective minimization problem. Objectively, the Pareto-optimal set of non-dominated solutions are all equally better than the remainder of the solutions. There is no way to objectively determine which individuals on the Pareto-front are better than others without making a subjective decision about the value of one objective over another.

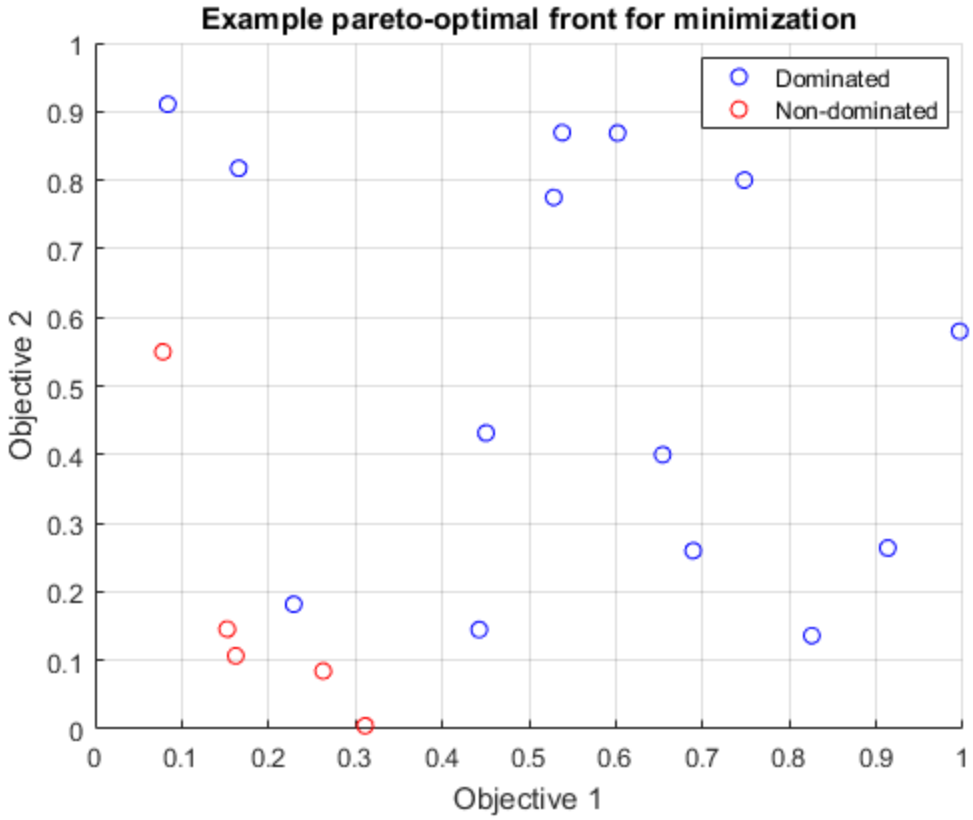

Figure 37: Example Pareto-optimal front for minimization

The primary advantage of the NSGA-II is that it is well-suited to multiple objectives. Other optimization algorithms make an explicit weighting of the objectives to reduce multiple objectives into a single objective. By sweeping a wide array of objective weightings, the optimization will eventually describe the entire front. Since the NSGA-II acts on a population instead of an individual, it builds the entire Pareto front as it progresses through the selection of non-dominated individuals discussed above. In addition, when new individuals are generated, the algorithm attempts to draw them from a variety of objective evaluations along the Pareto front. This maintains diversity in the solutions.

To account for constraints, a penalty factor is applied to the objective function evaluation. In a minimization problem, a penalty factor artificially increases the fitness of

an individual before the generation is sorted into Pareto sets. The form of the penalty factor is adapted from that presented in [34] and is discussed in more detail in 3.3.4.

3.3.2 Design Variables

The design variables and their limits are summarized in Table 6 below.

Table 6: Design Parameters for Optimization

Variable	Units	Range	Description
D	mm	[5, 9]	piston diameter
f	Hz	[15, 150]	driving frequency
k	kN/m	[20, 200]	spring constant
n_{pole}		[2, 16]	number of stator coils
R_o	mm	[30, 70]	outer radius of motor
α_{net}		[0.50, 2.00]	τ_{net}/R_o
α_{mag}		[0.50, 0.90]	τ_{mag}/τ_{net}
α_{pmr}		[0.10, 0.45]	τ_{pmr}/τ_{mag}
α_m		[0.20, 0.70]	R_m/R_o
α_{pm}		[0.10, 0.60]	w_{pm}/R_m
α_i		[0.01,0.90]	R_i/R_o
α_t		[0.10,0.70]	τ_t/τ_{tt}
d_{wire}	mm	[0.70,1.80]	wire diameter

The piston diameter, the driving frequency, and the spring constant are included as important parameters for the pump operation. The mechanical resonant frequency depends on the spring constant, the moving mass, and the pressure dynamics. Using the driving frequency as a design variable allows the optimization to find this resonant frequency on its own. The wire diameter is included to allow the optimization to evaluate the tradeoff between large driving currents and large inductance, since a smaller diameter wire requires more turns and inductance scales with N^2. The remainder of the design

variables are used to specify the dimensions for the linear motor, including its outer radius and length, the magnet length, the magnet and piston radii, the stator tooth width, and the piston bore diameter.

Most of the design parameters for the linear motor were specified as ratios such that there would be natural limits of 0 and 1. The motor outer radius R_o was left in units of length to allow the motor size to scale accordingly. It was found that solutions did not tend towards the limits of 0 and 1, so to speed up convergence of the algorithm to an optimized solution, these limits were reduced to the narrower ranges specified above.

Four motor design variables were left fixed in the optimization. These were the air gap width g, the width of the stator back iron w_{sbi}, and the width and length of the gap in the slot opening, w_{so} and τ_{so}, respectively. Decreasing the air gap provides a significant increase to motor performance by increasing the flux density, but it was found through preliminary FEA studies that for values smaller than 1 mm it resulted in heavy magnetic saturation. This value was left at 1 mm for the optimization. The stator back iron width had a negligible impact on performance and was left at 4 mm for the optimization. The slot opening gap had an impact on cogging force; larger slot openings resulted in more asymmetry of the motor force, which was undesired, while smaller openings increased the inductance. Since this part of the air gap was a particularly challenging part of the magnetic circuit, it was set to a value that provided good performance in baseline FEA and showed good agreement with MEC models. This parameter can be the study of more detailed FEA in the future.

3.3.3 Objectives

Power density and efficiency, the two maximization objectives used in the genetic algorithm, were calculated based on the cyclic steady state operation of the pump. Cyclic steady state is defined as when the output power for four consecutive cycles is within 1%. To treat the optimization as a minimization problem, the objectives were inverted after evaluation.

3.3.3.1 Power density

Power density was calculated as the output power divided by the total package volume of the linear motor. Output power was evaluated using the mean flowrate at cyclic steady state. The package volume was the cylindrical volume of the full motor outer radius and length. The calculation of power density within the optimization is intended to compare linear motor designs with one another, so the package volume calculation does not account for the pistons, cylinders, or manifolds.

3.3.3.2 Efficiency

Efficiency was calculated as the output power divided by the output power plus the losses. The power losses considered in the efficiency calculation included the viscous drag acting on the piston, leakage flow through the clearance seal, ohmic losses in the motor due to resistive heating, and magnetic losses in the motor steel:

$$\eta = \frac{P_{out}}{P_{out} + P_{drag} + P_{lk} + P_{ohm} + P_{loss,EM}} \tag{20}$$

where the different power terms were calculated as follows

$$P_{out} = Q(p_a - p_t) \tag{21}$$

$$P_{drag} = F_{drag}\dot{x} \tag{22}$$

$$P_{lk} = (p_1 - p_t)\frac{\pi D c^3}{12\mu L_f} \tag{23}$$

$$P_{ohm} = i^2 R_{coil} \tag{24}$$

and $P_{loss,EM}$ is calculated for an MEC as given in [34].

3.3.4 Constraints

To limit the results of the optimization to solutions that could reasonably be designed, the pump was constrained to maximum magnetic saturation and maximum input voltage.

The constraints are applied by multiplying each objective of an individual's fitness evaluation by a penalty factor. This is a simplified version of Lin et al.'s use of a penalty parameter for offsetting the fitness evaluation [45]. For a minimization problem, the penalty factor must be greater-than-or-equal-to 1. Therefore, an individual that meets all the constraints has its fitness evaluated in the Pareto sort as is. If any constraints are violated, then a penalty factor greater-than 1 is assessed to artificially increase the objective evaluation, and therefore decrease the fitness of the individual. The form of each constraint is adapted for minimization from Sudhoff, who defines a sample less-than-or-equal-to function for a maximization problem as [34]

$$lte(x, x_{max}) = \begin{cases} 1, x \leq x_{max} \\ \dfrac{1}{1 + x - x_{max}}, x > x_{max} \end{cases} \tag{25}$$

This function is plotted in Figure 38 for arbitrary values. Note that there is a sharp discontinuity in the vicinity of the limiting value. This enforces a hard cut-off on solutions, forcing individuals to remain within the less-than-or-equal range.

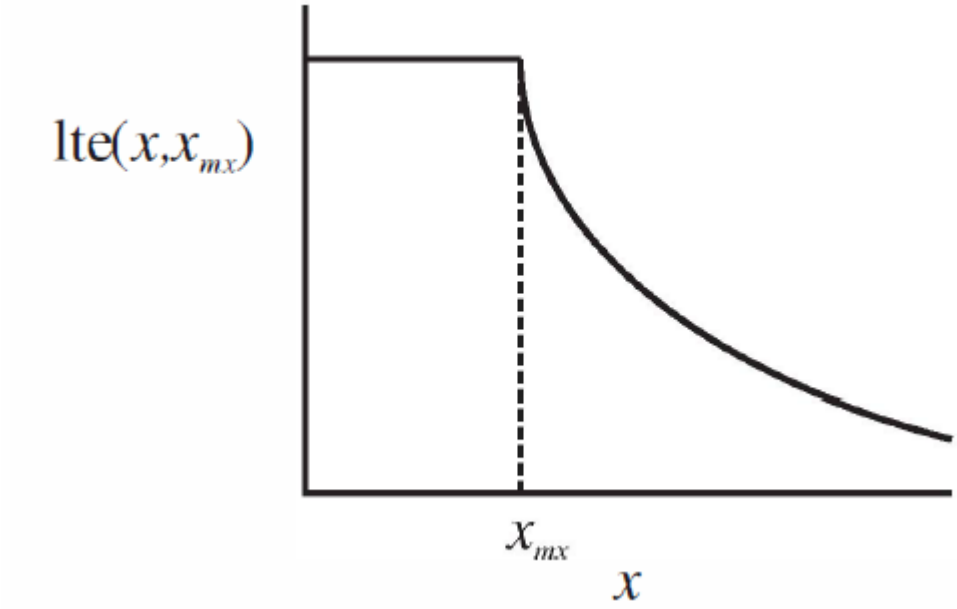

Figure 38: Sudhoff's less-than-or-equal-to function for a maximization function [34]

This thesis used a minimization optimization algorithm, so the minimum constraint was 1. To achieve the same hard cut-off at the constraint, a square-root function was used instead.

3.3.4.1 Maximum flux density

The maximum flux density in any branch of the MEC must be less than 2.07 T, which is the maximum allowable flux density of the Hiperco 50 magnetic steel that was modeled. The maximum is taken as the largest individual branch flux density at any modeled piston displacement. The constraint was evaluated as

$$c_B = \begin{cases} \sqrt{\dfrac{B_{max} - 2.07\ T}{2.07\ T}}, B_{max} \geq 2.07\ T \\ 0, B_{max} < 2.07\ T \end{cases} \tag{26}$$

where c_B quantifies the violation of the constraint. This constraint function is plotted in Figure 39. A discontinuous slope occurs at 2.07 T to discourage solutions that are just over the line.

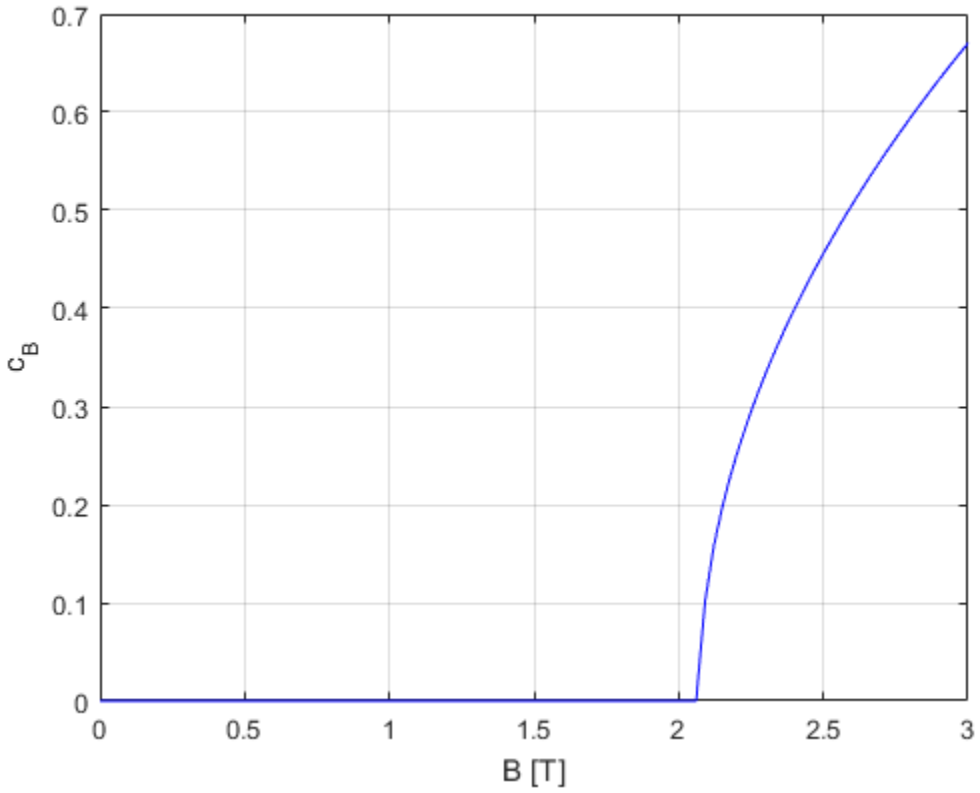

Figure 39: Constraint function for maximum flux density

3.3.4.2 Maximum voltage

Finally, the maximum voltage required to switch the current on and off must be less than 400 V. This quantity was estimated as

$$V_{charge} \approx L\frac{\Delta i}{\Delta t} \tag{27}$$

where L is the motor inductance calculated by the MEC model, Δi is the required current rise, and Δt is 5% of the driving period. This constraint checks that the quasi-steady state assumption for linear motor modeling is still valid. With the inductances modeled in baseline FEA, this was found to be the largest contributor to voltage requirements from the current controller. In addition, this charge voltage typically applies only at piston transitions, when velocity and therefore back-emf are relatively low. The constraint was evaluated as

$$c_V = \begin{cases} \sqrt{\frac{V_{charge} - 400\ V}{400\ V}}, V_{charge} \geq 400 \\ 0, V_{charge} < 400 \end{cases} \quad (28)$$

where c_V quantifies the violation of the constraint.

3.3.4.3 Penalty factor

Since the values for c_B and c_V are normalized, they are weighted equally in the total constraint evaluation. They were averaged into a penalty factor using

$$c_{tot} = 1 + 0.5\varepsilon(c_B + c_V) \quad (29)$$

where c_{tot} is the total penalty factor and ε is a constant that adjusts the weight of the constraints relative to the objectives. The value of ε does not have a significant impact on optimization performance, and was set to 10 for this thesis. Designs which ran into errors, did not reach a magnetic solution, or did not converge to steady state were assigned a total penalty factor of infinity. The value of c_{tot} is multiplied by each value of the fitness. For individuals which satisfy all constraints, c_{tot} is 1 and the fitness remains unchanged. Otherwise, this penalty factor increases the fitness artificially and the solution is less likely to be carried to the next generation.

3.3.5 MOGA Configuration

The MOGA was configured to run 288 individuals per generation for 100 generations. The large number of individuals were required to ensure the large design space was fully explored by the algorithm. The Mesabi supercomputing cluster at the Minnesota Supercomputing Institute was used to allow 24 processors working in parallel to solve for all cases. A full solution took approximately four days. To handle optimization of the discrete n_{pole} design variable, separate optimization runs were conducted with each possible value.

To save computational time and isolate the performance of the pump itself, the check valve outlets were assumed to be at constant accumulator pressure. This change removed the inertance dynamics and delivery major losses, allowing faster dynamic solution. It had a minimal effect on the piston mechanical dynamics. In addition, the

power loss across the check valves was not included in the efficiency calculations because this is a factor that is not directly dependent on the pump design.

3.4 MOGA Results

The results of the MOGA suggest that large improvements to existing mobile hydraulic power supply technology are achievable using a linear electromagnetic piston pump. Figure 40 shows the Pareto-optimal front for the optimized designs. There are two important trends. First, fewer stator pole windings can result in increasingly power dense yet less efficient designs, while increasing the number of stator pole windings will result in more efficient but less power dense designs. The second trend is that larger diameter, lower frequency designs tend to be more efficient and less power dense than their smaller diameter, higher frequency counterparts. This is likely due to the lower frequencies corresponding to decreased losses, which are proportional to the piston velocity.

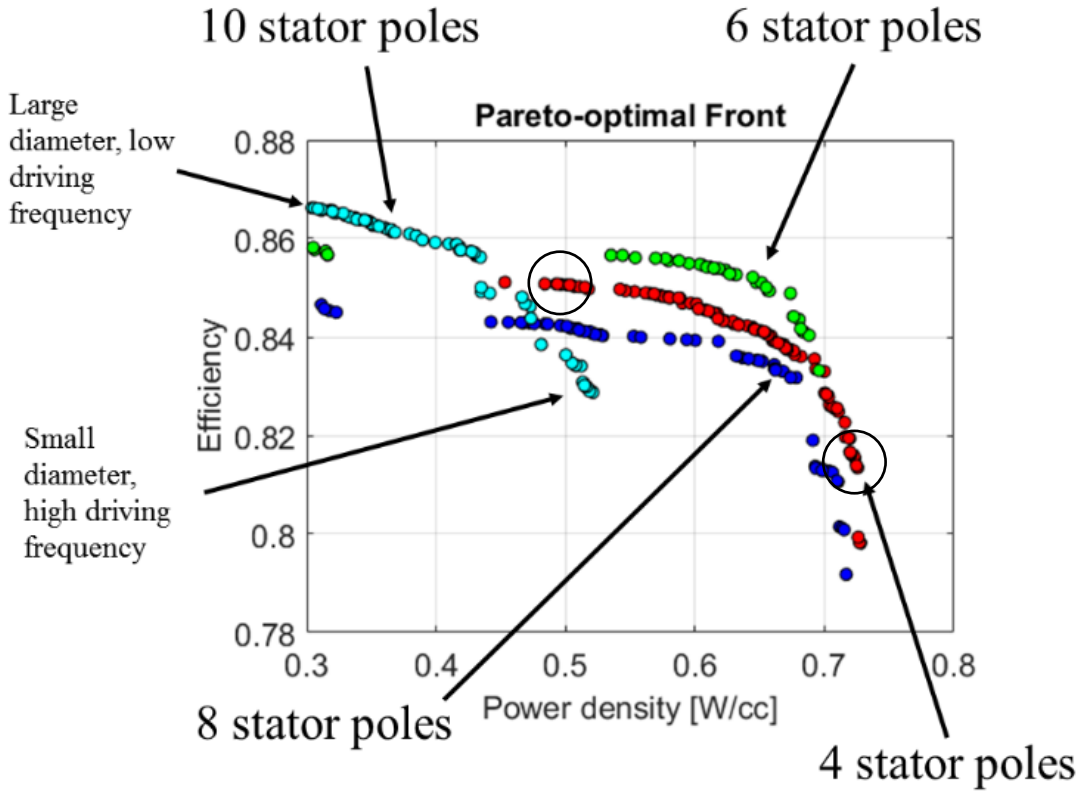

Figure 40: Pareto-optimal front for MOGA

The Pareto-optimal front is a visual representation of the tradeoff between two competing objectives, efficiency and power density. To understand the tradeoff in physical terms, two optimal designs for the 4-pole optimization are examined in more detail. The first is a high efficiency, low power density design circled at left and the second is a low efficiency, high power design. The 4-pole designs are chosen because they perform relatively well and are easier to build in FEA. Table 7 provides the design parameters for these two designs.

Table 7:Design variables for sample optimized solutions

Design Variable	Unit	High Efficiency	High Power Density
D	mm	7.47	6.86
f	Hz	75.19	77.15
k	kN/m	132.29	129.91
n_{pole}	-	4	4
R_o	mm	51.78	51.77
α_{net}	-	0.99	0.99
α_{mag}	-	0.76	0.79
α_{pmr}	-	0.34	0.35
α_m	-	0.5	0.46
α_{pm}	-	0.28	0.28
α_i	-	0.44	0.41
α_t	-	0.46	0.46
d_{wire}	mm	1.06	1.50

3.4.1 High Efficiency, Low Power Density

The high-efficiency, low power density case circled in Figure 40 has been modeled using both FEA and the MEC for linear motor force. The comparison is presented in Figure 41.

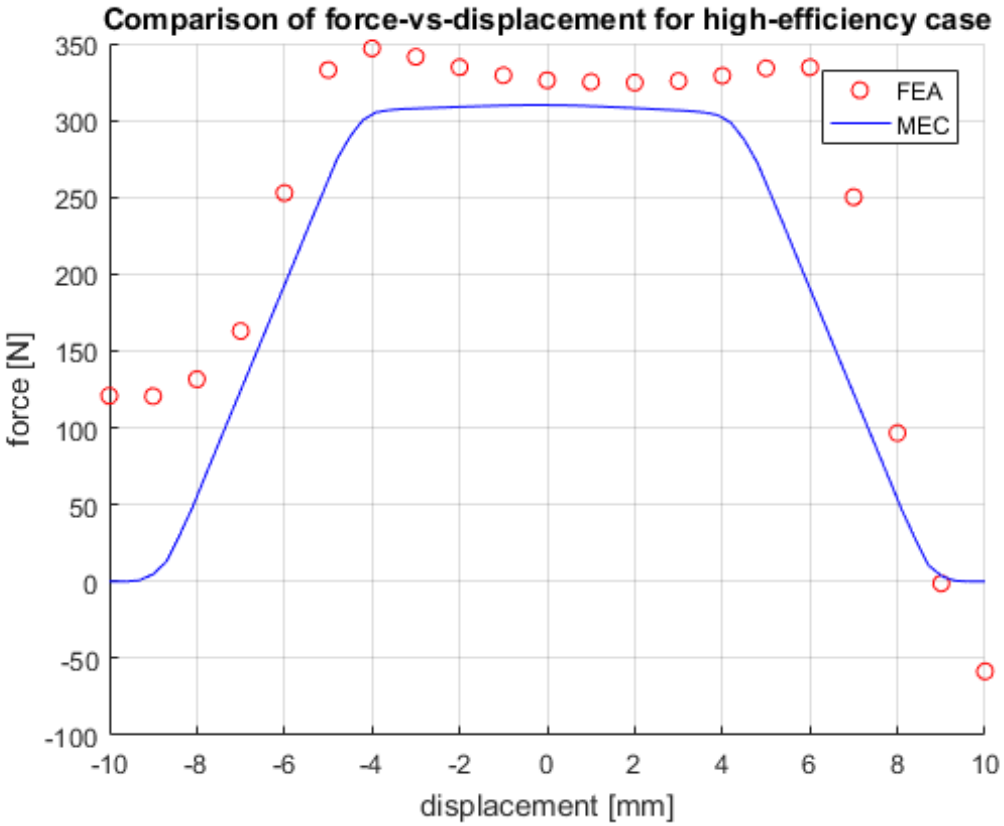

Figure 41: Force vs displacement comparison, high efficiency case

The force evaluation using the MEC is off by 5% at zero displacement and a maximum of 24% at 5 mm. For use in a design optimization, this error is reasonable. In particular, the force evaluation is most accurate at zero displacement, when the motor force is the most significant force acting on the piston. At large displacements, where the error is greatest, the spring forces dominate the mechanical dynamics of the piston. Also, the MEC should be a conservative estimate for total piston output since it is consistently lower than FEA for all displacements of interest.

A comparison of the piston displacement at cyclic steady state for using these two different force models is presented in Figure 42. The increased magnitude of the FEA-evaluated force at all displacements results in greater piston displacements and velocities.

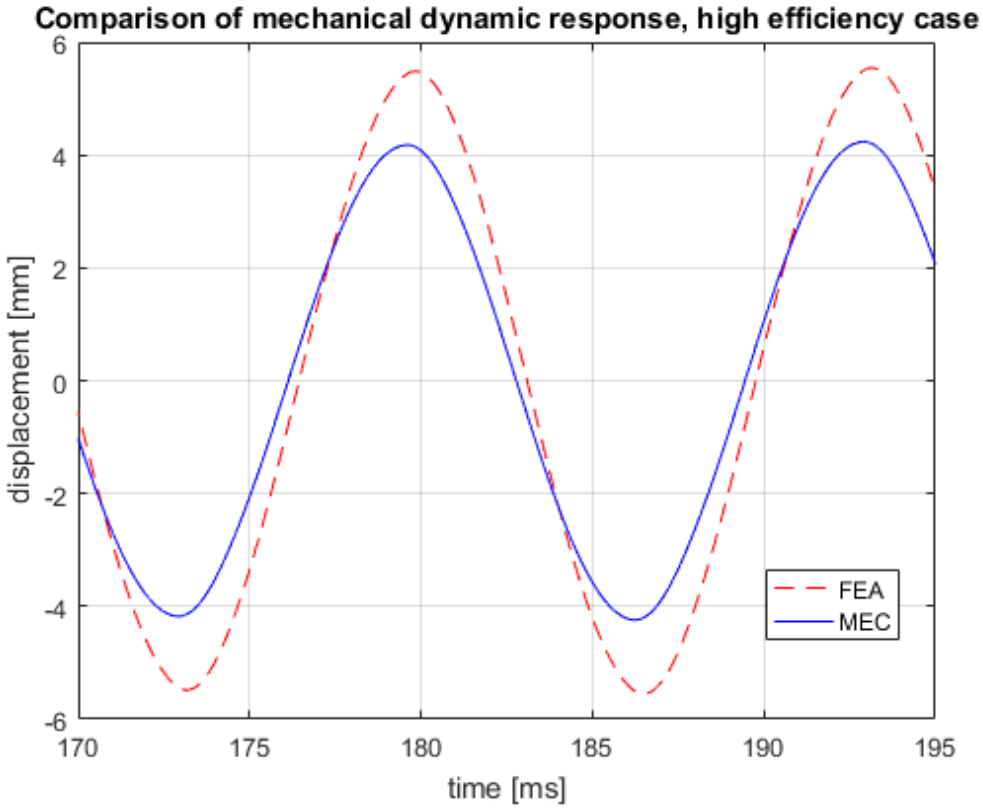

Figure 42: Displacement vs time, high efficiency case

The comparison for pressure dynamic response within cylinder 2 is in Figure 43. For these case studies, the inertance term has been included to approximate mechanical and pressure dynamics as they might manifest themselves in a real prototype with the manifolds separated by long lines. The higher piston velocities calculated by FEA result in slightly larger pressure transients, but the effect is not significant.

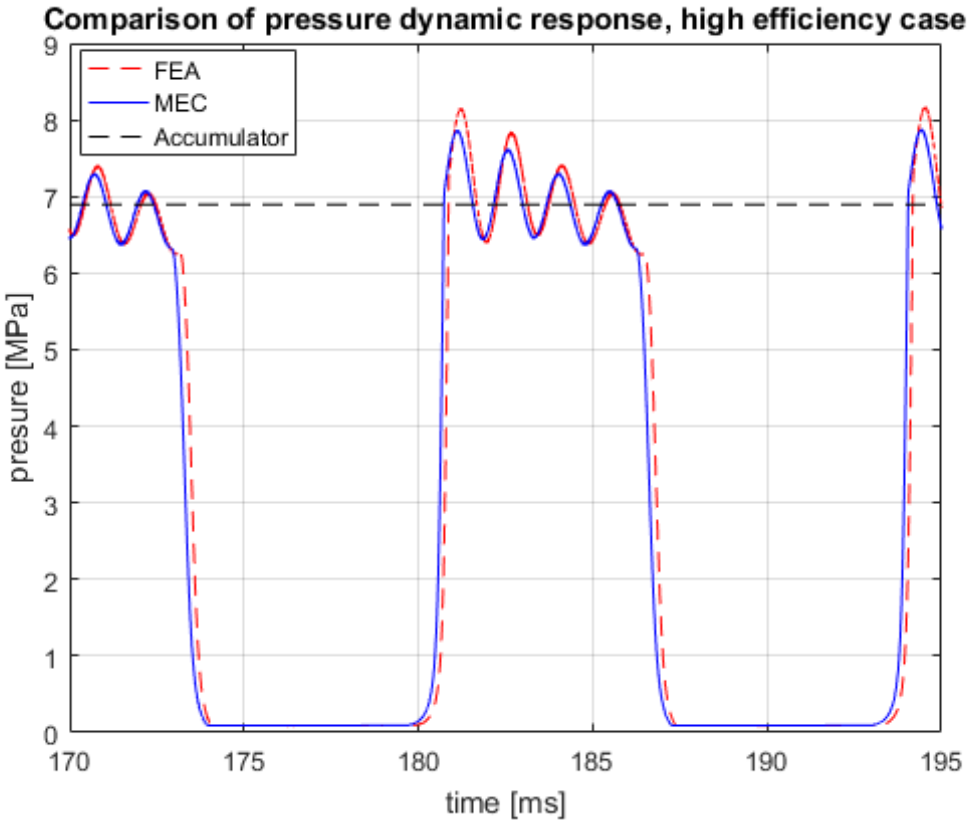

Figure 43: Pressure vs time comparison, high efficiency case

The evaluated results for pump output with an inertance load are in Table 8. The higher force evaluations using FEA result in greater piston displacements and, therefore, greater power density. The inductance evaluation is still reasonably close, so the electromagnetic performance of the MEC-modeled motor should behave similarly to that of the FEA-modeled motor.

Table 8: Pump output for high efficiency case

Parameter	**FEA**	**MEC**	**Error**
Force @ dx = 0 mm	326 N	310 N	-5.0%
Force @ dx = 5 mm	334 N	255 N	-24%
Inductance @ dx = 0 mm	63.6 mH	60.6 mH	-4.7%

E.M. solution time	~20 min	1.5 sec	
Cycle power density	0.60 W/cc	0.46 W/cc	-23%
Cycle efficiency	81%	81%	0%
DC Resistance Losses	5.8%	7.2%	
Viscous Drag Losses	7.9%	6.1%	
Throttling Losses	5.6%	5.3%	

Losses due to magnetic hysteresis, eddy currents, and leakage flow were negligible and on the order of less than 1%. The increased displacement and velocity in the FEA-based dynamics calculation results in increased drag, while the higher pressure transients result in higher throttling losses. Since the linear motors were assumed to have the same electric coils, their DC resistance losses were the same magnitude.

3.4.2 High Power Density, Low Efficiency

The high-power density, low efficiency case circled in Figure 40 has been modeled using both FEA and MEC for linear motor force. The comparison is presented in Figure 44. This motor geometry is nearly identical to that powering the high efficiency case, so there is similarly good agreement at zero piston displacement and increased error at +/- 5 mm. As previously, the error is at a minimum when the motor force is dominating the mechanical dynamics, and at a maximum when the spring and pressure forces are dominating.

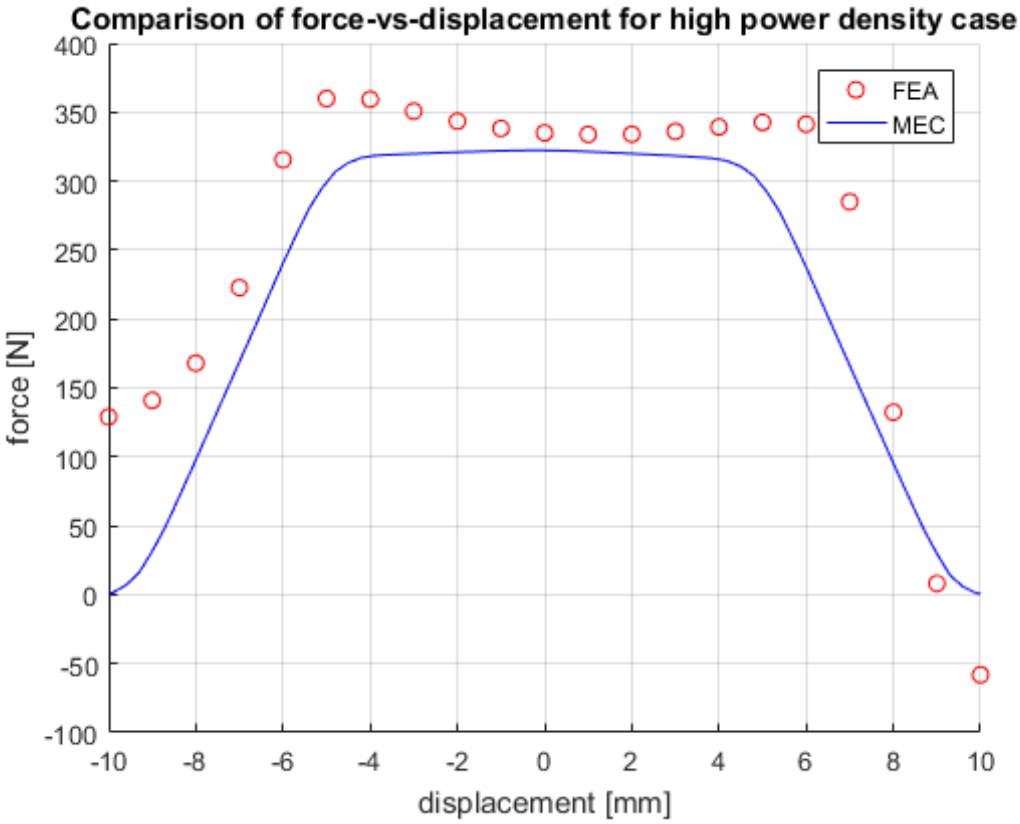

Figure 44: Force vs displacement comparison, high power density case

The comparison for the piston displacement at cyclic steady state is in Figure 45. With a smaller diameter, the piston is able to displace much farther in the high power case than in the high efficiency case. It builds up greater velocities, resulting in higher flow output at the expense of greater viscous drag losses. At these displacements, the piston spends a considerable amount of its stroke at positions where there is high error between the MEC and FEA force. As mentioned previously, since the spring forces are dominating at those displacements the substantial error in force calculation does not translate into equally high error in piston displacement.

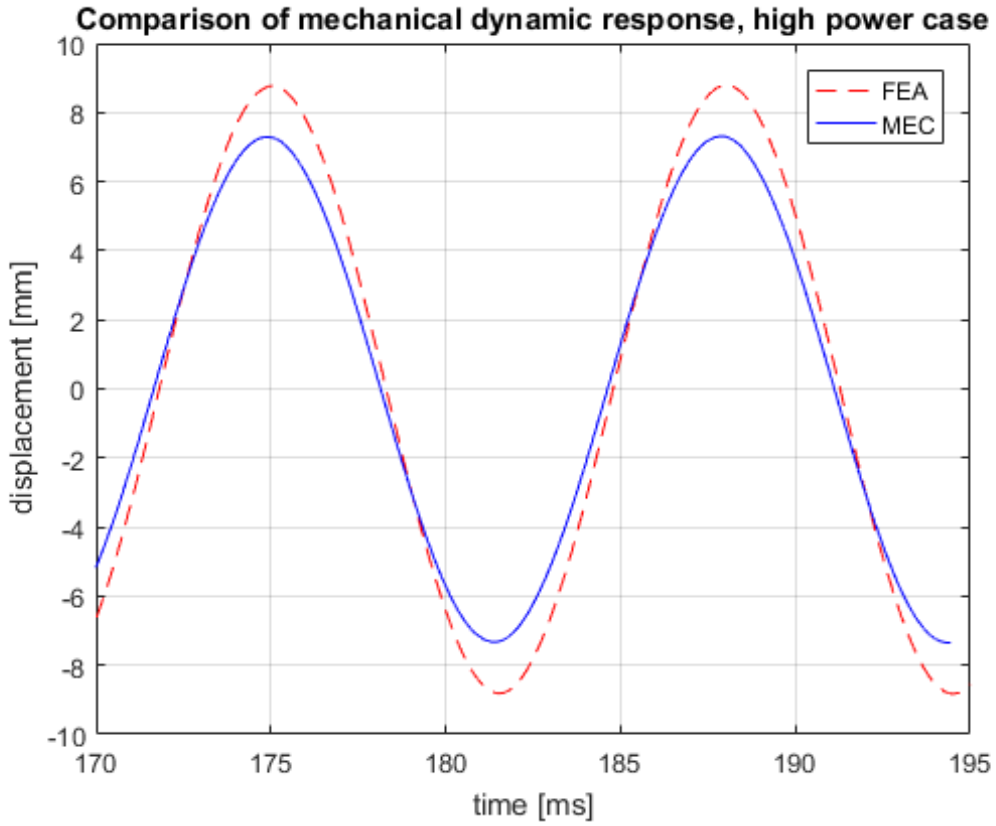

Figure 45: Piston displacement comparison, high power case

The comparison for pressure dynamic response within cylinder 2 is in Figure 46. The greater force calculated by FEA results in larger pressure transients, like the greater piston displacements seen above. The ringing of the pressure within the cylinder, due to the inertance of the delivery lines, is a higher magnitude than the high efficiency case. This is expected due to the larger peak piston velocity. As before, this has a minimal impact on the mechanical dynamics of the piston.

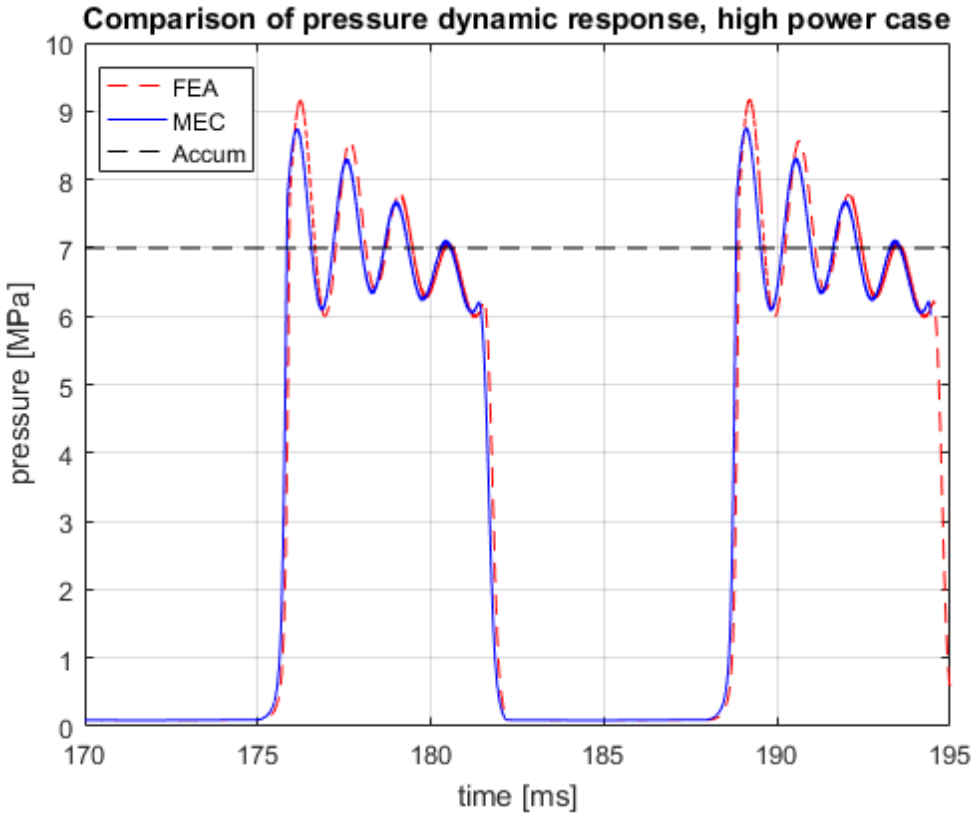

Figure 46: Pressure dynamics comparison, high power case

The evaluated results for high power pump output with an inertance load are in Table 9. As with the high efficiency case, the greater force evaluations in FEA result in larger piston displacements and therefore larger power density. Correspondingly, the efficiency calculated using the MEC force model is higher due to the lower piston velocities.

Table 9: Evaluated pump results for high power density case

Parameter	**FEA**	**MEC**	**Error**
Force @ dx = 0 mm	335 N	322 N	-3.9%
Force @ dx = 5 mm	343 N	295 N	-14%
Inductance @ dx = 0 mm	19.7 mH	18.9 mH	-4.1%

E.M. solution time	~20 min	1.5 sec	
Cycle power density	0.79 W/cc	0.66 W/cc	-16%
Cycle efficiency	76%	78%	2.6%
DC Resistance Losses	4.7%	5.8%	
Viscous Drag Losses	12.9%	11.1%	
Throttling Losses	6.2%	5.4%	

In the high power case, viscous drag is easily the highest source of power loss. Since the power lost due to drag is proportional to the square of velocity, the FEA-modeled pump takes a particularly severe hit to efficiency due to its larger amplitude piston oscillations. Contrary to the high efficiency case, the DC resistance is now on the lower end of loss mechanisms.

3.4.3 Discussion

The Pareto-optimal front shows the tradeoff between the efficiency and power density. The optimization provided designs along the entire front for a reasonable range of efficiency and power density results. As seen in Figure 40, the tradeoff between efficiency and power density is minimal. Increasing the power density substantially results in a very minimal decrease in efficiency for most of the range of optimized solutions. For instance, for 4-pole motor designs, a 40% increase in power density from 0.5 to 0.7 W/cc only suffers an efficiency drop from 85% down to 83%.

As mentioned in the beginning of this section, the primary difference between the efficient and power optimized designs is in their piston diameters. Larger pistons, and therefore smaller displacements, velocities, and losses, are associated with higher efficiency. Smaller, higher frequency pistons are more power dense because they can achieve larger displacements. Since many losses scale with velocity, most notably the viscous drag, these larger displacement oscillations are more lossy as well.

The MEC and FEA force calculation models have decent agreement on the optimized solutions. The modeled force is only off by about 5% at zero displacement, and it predicts the total travel of the motor reasonably well. However, the magnitude of the force at +/- 5 mm is off by a substantial amount. The FEA predicts that there will be peaks in the motor force at around these displacements, but the MEC does not capture these at all. The substantial error at large displacements is not a significant concern because the spring and pressure forces become larger than the motor force. For instance, the high power design uses a spring constant of about 129 kN/m, or 129 N/mm. With two springs in parallel, this equates to an equivalent spring constant of about 260 N/mm. At just 5 mm of displacement, the spring force is over three times the motor force predicted by FEA.

Inductance predictions are good, staying within about 5% in each optimized case. This suggests that the square-wave current input modeled using the MEC is achievable.

The power density calculated using the MEC force model has some error as well, but it does tend to underpredict compared to the FEA results. The piston displacement is considerably higher in the FEA-modeled results, which is likely due to the large discrepancy in force evaluation at small piston displacements.

Another byproduct of inaccuracies in force evaluation is higher pressure transients, particularly when an inertance load model is used. The FEA-modeled pressure trace has higher peaks. This accounts for the difference in modeled throttling losses. It likely also affects the mechanical dynamics of the piston, since a significant force on the piston is due to the cylinder pressures, but this effect was overshadowed by the different force evaluations.

The discrepancies in force calculation could be due to a few issues. Primarily, the magnet dimensions that the optimization tends toward are unrealistically thick in the radial direction. As seen in Figure 47, the magnets themselves are of a comparable thickness to the back iron on the shaft. The peak measurements of flux density in the shaft back iron are greater than 2.10 T, which is well into the saturation region for the modeled magnetic steel, resulting in diminished performance. Interestingly, flux density

in the shaft back iron had good agreement to the test case in Chapter 2, but not in the optimized case here. Also, solution of the nonlinear flux equations in the MEC becomes less reliable at very high flux densities. As a result, the maximum flux density found in the FEA analysis is significantly higher than the maximum found through MEC methods.

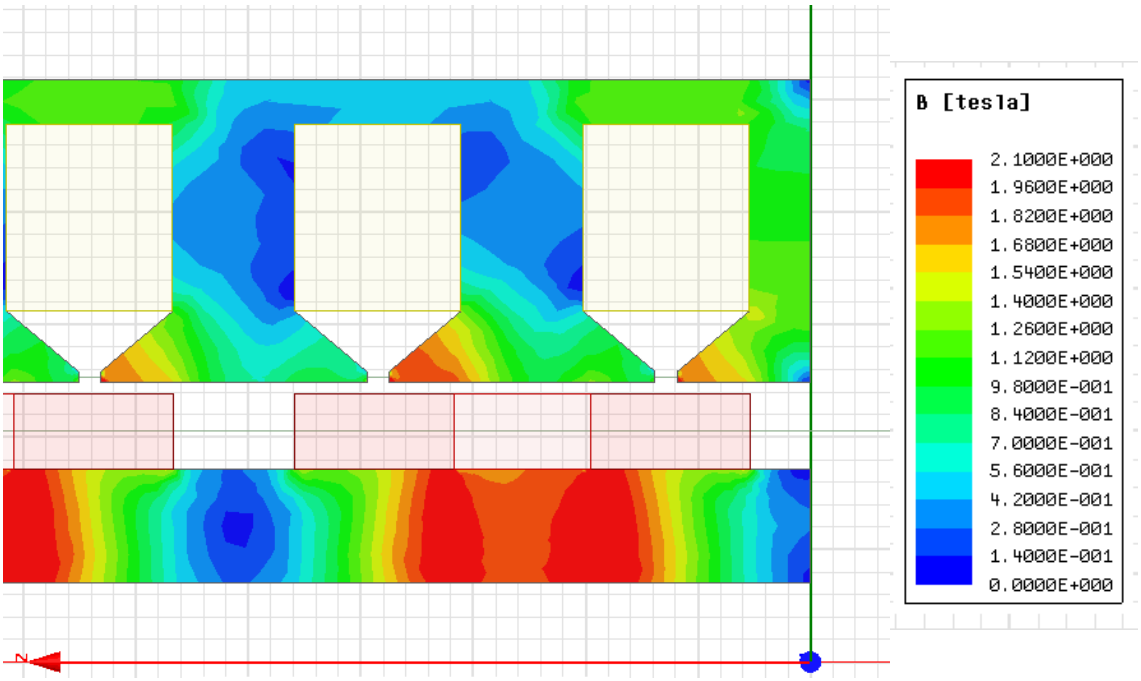

Figure 47: FEA solution for flux density in optimized geometry

A key assumption in the calculation of force was that it was dominated by the change in flux linked by the coils as the piston displaces. This simplified the calculation of force, since the field energy term calculated by the MEC was very discontinuous and did not allow for clean numerical derivatives. This assumption was shown to be valid for the thinner, more typical off-the-shelf radial ring magnets in previous sections. With the thicker magnet, the field energy force term likely becomes more significant. Such a force term is calculable with an MEC, but would require modifications to the model presented in this paper.

In the future, the MEC can be modified to better capture the full mechanics of the force production. In addition, a safety factor may be applied to the flux density constraints to account for the MEC underpredicting the peak flux densities at the stator

teeth. Also, more stringent limits on the range of α_{pm}, the ratio of magnet thickness to outer radius, may be used to limit the radial thickness of the magnet to more reasonable values.

Despite the room for improvement in the force modeling, the results of the design optimization suggest that power density improvements on the order of 400% over a typical state of the art value of 0.15 W/cc are attainable.

3.5 Conclusions

Based on the results presented in this chapter, magnetic circuit modeling may be used for fast solution and reasonable accuracy of linear motor electromechanical performance within a lumped parameter time domain model. For a test case with reasonable dimensions based on available magnet dimensions and materials that compared MEC and FEA methods of solving for excitation force, there was very good agreement in the solution of the mechanical and pressure dynamics of the pump. Inclusion of an inertial element at the load replicated the long lines connecting the two manifolds. This inertance term resulted in ringing of the pressure within the cylinder.

A multi-objective genetic algorithm optimization was conducted to explore the design space and determine the tradeoff between efficiency and power density of the linear pump. For the optimized design, the MEC predicts force at zero displacement within 10% of a more detailed finite-element solution in a fraction of the time. The calculation was off by a larger amount at the limits of motor travel, but the MEC is still able to capture the point at which the force starts to fall off. In particular, the MEC is most accurate when the motor force is most significant relative to the other forces acting on the piston. This accuracy is reasonable for exploring a large design space in a multi-objective optimization algorithm. More accurate solution of optimized solutions may still be done in FEA.

The optimized designs rely on operation at a high frequency, resonant condition to maximize fluid power output. For most of the Pareto-optimal set, there is a minimal tradeoff between efficiency and power density. Power density may be increased by a substantial amount before there is a significant drop in efficiency.

The optimized designs generally have similar dimensions for the linear motor. The main differences between the high efficiency and high power dense cases at either end of the Pareto front is in the pump and piston parameters. The highly power dense designs use smaller pistons to achieve larger displacements, due to the lower magnitude pressure force acting on a small piston area. With larger displacements, power output is increased at the cost of increased drag and throttling losses. The highly efficient designs have larger pistons and therefore smaller displacements. A larger-area piston is able to output more flow per unit stroke, but experiences a larger pressure force so it has a reduced net displacement.

Overall, the optimized solutions suggest that improvements in power density of over 400% compared to a state of the art Concentric pump are achievable using a linear electromagnetic piston pump [9].

3.5.1 Future Work

Future work should continue to validate the numerical linear electromagnetic piston pump model developed here and in Chapter 2. Further detailed electromechanical design of a pump can be conducted using the optimized geometry presented here as a starting point. The detailed design would consist of a full transient coupled FEA model that accounts for the electromechanical performance of the linear motor, the mechanical dynamics of the piston, the pressure dynamics and other components of the highly variable external load on the piston, and the transient electromagnetics solution. The quasi-static approach taken here assumed a constant current input, and a detailed transient analysis would validate that assumption.

Further validation could be achieved using a test bench with a custom tubular linear motor driving a piston pump. Following detailed transient analysis of the optimized geometry using FEA as described above, a linear motor may be designed with integrated pistons and cylinders to minimize excess package volume. Initial experimental testing for mechanical and pressure model validation using an off-the-shelf linear motor is discussed in Chapter 4.

4 Experimental Linear Pump for Model Validation

4.1 Introduction

The linear electromagnetic piston pump uses the piston itself as the moving element in a linear motor. This results in a more compact design with fewer energy conversions, making for increased power density and efficiency. As discussed previously, design and optimization of such a device requires a detailed model for simulating performance as a function of various design parameters. Previously, the magnetic equivalent circuit (MEC) method for electromagnetics modeling was demonstrated to be reasonably accurate compared with finite-element analysis (FEA) for predicting actuator force and inductance as functions of displacement.

To validate the hydraulic model of the coupled linear motor piston pump, an experimental prototype was fabricated using an off-the-shelf linear servo motor coupled to pistons and cylinders in a custom manifold. The objective of this experimental study was to test the performance of the pressure dynamics modeling and to validate assumptions about the performance of different components in the hydraulic circuit. It also served as an opportunity to test the operation of the servo drive in this current-control free piston operation. This experiment used a modular design to permit coupling different linear motors to the pistons and manifolds. This sacrificed compactness, but allowed experimentation with an off-the-shelf linear servo motor and, in the future, custom linear motors.

4.1.1 Literature Review

For a thorough overview of the variety of hydraulic power supplies both available off the shelf and in academic research, the reader is encouraged to revisit the literature review in Chapter 1. The literature review in this chapter will focus on experimental techniques and mechanical design of linear piston pumps and hydraulic power supplies at the human-scale.

In designing the hydraulic power supply for their powered ankle prosthesis, Yu et al. conducted benchtop testing as a validation of predicted performance [4]. Their test

setup uses the prototype powered ankle prosthesis with a constant, high load torque of 43 N*m. The demands on the hydraulic power supply vary as a function of ankle position, which is an input to the system that seems to be determined by the structure of the prototype itself. The performance variables of interest are the motor current, the pump angular velocity, and the pressure difference. Limiting motor current is important to avoid burning out the coils due to excessive heat generation. Current appears to be approximately proportional to the pressure difference. This is expected since current is proportional to motor torque, which is itself proportional to the pressure supplied by the pump. The pump angular velocity is proportional to the measured flow rate.

The authors present a strong proof of concept of the system as a whole. Net efficiency is only 36%, but the system is capable of supplying the pressure and flow needed for the constant torque loading. The experimental results of this test are not compared to any theoretical modeling, although some simulated results for walking on a treadmill are discussed. Also, limited experimental testing of the hydraulic power unit itself is discussed. A pressure-flow rate plot would be useful to fully evaluate the strengths of this design.

Lee et al. experimentally tested a piezo pump with active piezoelectric unimorph valves to validate their electrical, mechanical, and fluid dynamics models [12]. The very fast frequencies used in a piezo pump require accurate modeling of different aspects of the design ranging from velocity profiles to electrical impedance. For accurate input control, they used sinusoidal voltage inputs as opposed to square wave inputs because at very high frequencies, upwards of 1 kHz, the sine wave allows for faster voltage transition. This input is used to experimentally determine the electrical impedance as a function of frequency for comparisons to FEA.

Many of the cryocooler compressors in the literature have been experimentally verified at lower operating power than those targeted by this thesis, but they use a similar linear electromagnetic piston pump concept. In the case of Karunanithi et al., the piston is a separate element that is screwed directly into the end of the moving magnet shaft of the linear motor [16]. A flexure is attached between the piston and shaft to act as both an

axial spring and a linear bearing. The concept of a flexure is better elaborated in Wang et al. [18] Their flexure is a metal sheet with spiraled cutouts to give it a high radial to axial stiffness ratio. This allows it to perform its dual function as a linear bearing and axial spring. The actual material used for the flexure is not published, but it is likely a steel alloy for a higher fatigue life.

4.1.2 Chapter Overview

In this chapter, the design of the experimental linear piston pump will be discussed along with the methodology for testing. Results for pressure and flow measurements will be presented and discussed, and the modeled pressure dynamics will be compared to those found experimentally. The chapter will conclude with a discussion of the key findings and the implications for future prototypes and recommendations for modifications to the model.

4.2 Methods

This section will present the components used and the design of the linear servo-driven pump, the experimental hydraulic schematic, the procedure, and the operating conditions tested.

4.2.1 Component Selection and Pump Design

Several different off-the-shelf linear motors were compared for driving the piston pump. The motors were evaluated based on the desired metrics of high force density, low inductance, low resistance, low moving mass, and simplicity of electrical input. An H2W Tech NCM08-350-45 moving magnet voice coil linear servo motor was selected for this application; a picture of the motor and its performance specifications are presented in Figure 48. The motor is intended for precise positioning applications as a replacement for high load pneumatic actuators. Due to its large moving mass, it is not meant for particularly high frequency applications, but the low impedance and high force allows for a faster electrical response and higher pressure delivery than the alternatives found. Also, the non-commutated design simplifies the power electric drive considerably.

Parameter (as received)	Value	Unit
Stroke	19.1	mm
Moving Mass	1970	grams
Resistance	12.0	Ω
Inductance	6.4	mH
Force @ 100% duty	157	N
Current @ 100% duty	2.0	A
Back-EMF	78.4	V/m/s

Figure 48: H2W Tech NCM08-350-45 linear servo motor and specifications [50]

To accurately recreate the simulated square wave current input used in the numerical modeling, a servo controller was required to perform closed loop current control and to limit the continuous current, which could burn out the motor. An AMC DPE-series servo drive was selected, courtesy of AMC. The drive uses a single-phase, 208 VAC supply and is capable of up to 7.5 A continuous current using pulse-width modulation (PWM) [46]. It uses a built-in shunt regulator to divert overvoltage generated during regeneration events to an external shunt power resistor. A photograph of the servo drive and associated circuitry is shown in Figure 49. A 100 Ω, 225 W power resistor was specified based on the maximum required energy dissipation in a motor braking event in the absence of external system friction. The current and voltage measuring circuit was intended to measure the driving current and voltage sent to the motor, but there was too much PWM noise from the servo drive for this signal to be useful. The ferrite filter was used as a low-pass filter in series with the motor to suppress additional switching noise from the servo drive. Not pictured is a high gage grounding wire to connect the lab bench to the chassis of the servo drive. This was very successful in suppressing PWM switching noise received by the pressure transducers.

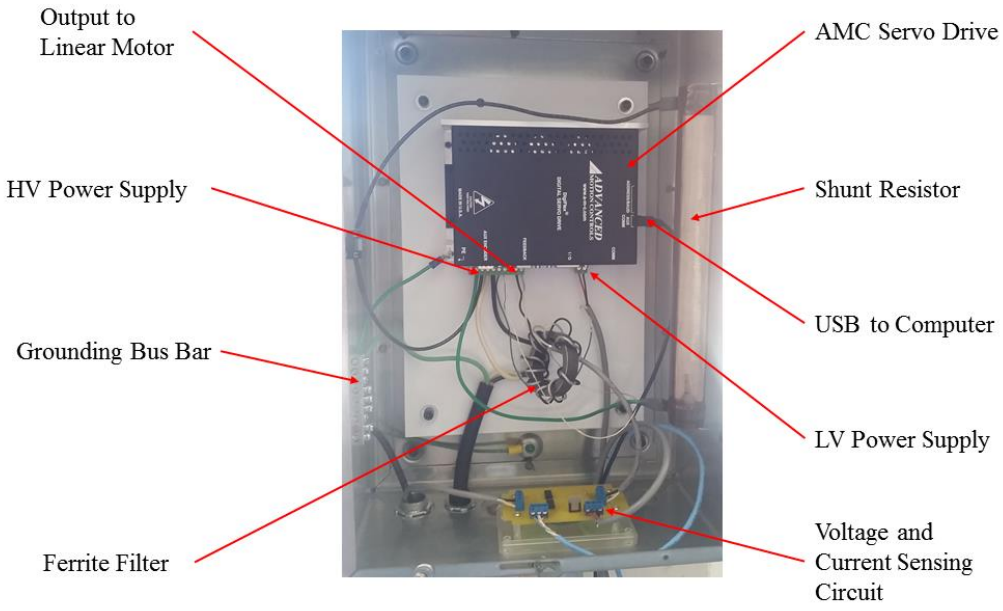

Figure 49: High voltage enclosure for servo drive

The motor can deliver 200 N continuous, at 2.4 A. The target 6.9 MPa of pressure (1000 psi) would require a maximum piston diameter of 6.1 mm. The piston was sized to 6.35 mm (1/4") due to availability. Maximum flow rate was 2.5 lpm, based on peak piston velocity predicted by the model.

Hawe plate style check valves were selected for their compact design and fast response times [47]. RC-1 valves were used for the outlet, with approximately 0.06 bar cracking pressure (0.9 psi) and about 0.8 bar (12 psi) drop at peak flow. RC-2 valves were used for the inlet, with the same cracking pressure and about 0.3 bar (4.3 psi) drop at peak flow. The pressure-vs-flow charts for the check valves is shown in Figure 50.

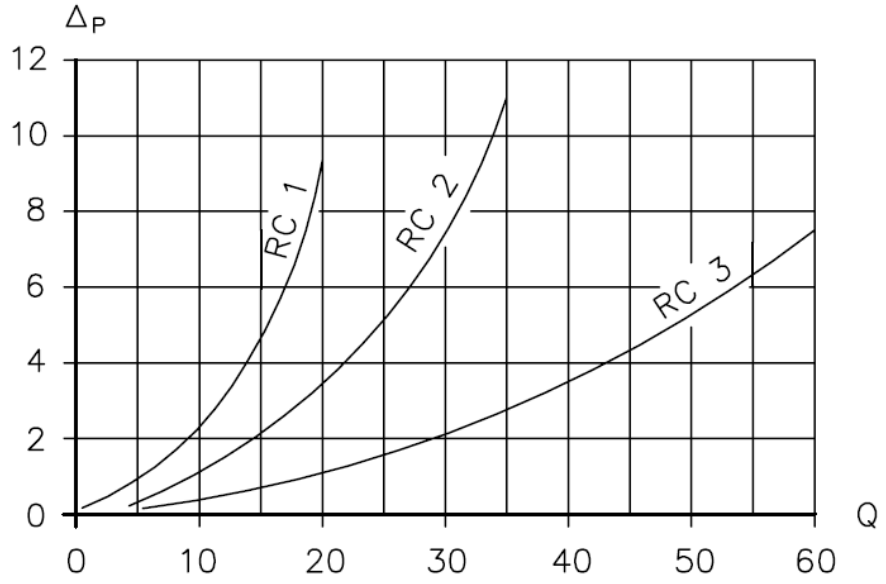

Figure 50: Pressure (bar) vs flow (lpm) of Hawe check valves [47]

An NI PCI 6143 multiplexing DAQ card with +/- 5V analog input and 16 bit resolution was used for data acquisition. Omega PX4201 100-mV transducers were used unamplified to measure pressure at the cylinders, load, and accumulator. Two 0-1000 psig range available on hand were used for cylinder 2 and the pressure immediately downstream of the delivery check valve, hereafter referred to as the “load”. Two 0-3000 psig sensors were used for the other cylinder and the accumulator. Resolutions for the two transducers were 1.5 psi and 4.5 psi, respectively. An AW-Lake positive displacement flow meter was used to measure flow. An MTI Instruments Microtrak laser triangulation sensor (LTS) was used to measure piston position by shining a laser on an aluminum flag attached directly to the piston.

A voltage divider and high common-mode difference amplifier with optical isolation were used to measure the voltage sent to the motor. Likewise, a series shunt resistor and the same difference amplification and isolation were used for current measurements. Since these measurements were located so close to the servo drive, they experienced too much high frequency noise to be used reliably.

The experimental pump was designed with the objectives of minimal dead volume, modular design for experimentation with different linear motors, and simple

parts for manufacture. The CAD view of the assembly is pictured in Figure 51. The linear motor has two cylinder housings on each side, which contain the motor shaft, springs and spring retainers, pistons, cylinders, and high pressure seal. The cylinder housing also contains any leakage through the piston clearance seal. A slot at top allows the flag for position measurement to protrude, and a drain hole at the bottom (not pictured) allows leaked oil to drain. The manifold houses the inlet and outlet check valves and a pressure transducer for cylinder pressure measurements.

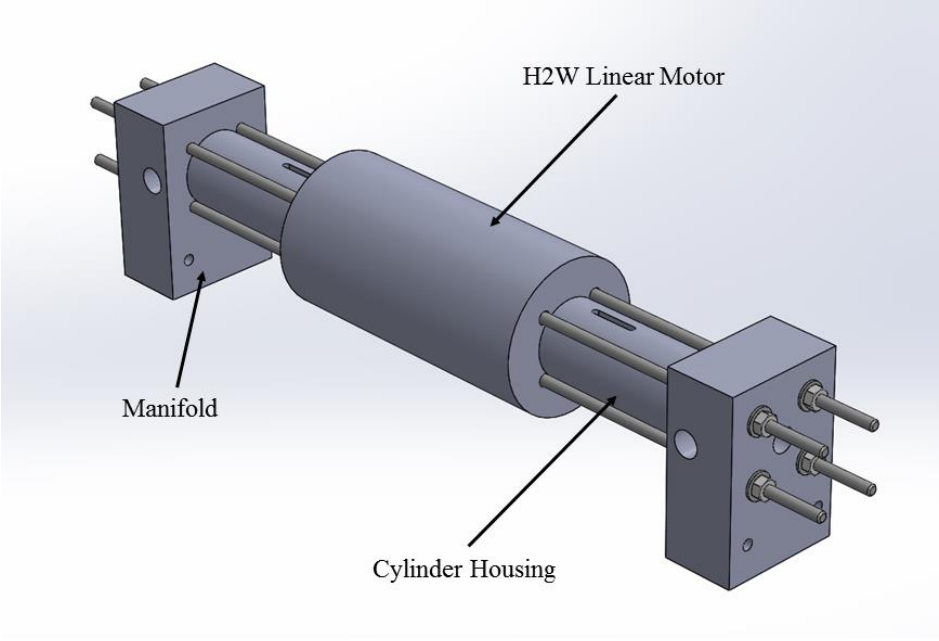

Figure 51: CAD for the experimental pump

A section view of a single cylinder is in Figure 52. The linear motor shaft pushes against the spring retainer, while the spring maintains this contact throughout the piston motion. The piston is a 1.5” long steel threaded dowel pin with an OD of 0.2500” +0.0001”/+0.0003”. The cylinder is a 1.375” long steel drill bushing, with an ID of 0.2500” +0.0001”/+0.0004”. Using these components, the piston-sleeve clearance ranges from an interference of 2.54 µm to a clearance of 3.81 µm. Pairs of dowel pins and bushings were inspected and matched to create a sliding clearance.

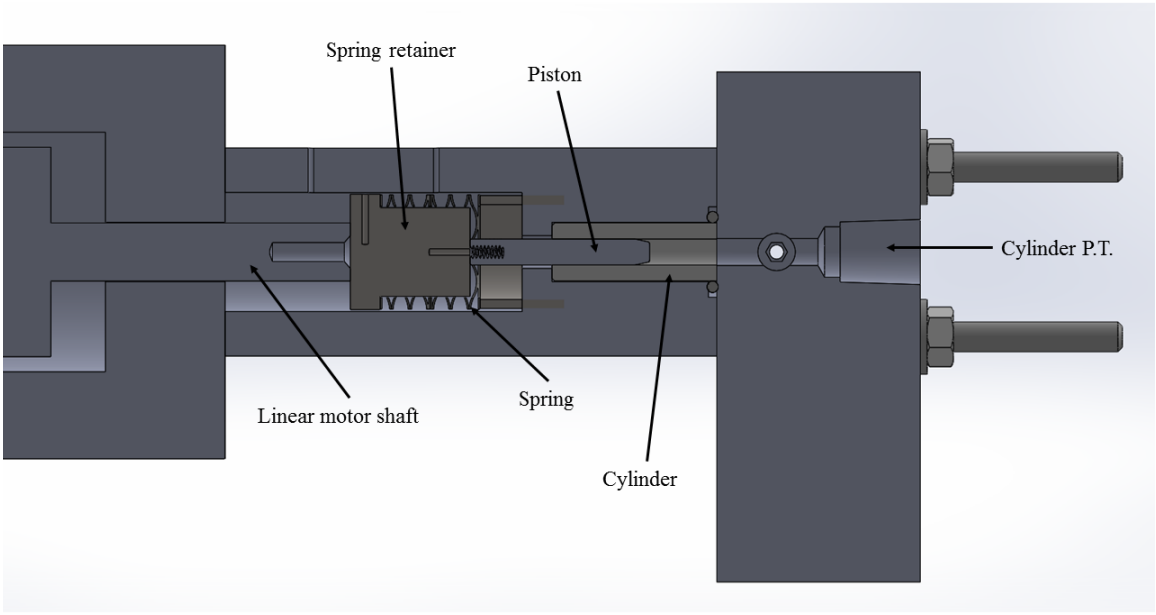

Figure 52: Section view of CAD

Within the cylinder block, the cylinder is allowed to float on a single o-ring that also seals the interface with the manifold and the axial path outside the cylinder. This design was intended to allow the piston and cylinder to self-align and reduce radial loading that could drive up mechanical friction.

The manifold top view is presented in Figure 53. The rectangular 6061 aluminum block was drilled and tapped for the -4 NPT pressure transducer and the two BSPP pipe threads for the Hawe check valves. The valves were located as close as possible to the cylinder outlet to minimize the compressible volume, while maintaining enough material to be structurally sound.

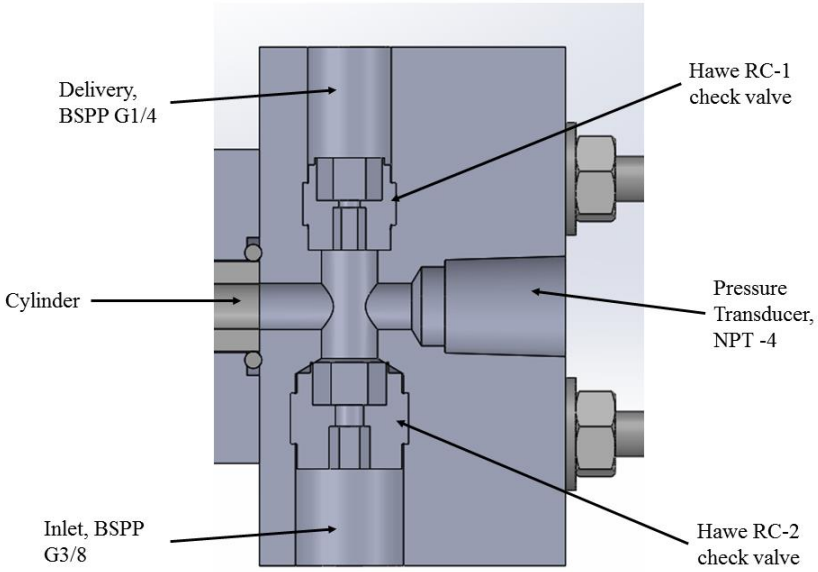

Figure 53: Manifold top view

4.2.2 Hydraulic Circuit

The hydraulic circuit for the system under test is shown in Figure 54 and a photograph of the test bench in Figure 55. The tank is vented to atmosphere and contains approximately 22 liters of ISO 46 oil. The intake passes through a ball valve and analog vacuum gage before splitting for delivery to each separate manifold. As mentioned in 4.2.1, pressure transducers are in each cylinder. The outlet of cylinder 2 has a pressure transducer as well to gain accurate measurements of the pressure drop across the check valve. The outlets of the manifolds are connected with approximately 0.3 m of hose to a cross, with an accumulator, additional pressure transducer, and analog pressure gauge. The accumulator is precharged to 1.72 MPa (250 psi). A flow meter is located downstream of the accumulator, followed by a needle valve and pressure relief valve in parallel. The relief sets a maximum system pressure as a failsafe against over-driving the linear motor, and the needle valve is adjusted as the load. The two branches come together in a tee and pass through a filter before returning to tank.

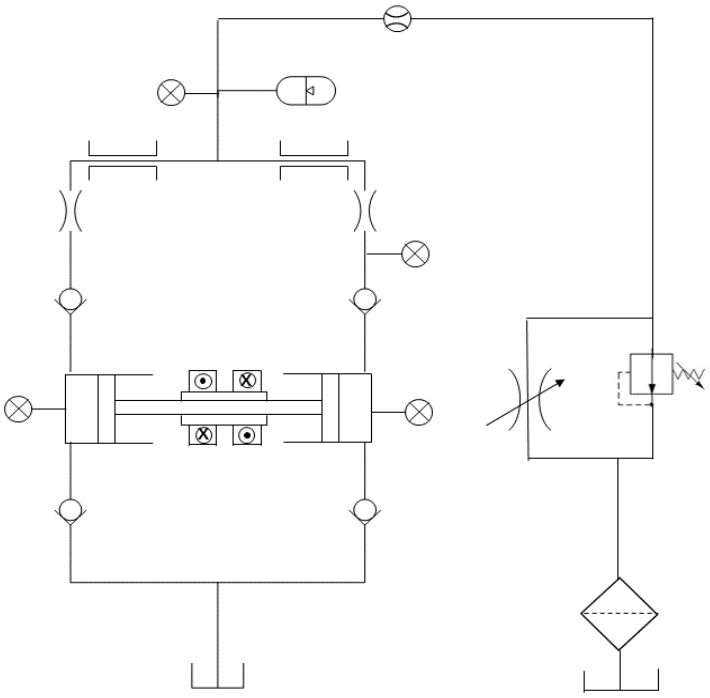

Figure 54: Hydraulic schematic for experimental prototype

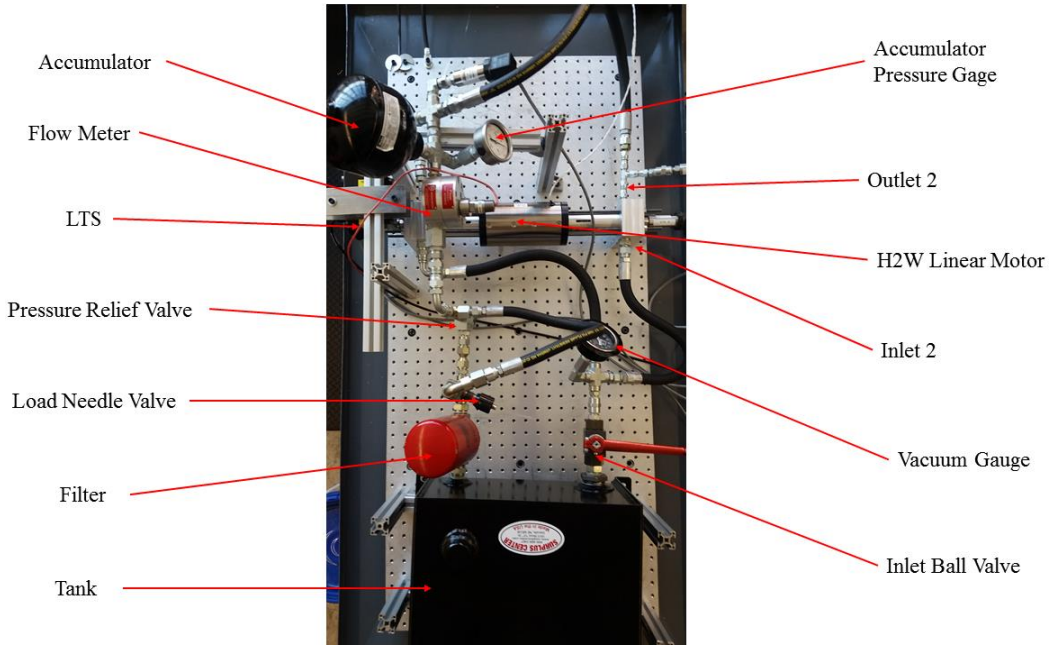

Figure 55: Experimental Test Stand

4.2.3 Procedure

4.2.3.1 Data collection settings

Each sensor signal was passed through a low-pass filter. The cut-off frequency for the pressure transducers and LTS was 3 kHz and the flow meter, current, and voltage was 100 Hz. Since the current and voltage sensing circuits were located within the high voltage enclosure near the servo drive, they saw very high PWM noise. This, along with the low expected bandwidth of the measured signal, meant that a lower frequency could be used for stronger attenuation of the noise. The signals were all received as analog inputs into the DAQ. Further digital processing in MATLAB involved 5-point median and moving average filters to remove the PWM noise in the transducer signals, and a 2nd order Butterworth filter with a 200 Hz cutoff frequency on the flow, voltage, and current signals.

Since the flow meter is located downstream of the accumulator, it is important that the accumulator be at constant pressure for data collection. This indicates that it is

not accumulating oil and that the flowrate measured is the net flowrate leaving the cylinders.

4.2.3.2 Experimental procedure

The experimental procedure is documented below.

1. Open ball valve to tank. Ensure that needle valve is fully open to initialize at zero load.
2. Using AMC DriveWare software, confirm that drive is disabled. Enable waveform generator and switch to current mode. Set a sinusoidal input of 1 A at 10 Hz.
3. Enable the drive. Piston should begin to oscillate.
4. Run at zero load for at least 15 minutes to fully bleed system
5. Increase input to 1.5 A at 10 Hz.
6. Close the needle valve to allow system pressure to build.
7. Once accumulator pressure has built to at least 100 psi, switch to square wave input and adjust current, driving frequency, and load to operating point.
8. Allow accumulator pressure to settle to a constant value. This is cyclic steady state.
9. Collect data. Confirm that accumulator is constant.
10. Lock needle valve. Disable drive from DriveWare.
11. For additional data points, adjust waveform parameters before re-enabling DriveWare.
12. Disable waveform generator.
13. Open needle valve to release built-up system pressure.

4.2.4 Operating Conditions Tested

4.2.4.1 Position and flow rate measurement at varied frequency under no load

The objective of testing under no load was to determine peak flow rates achievable with the pump and to determine conditions for resonant mechanical dynamics. Measurements were taken at different frequencies at no load to determine how driving frequency relates to volumetric efficiency and resonance in the piston displacement. The

volumetric efficiency was calculated based on the piston displacement and flow rate measurements.

4.2.4.2 Position and pressure measurement at varied frequency under load

The objective of testing under load was to observe pressure dynamics in the cylinders, the load immediately downstream of the delivery check valve, and the accumulator. Measurements were taken at different frequencies and the same nominal accumulator pressure to determine how driving frequency relates to power output and efficiency.

Since precise electrical input measurements were not available, input electrical power was estimated by using the mean back-emf and the resistive drop. The mean velocity was found to evaluate the mean back-emf, and the DC resistance used to determine the Ohmic drop. The total motor emf was multiplied by a constant magnitude current of 2 A. This method does not account for $L\frac{di}{dt}$ voltage, but the motor inductance is low so this contribution is negligible. This estimation should be valid for comparisons within these tests, but likely underpredicts the true input power. Output power was evaluated as the product of pressure rise and volumetric flow rate. Volumetric efficiency was calculated as in 4.2.4.1.

4.2.4.3 Detailed results at peak power

The experimental result with the highest output power is documented in more detail, looking at the cylinder pressure dynamics and piston dynamics. The pressure drop across the check valve is examined as it relates to check valve performance and ringing in the cylinder pressure.

4.2.4.4 Model Comparison

The model was configured to use the same parameters as those in the experimental setup to confirm the pressure dynamics and mechanical modeling of the high power output case identified in 4.2.4.3. To model the linear motor input to the system, an approximate force-vs-displacement profile, shown in Figure 56, was used based on the motor manufacturer's specifications for force output at zero displacement and a 30% drop in force production at each limit of travel. Approximate intermediate

values are generated based on manufacturer data for a similar motor, and the curve smoothed by a moving average and fit to a piecewise cubic Hermite polynomial.

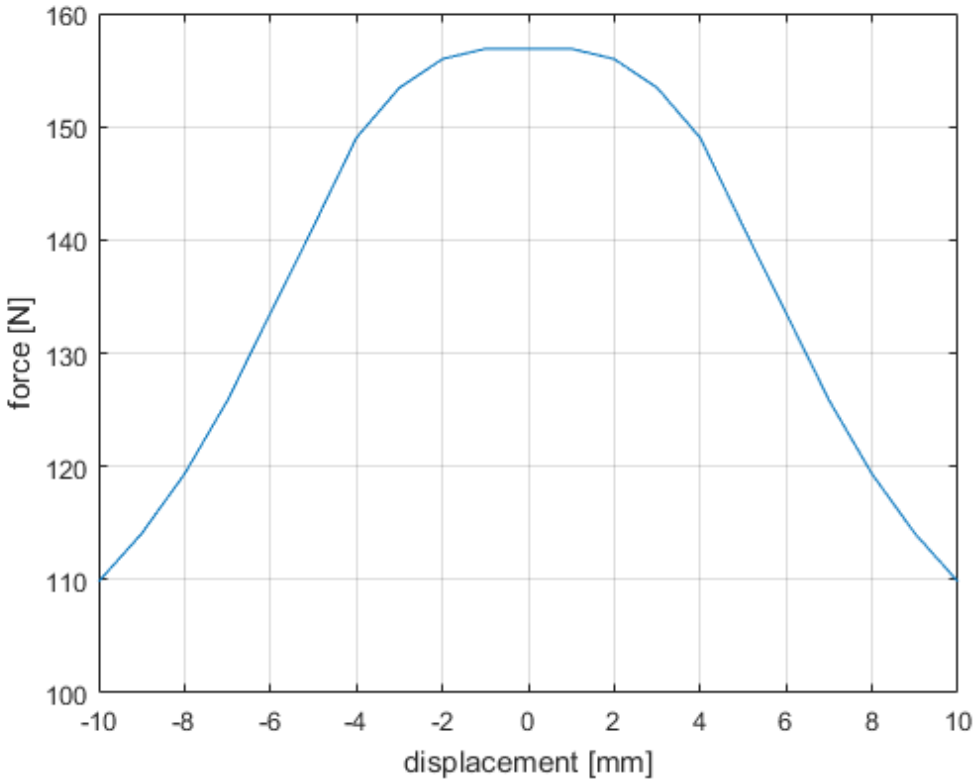

Figure 56: Modeled force-vs-displacement for H2W motor at 2 A

Additional parameters used for the model were a 6.35 mm (1/4”) diameter piston, spring constants of 11.56 kN/m (66 lbf/in) each, a moving mass of 2 kg, which includes the actuator and piston moving masses, and a 21 Hz driving frequency. The inertance and major losses of the delivery lines were modeled based on measurements taken of the physical system. The fraction of entrained air was estimated at 2%. The accumulator pressure in the model was adjusted to match the experimentally measured mean accumulator pressure.

4.3 Results

In this section, the results from experimental testing at various loads and driving frequencies will be presented. The loaded case will be compared with the modeled case for the parameters outlined in 4.2.4.4.

4.3.1 Unloaded, Varied Frequency

The piston displacement and volumetric efficiency are plotted as functions of frequency in Figure 57. To avoid over-extending the piston in the absence of a load, the driving current was limited to 1.00 A.

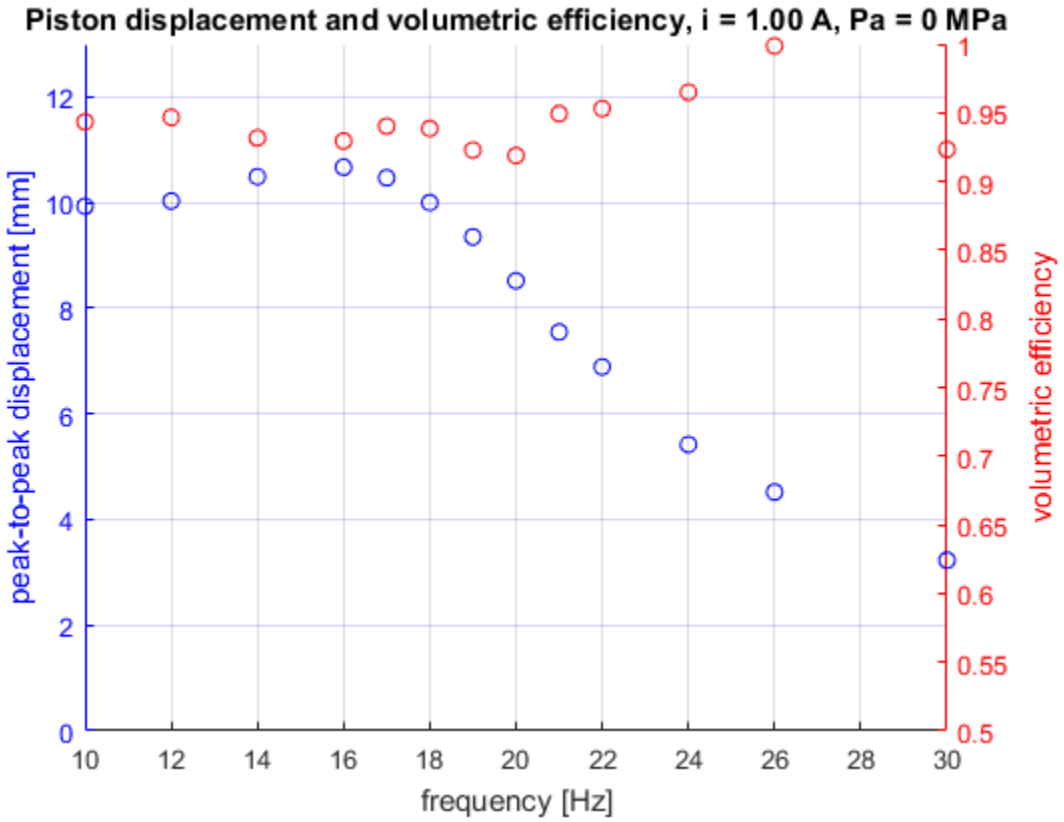

Figure 57: Piston displacement and volumetric efficiency vs driving frequency, 1.00 A driving current at zero load

Based on an effective spring constant of 23.3 kN/m (133 lbf/in) and a moving mass of 2 kg, the theoretical undamped resonant frequency is 17 Hz. Experimentally at zero load, maximum piston displacement occurs at 16 Hz. Volumetric efficiency at zero

load stays high, at approximately 94% for most cases. Maximum volumetric flow rate was 0.642 lpm at 18 Hz and minimum flow rate was 0.340 lpm at 30 Hz.

4.3.2 Loaded, Varied Frequency and Current

The output power and overall efficiency are plotted in Figure 58. The overall efficiency tends to track closely to the output power, with peak output at 21 Hz. The maximum output power was 28.5 W, with the maximum efficiency about 23.6%.

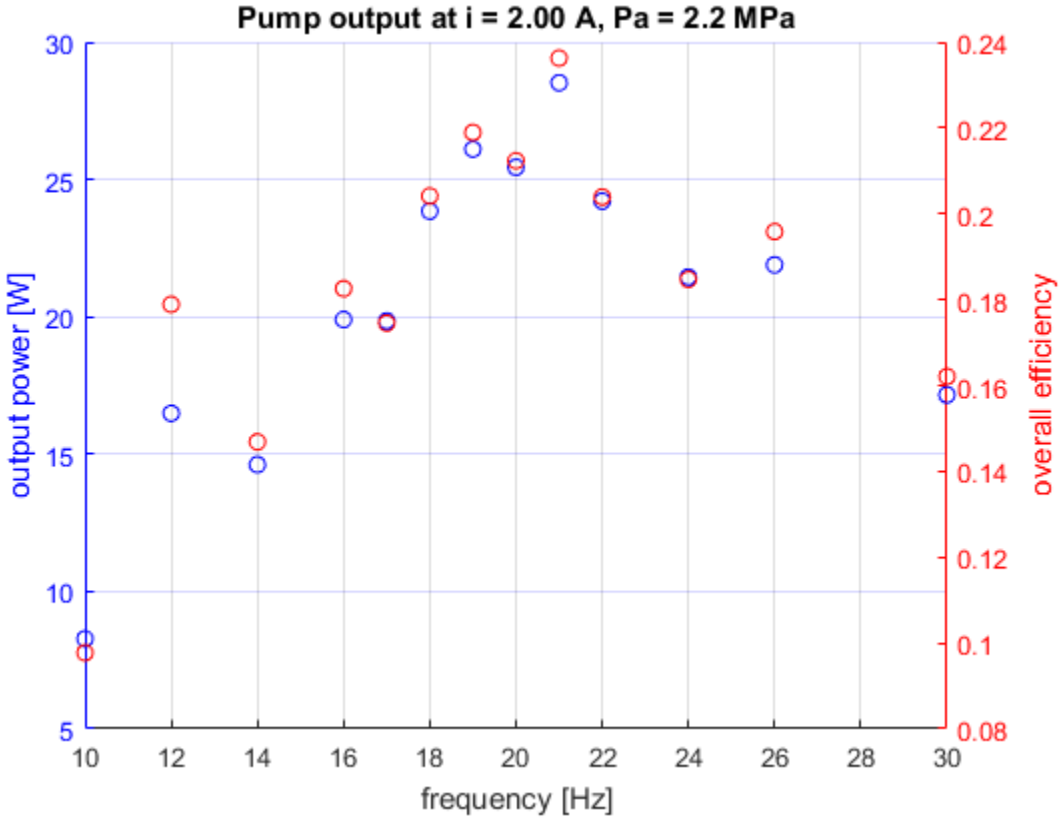

Figure 58: Power output and overall efficiency vs frequency, 2.00 A driving current

By decreasing the motor current to 1.75 A and maintaining the same load, the output power of the pump is reduced to about 20 W peak, and overall efficiency is approximately unchanged. As when excited at 2.00 A, the power output at 1.75 A reaches its maximum at 21 Hz. This maximum power output seems to extend across a wider range of frequencies at the lower input current.

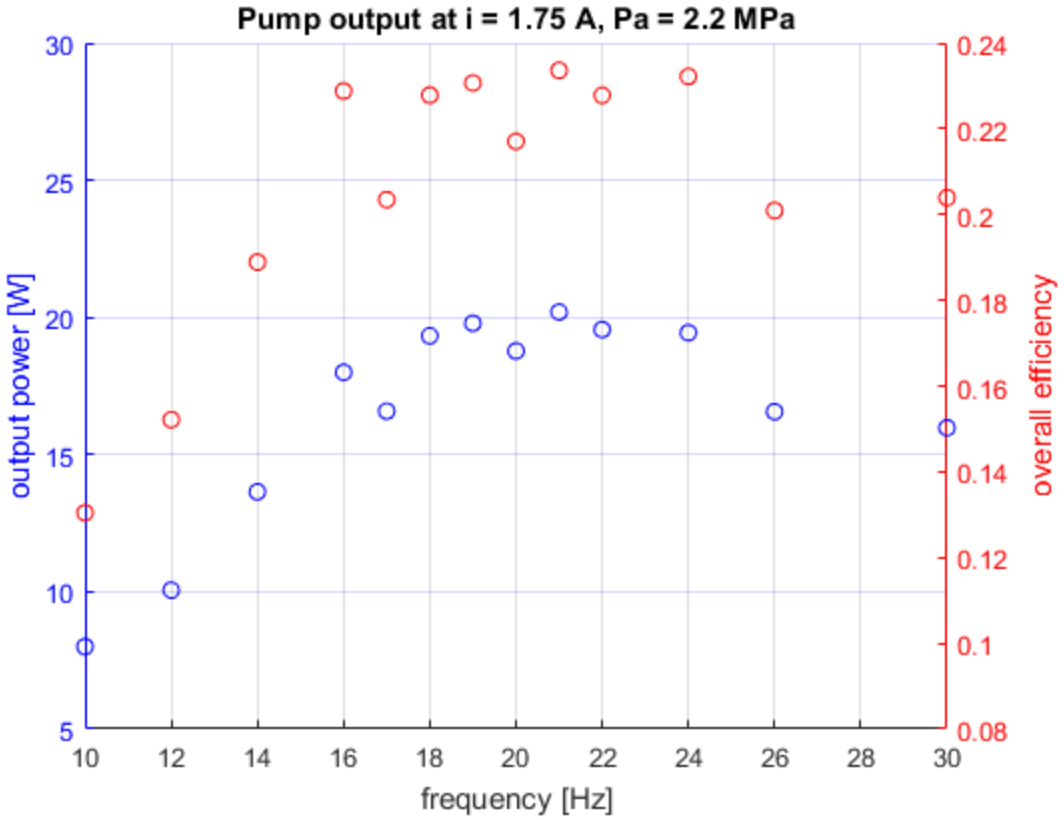

Figure 59: Power output and overall efficiency vs frequency, 1.75 A driving current

The theoretical undamped resonant frequency is 17 Hz. This was found experimentally to be the frequency giving maximum piston displacement, but it did not correspond with the maximum volumetric efficiency, as shown in Figure 60. This difference might be related to the load inertance. With pressure waves traveling between the two delivery check valves, certain piston frequencies may result in better check valve timing and lower backflow.

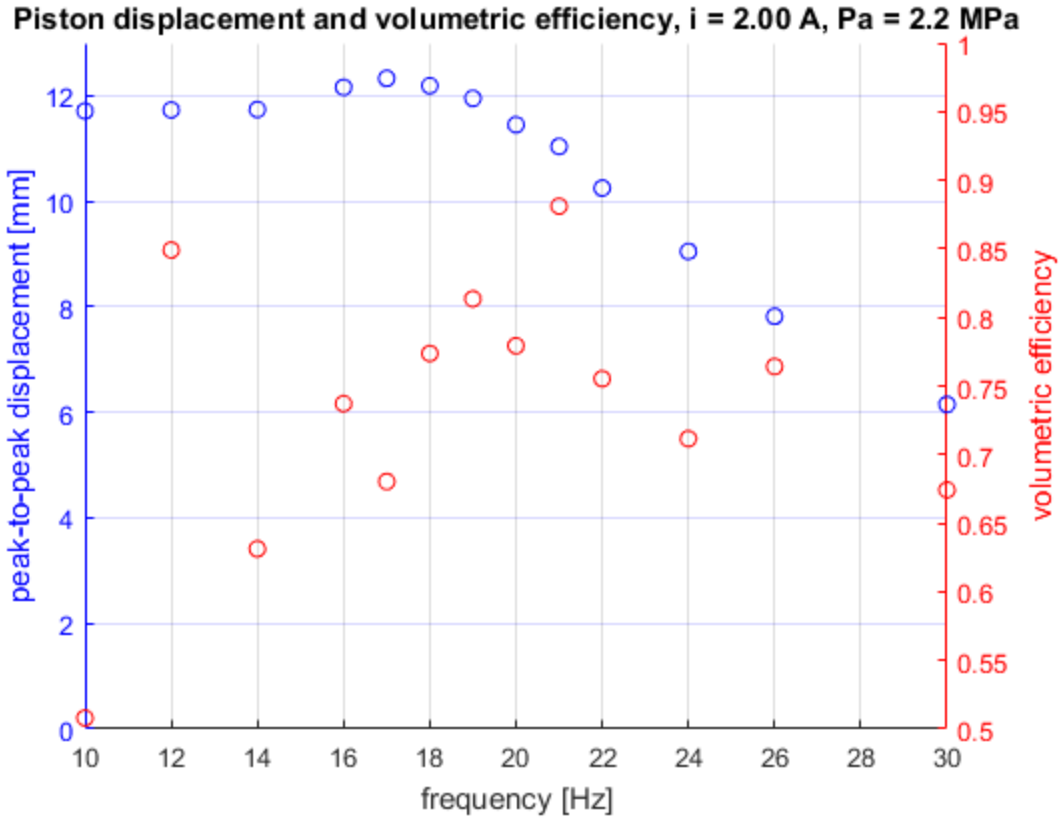

Figure 60: Piston displacement and volumetric efficiency as functions of square-wave driving frequency

There is a similar trend in piston displacement and volumetric efficiency for the lower current input. The actual piston displacements are lower, as expected, but the peak displacement still occurs at 17 Hz. Although the peak volumetric efficiency occurs at 16 Hz instead of 21 Hz, the overall trend is for higher efficiency around the frequency of peak power output.

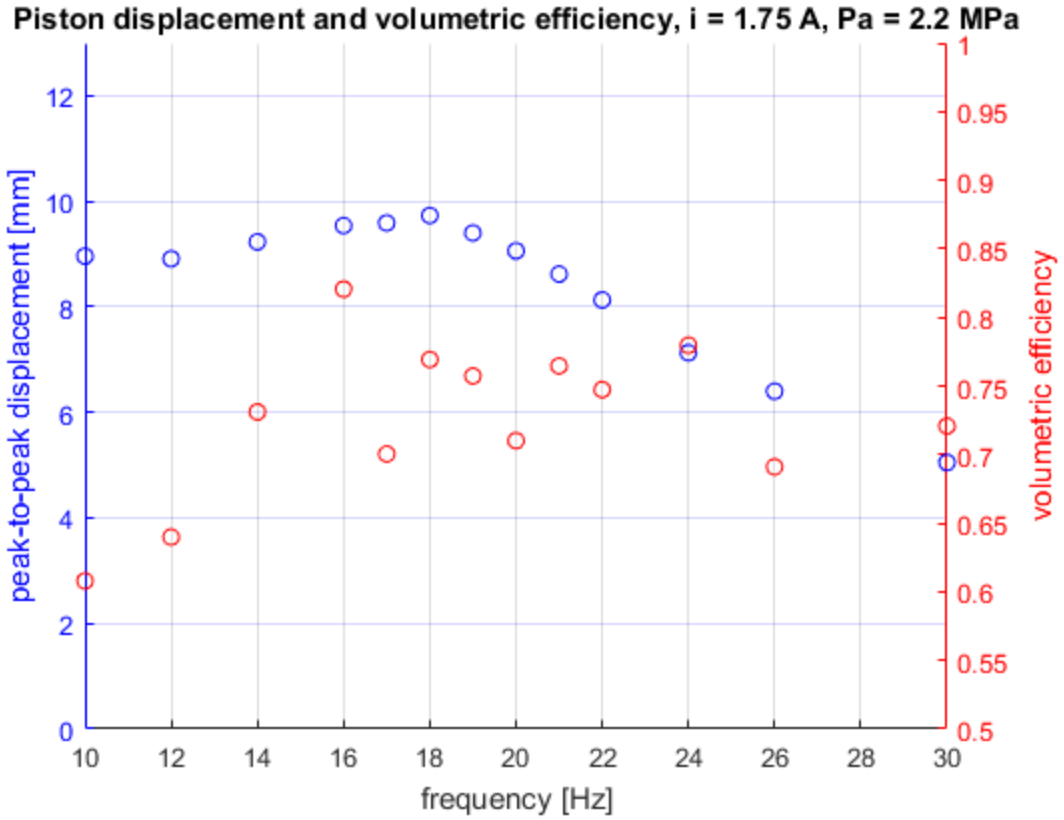

Figure 61: Piston displacement and volumetric efficiency versus frequency, 1.75 A driving current

4.3.3 Detailed Results at Peak Power

For a closer look at the pressure and mechanical dynamics present in the system, the results for the peak output case of 21 Hz will be studied. The mean accumulator pressure for this case was 2.28 MPa. The piston traveled 11.04 mm peak to peak, seen in Figure 62, with a mean flow rate of 0.752 lpm and net volumetric efficiency of 87.8%.

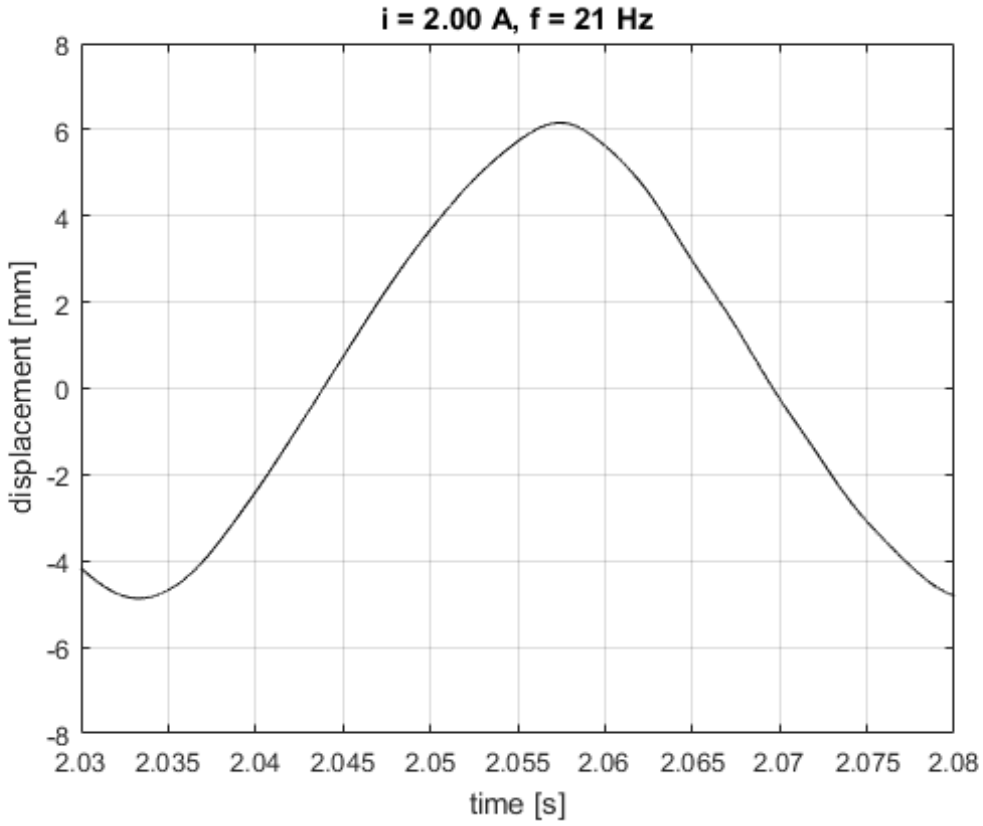

Figure 62: Piston displacement vs time

The pressure-volume in one cylinder through a cycle is shown in Figure 63. First, the inlet check valve opens (1) and the piston draws oil into the cylinder while the cylinder volume increases at low pressure. When the piston changes direction, the inlet check valve closes (2) and the cylinder begins to build pressure as volume decreases. Once the cylinder pressure reaches the cracking pressure of the delivery valve, the outlet opens (3) and flow exits the cylinder as volume continues to decrease at load pressure. When the piston reverses, the cylinder volume begins to expand again and the delivery check valve closes (4). The cylinder pressure falls until the inlet check valve can open to tank (1).

From Figure 60, the check valves are opening and closing cleanly, with minimal change in volume as the pressure rises and falls to the cracking pressures. This also suggests a reasonable value for entrained air fraction in the oil. Based on the PV-diagram,

the impacts of compressibility and check valve performance on volumetric efficiency can be isolated. The total volumetric loss is approximately 0.105 lpm, based on the experimental flow rate and the total volumetric efficiency. The fluid is compressing for the first 0.02 cc of each piston stroke before the delivery check valve opens. This accounts for 0.050 lpm of piston displacement, which is roughly half of the total volumetric losses. Therefore, approximately half of the volumetric losses may be attributed to compressibility of the oil and the other half to back flow and leakage.

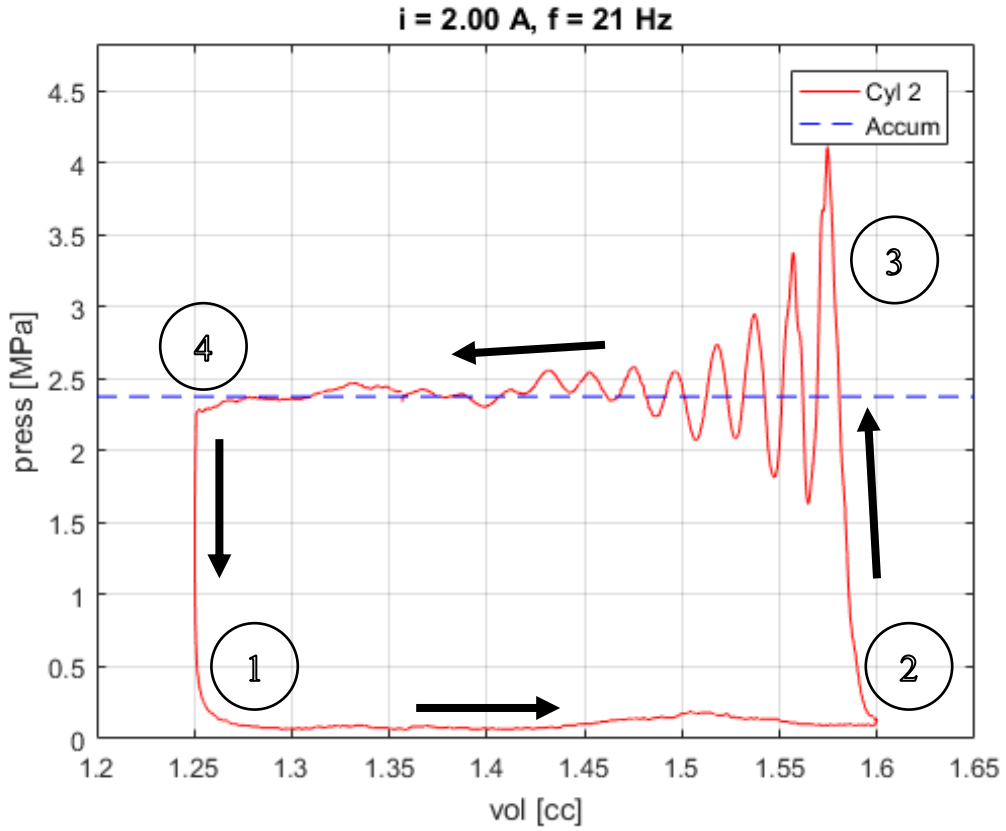

Figure 63: Pressure-vs-volume, i = 2.00 A, f = 21 Hz

Pressure versus time for this case is shown in Figure 64. This plot looks at the pressure in cylinder 2, the pressure immediately following the outlet of cylinder 2, and the pressure at the accumulator. The disturbance in the load and accumulator pressure traces at 2.065 seconds is a pressure wave from cylinder 1. Additionally, it should be noted that once the ringing in the cylinder pressure has damped out, around 2.05 seconds,

the pressure drop across the valve is consistently approximately 0.3 bar (4 psi), which agrees with the Hawe datasheet.

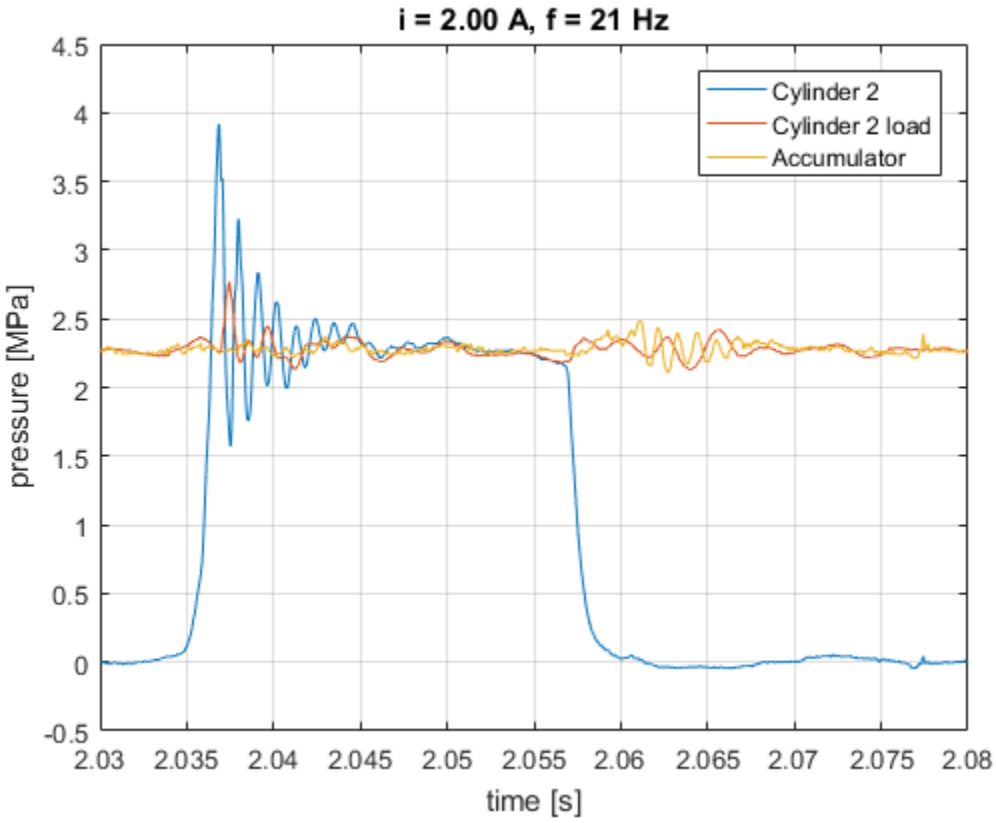

Figure 64: Pressure vs time for square-wave current input

The high amplitude pressure ringing at 2.04 seconds is examined closer in Figure 65, and a numerical derivative of the pressure signal with respect to time in Figure 66. When the check valve begins to transition from closed to open, there should be an inflection in the pressure trace as the rate of pressure rise begins to decelerate. As seen in the gradient plot, the first inflection occurs at 2.0364 seconds. At this time, the pressure difference across the delivery check valve is very low, as it should be. However, the valve doesn't stay open, as the pressure gradient stays positive through another two inflection points, despite a favorable pressure drop across the valve. It is not until 2.0366 seconds that the valve opens and stays open, as the pressure gradient goes negative and the cylinder pressure has reached its maximum value. At this point, the cracking pressure

is close to 9 bar (130 psi). Even with a finite lag time between the true check valve outlet and the pressure transducer, this is still over two orders of magnitude greater than expected. As discussed later, this discrepancy is believed to be “stiction” between the valve seat and disc, delaying the valve opening.

Looking to a pressure inflection further ahead at approximately 2.0442 sec, there is an experimental cracking pressure of approximately 6 psi. Accounting for possible error in calibration, transducer-DAQ resolution, and the finite lag time, this cracking pressure is more reasonable.

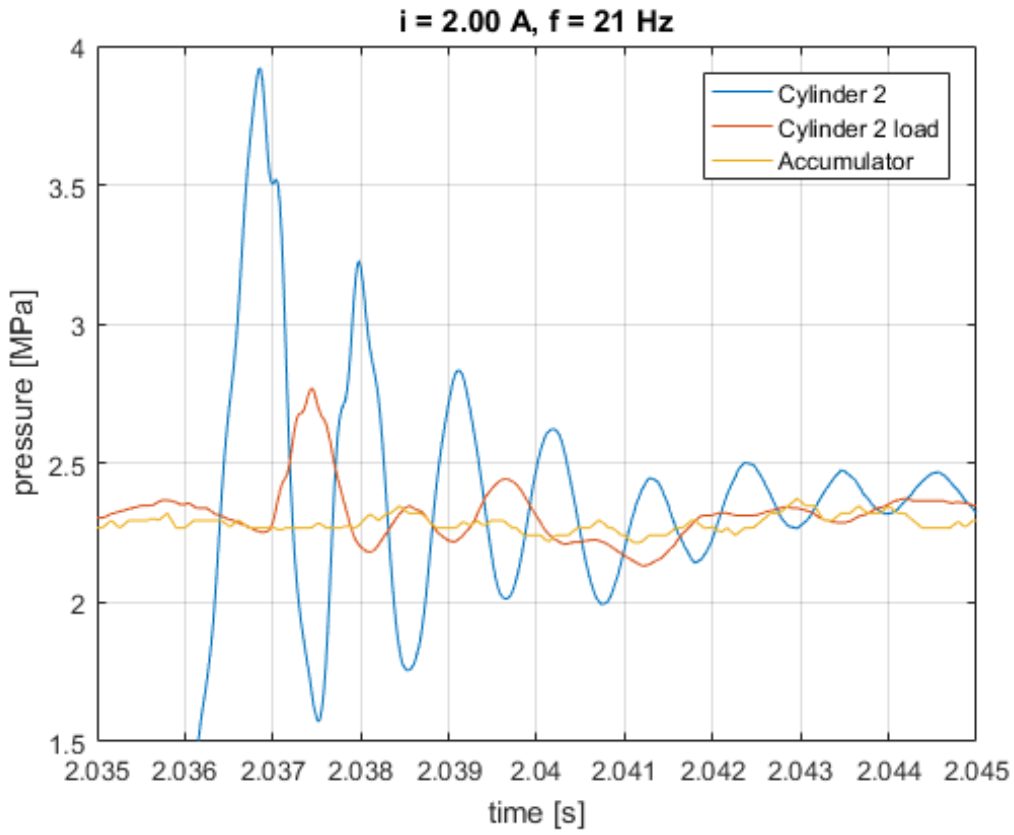

Figure 65: Detailed view of pressure-vs-time for square-wave current input

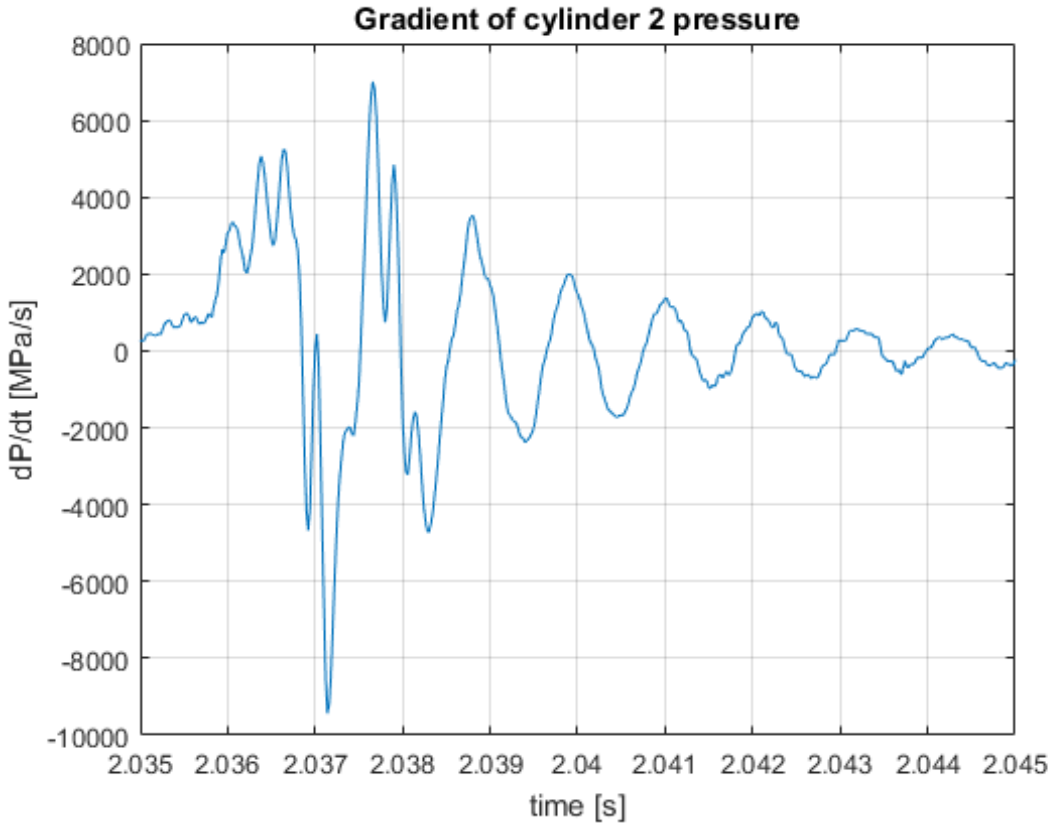

Figure 66: Gradient of pressure-vs-time for square-wave current input.

The initial high pressure transient created by the valve stiction sets off a ringing of the cylinder and load pressures. This ringing can be examined closer using a Fast Fourier Transform (FFT) to identify significant natural frequencies, as in Figure 67. The FFT is dominated by component frequencies that make up the decomposed 17 Hz square wave signal. There are two other significant peaks to note. The first is at approximately 882 Hz and is related to the inertance of the delivery lines. The second is at 3.1 kHz, and may be related to dynamics of the check valve itself.

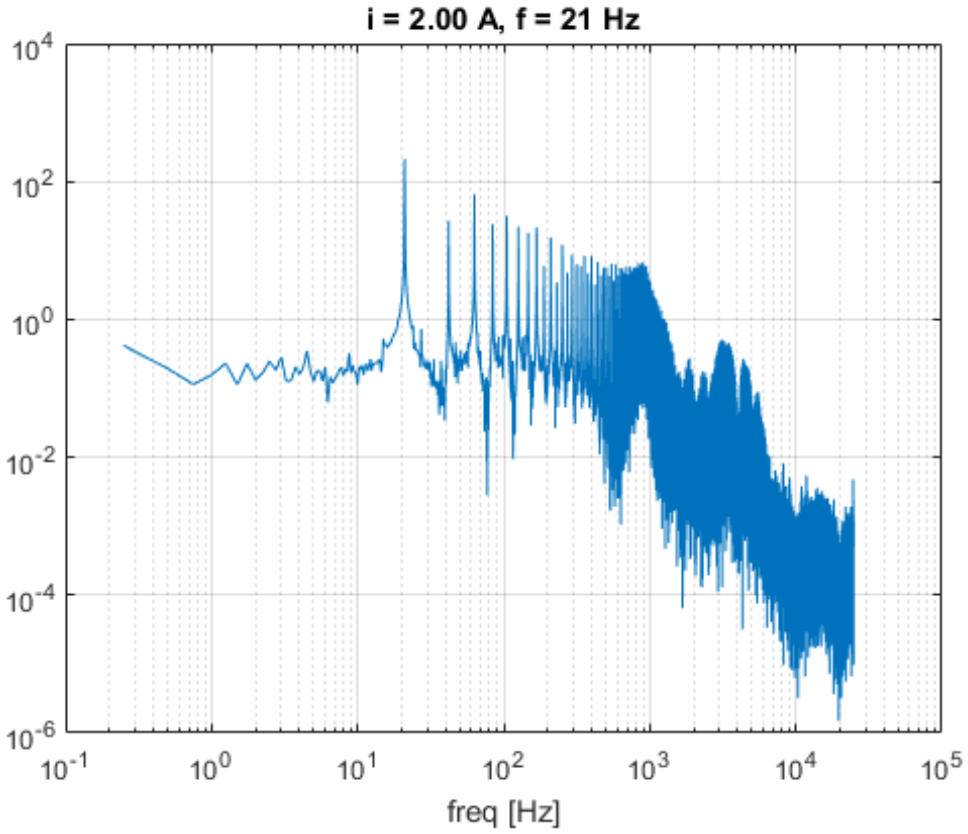

Figure 67: FFT of pressure-vs-time for square-wave current input

4.3.4 Comparison with Modeled Performance

When the numerical model is used with the parameters discussed in 4.2.4.4 and untuned for the increased friction in the experimental design, the model does not track the experimental piston displacement well, as seen in Figure 68.

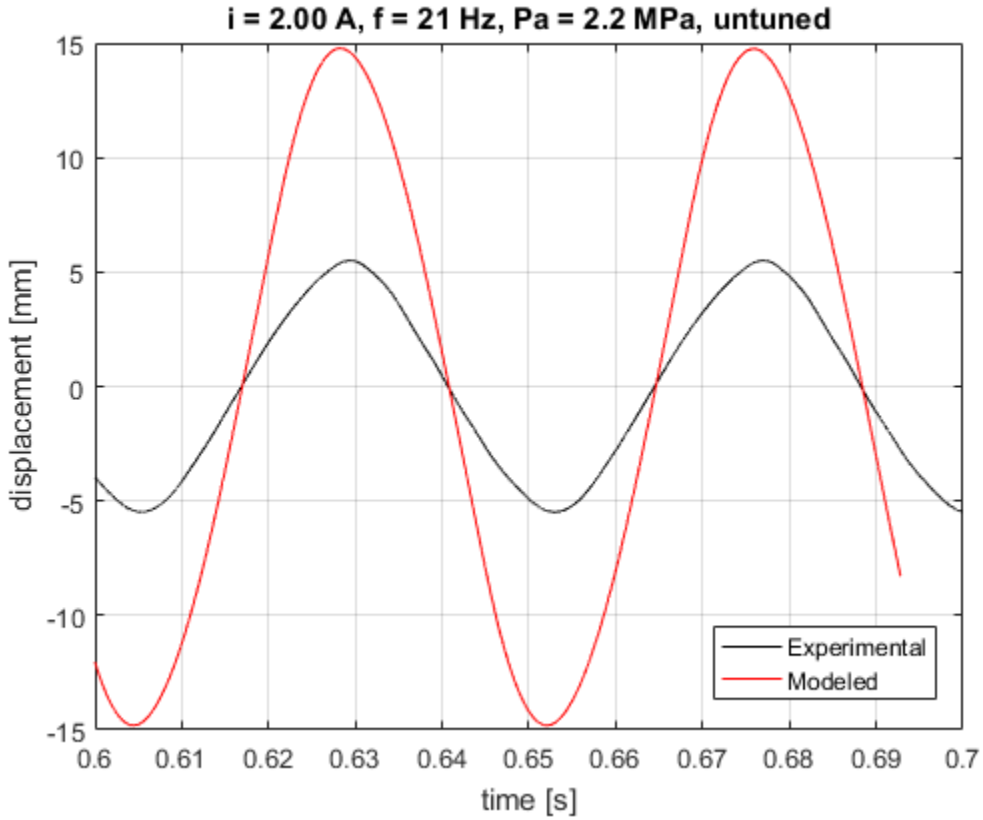

Figure 68: Comparison of experimental and modeled piston displacement, untuned

By increasing the mechanical friction by a factor of 13, the piston motion tracks the experimental results very well.

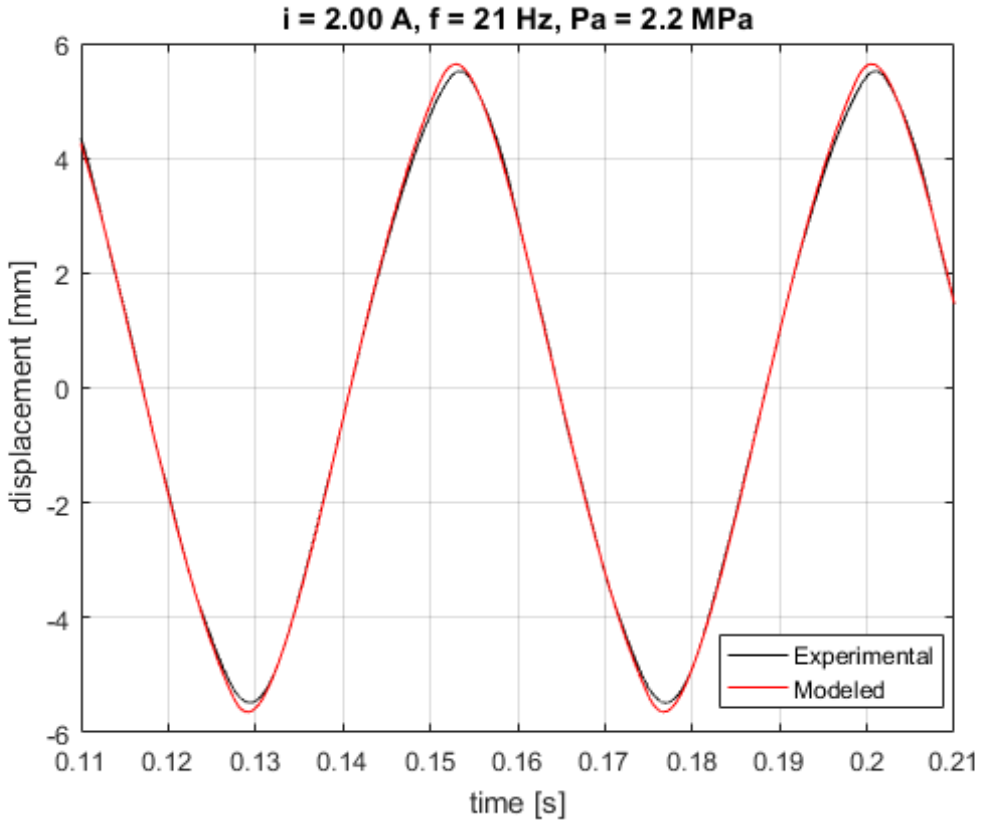

Figure 69: Comparison of experimental and modeled piston motion

The pressure-versus-volume plot in Figure 70 tracks the rise and fall of pressure quite well, with an entrained air fraction of 2%. The performance at delivery pressure does not track as well; this is elaborated on below.

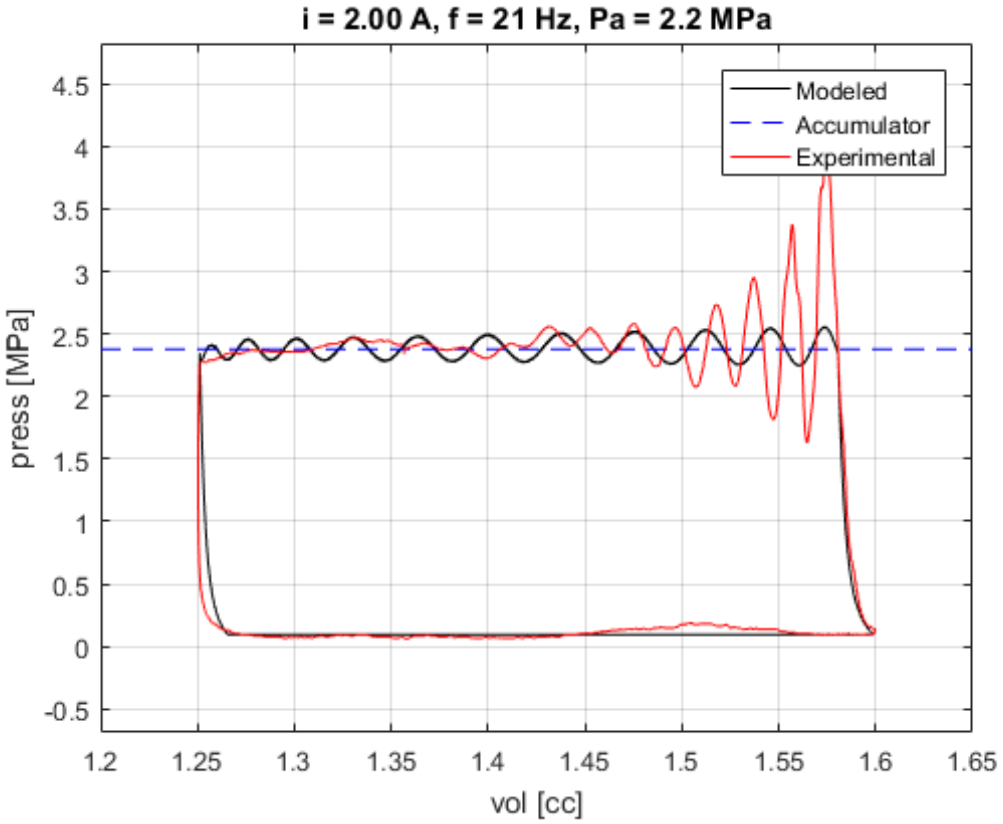

Figure 70: PV diagram comparing model and experimental results

In Figure 71 is a comparison of the model output and experimental results for the cylinder pressure as a function of time. Again, the model tracks the rise and fall of the pressure within the cylinders very well, but the behavior at delivery pressure is not as well matched. In particular, the model captures none of the very high pressure transients at the beginning of the delivery stroke. Also, the natural frequency of the pressure ringing is off by a factor of about 2.

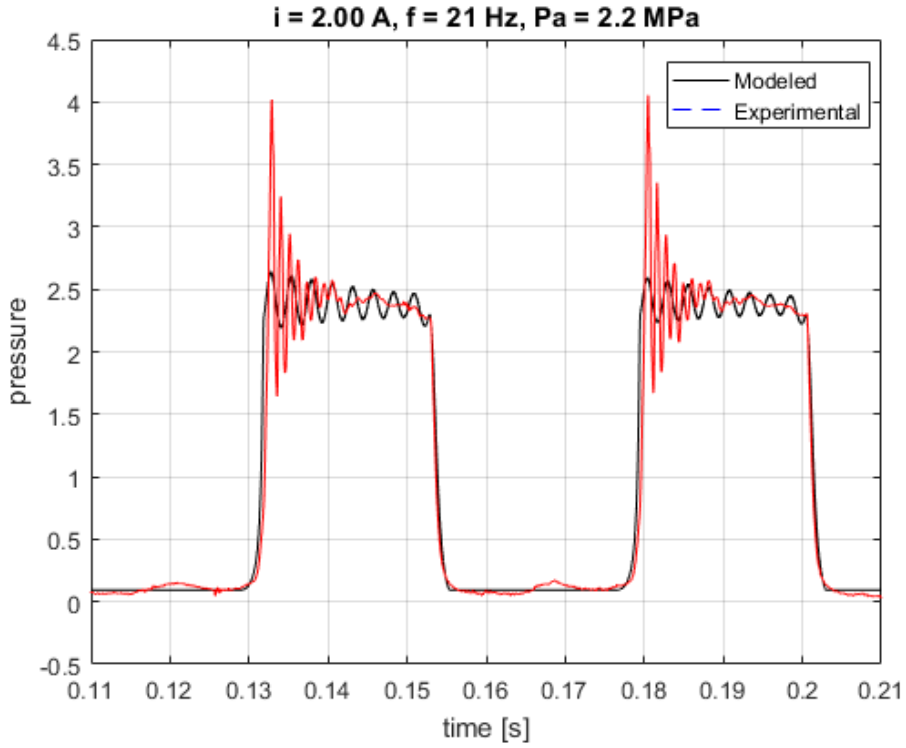

Figure 71: Comparison of modeled and experimental cylinder pressure

The dominant natural frequency of the ringing in the pressure trace is likely due to the inertance in the delivery lines. As described in Chapter 3, the inertance lines are modeled using the physical dimensions of the lines used up to the tee in the experimental setup. Arbitrarily halving the inertance in the model solution increases the natural frequency and brings it closer in line to that seen experimentally, as seen in Figure 72.

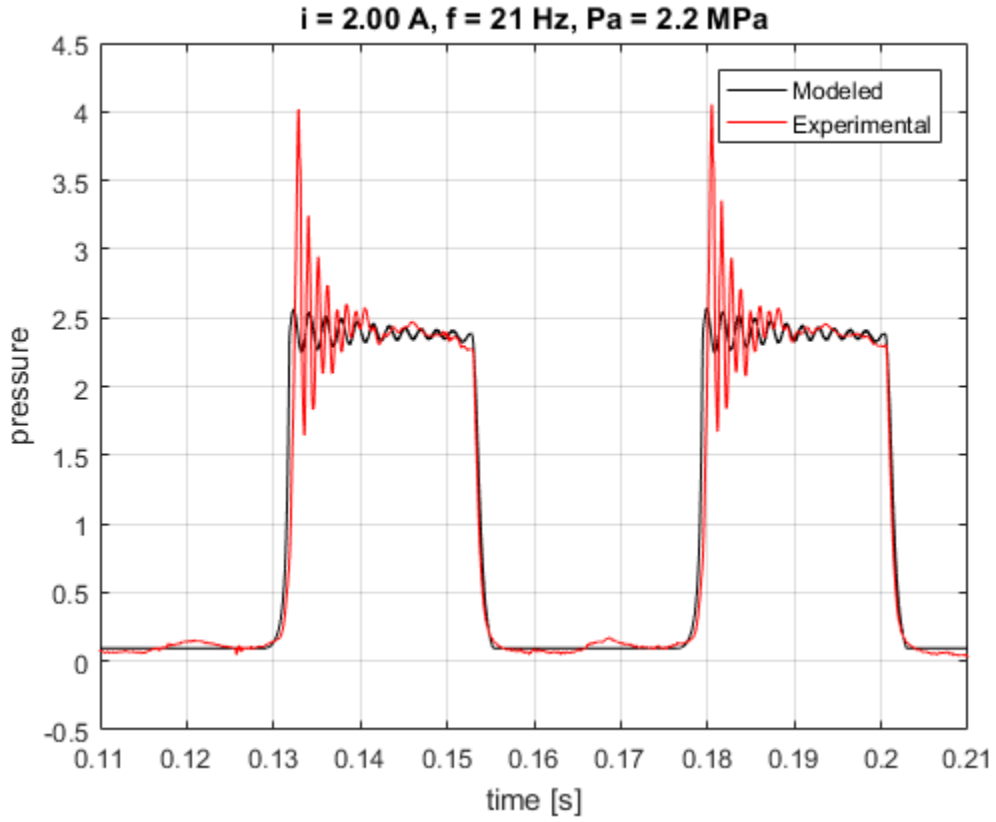

Figure 72: Pressure vs time comparison, with half the delivery inertance

4.4 Discussion

4.4.1 Varied loading and frequency

At zero load, the pump behaves mostly as expected. The peak piston displacements occur at 16 Hz instead of the theoretical undamped resonance of 17 Hz. The volumetric efficiency is very high with very little dependence on driving frequency.

While holding the accumulator pressure constant at 2.2 MPa (330 psi), the output power reaches a maximum of nearly 30 W and 23% overall efficiency at 21 Hz for 2.00 A excitation and 20 W and 23% overall efficiency at 21 Hz for 1.75 A. The piston peak-to-peak displacement peaks in each case at the expected value of 17 Hz, with volumetric efficiencies reaching their maxima closer to 21 Hz. The frequency of peak power production does not correspond to the resonant frequency of the piston. The maximum

volumetric and overall efficiencies, as well as the maximum output power, all occurred at 21 Hz. Interestingly, this does not coincide with resonance of the mechanical system, which occurred at 17 Hz. In fact, this point was a local minimum for measured volumetric efficiency. This suggests that there are additional dynamics in the load, such as capacitance and inertance in the oil downstream of the check valves, that are interacting with one another to change the volumetric efficiency and therefore the power output. With very large transient pressures, likely due to stiction in the check valve, the inertance of the delivery lines played a significant role in the volumetric efficiency and therefore the output flow rate of the pump. This was in part a challenge brought on by separating the delivery check valves by around 0.3 m of fluid conduit.

As presented above, the large initial cracking pressures played a significant role in the transient performance of the pump. One possible cause of the large initial cracking pressure is stiction in the valve seat. The Hawe RC check valves use a flat plate that is flush with a flat valve seat. As the plate lifts off the seat, the fluid film between the surfaces generates a force that opposes the motion, resulting in significantly greater than cracking pressure than predicted by just the spring force. This increases the pressure required to quickly open the valve. At the extreme limit, rapidly opening the valve could cavitate the fluid film in annular area between the disc and the valve seat; this would require an additional 8-27 N to open, depending on the exact geometry of the valve. With a downstream pressure of 2.2 MPa, this would require an upstream pressure as high as 3.0 – 4.6 MPa to overcome cavitation. These pressures are comparable to the maximum transient pressures observed in the cylinders.

4.4.2 Comparison with Modeled Performance

With a significant adjustment to the mechanical drag in the system to account for unmodeled friction such as that in the linear motor bearings and the piston clearance seal, the numerical model predicts the mechanical dynamics of the piston oscillation very well. The pressure dynamics as the check valves open and close are also predicted well, which demonstrates that the Cho model for variable bulk modulus with an entrained air fraction of 2% is a good assumption in this case [41].

The model does not account for valve stiction or other check valve dynamics, so it is unable to capture the large pressure transients that are seen in the experimental results. The modeled inertance at the load, however, does demonstrate that the experimental pressure ringing in the cylinders is related to an inertance in the delivery lines. In particular, by halving the inertance, we see an increase in the natural frequency of approximately 38%. The inertance was modeled based on the length of the delivery line to the tee, at which point the accumulator pressure is assumed constant. A more accurate model design would use a switched volume at the accumulator and allow pressure waves to traverse through the tee towards the opposite cylinder, as observed in the experimental results. This begins to leave the scope of this thesis, however, which is the linear piston pump itself.

4.5 Conclusion

To conclude, the experimental design proved the concept of using a linear motor to drive a free piston. The linear servo motor was operating at the limits of its rated continuous current and could achieve a resonant condition using the opposing springs. At this operating point, the power output was as high as 28 W with approximate overall efficiencies of 23%. Pressure delivery was upwards of 24 bar (350 psi) with flow rates as high as 0.75 lpm. Losses were mostly dominated by ohmic heating in the linear motor coils, but volumetric losses and mechanical friction in the linear motor bearings and in wear surfaces between the piston and cylinder assemblies also played a role.

The pump also seemed to be impacted by poorly performing check valves at the initial transition from closed to open. This is believed to be due to stiction between the moving element of the valve and the valve seat. Future iterations of the experimental design will use a custom tubular linear motor with significantly lower moving mass and friction. Incorporating the piston into the design of the motor shaft will help reduce mechanical friction of the piston and cylinder assembly. In addition, different types of springs and flexures may be investigated to reduce radial loading on the piston.

With respect to comparisons with the coupled model presented in this thesis, the experimental work improved understanding of the dynamics of the free piston and the

complications of separating the delivery check valves by a considerable distance. Future work could incorporate the check valve model developed and experimentally validated by Knutson et al. to capture the stiction in the valve seat and other valve dynamics [48].

5 Conclusion

Mobile hydraulics at the human scale are experiencing a rapid rate of technological advancement. Improvements to hydraulic actuators have enabled high power and precision control in applications ranging from robotics to powered medical devices. The advantage of fluid power lies in its high actuation power density, making it attractive to many mobile applications.

Despite these advancements, many hydraulic actuation systems still rely on a modularized concept for hydraulic power generation. The usual conversion from electric to hydraulic energy uses an electric motor to generate shaft power. The shaft power is the input to a pump, which converts the rotating inertia of the shaft into piston oscillation and hydraulic flow. Rotating electric machinery generally operates most efficiently at high speeds, requiring either a gearbox or lower efficiency operating point. This conventional power supply design is modular, which allows for flexibility in how it is designed and implemented. However, the excessive energy conversions tend to decrease efficiency and power density in human scale mobile hydraulics.

5.1 Review

This thesis presented the design, optimization, and initial prototyping of a linear electromagnetic piston pump. The linear piston pump reduces the number of energy conversions by driving a piston directly with a linear electric motor. The electric motor and hydraulic pump are integrated into a single unit, making for a more compact and power dense design. With fewer energy conversions, it has the potential to have a higher overall conversion efficiency.

A coupled numerical model was developed to predict performance and aid in preliminary design studies. It used a quasi-static electromagnetics model to predict linear motor performance and a dynamic mechanical model to predict piston motion and pressure dynamics within the cylinders. The linear motor model was a magnetic equivalent circuit (MEC), which discretizes the linear motor into a network of reluctance branches and magnetomotive forces. Solution of the MEC provided the flow of magnetic

energy, or flux, through each branch. This information allowed calculation of the static performance of the actuator, including excitation force and inductance as functions of displacement. The flux also permitted an estimation of mean cyclic magnetic losses in the steel, which typically requires a transient solution in finite element analysis (FEA). An experimental prototype validated the MEC and FEA force models for two different excitation currents and the full range of travel.

The electromagnetics model was used to supply an excitation force to the mechanical dynamics model for the piston, as described in Chapter 3. This model accounted for electromagnetic force, viscous drag in the cylinder-piston clearance seal, spring forces, and pressure forces. The solution was executed to cyclic steady state, and the power density and efficiency were calculated.

A design optimization used a genetic algorithm on the coupled model to explore the design space and determine maximum expected gains in power density and efficiency compared to the state of the art. The NSGA-II was selected due to the possibility of multiple local minima in the solution space and for its ability to handle multiple objectives simultaneously.

To validate the mechanical and pumping dynamics model, in Chapter 4 an experimental design was built using an off-the-shelf linear servo motor and check valves, and a custom manifold. This prototype was able to produce nearly 30 W at 2.4 MPa (350 psi) with an overall efficiency of approximately 28%. The losses were due to volumetric inefficiencies of 25-40%, ohmic losses of around 45%, and mechanical friction in the motor bearings and the piston seal. With an adjustment to the mechanical drag in the system to account for unmodeled friction in the bearings and other contacting surfaces, the model tracks the experimental piston trajectory very well. The addition of the inertance term suggests that the pressure ringing in the cylinders is related to the long delivery lines, but further work is required to accurately model these dynamics.

5.2 Conclusions

Overall, this work provides a promising start to a linear electromagnetic piston pump. The coupled numerical model has been validated for quasi-static operation.

The model successfully used lumped parameter modeling from the electromagnetic and the mechanical domains, demonstrating that the MEC is a good approach for computationally efficient and accurate modeling of electrohydraulic components.

MEC force modeling was very accurate for baseline cases and reasonably accurate for the optimized geometries. Inaccuracies arose at medium to large piston displacements in the optimized cases, but the model stayed within 10% at zero displacement. This is important because the linear motor force is most significant relative to the other forces acting on the piston at zero displacement. When the piston reaches the medium displacements at which the model begins to lose accuracy, the other forces acting on the piston have a significantly higher impact on the mechanical dynamics. For instance, at just 5 mm of displacement in the optimized linear motor, the spring forces are over three times as great as the FEA-evaluated linear motor force. This suggests that the use of an MEC is valid for a design optimization.

The experimental prototype of the linear motor further validated use of the MEC and FEA force models. The MEC and FEA captured the shape of the force-vs-displacement curve for static excitation very well. They also underpredicted the maximum experimental force, suggesting that the dynamic pump model might be conservative in its prediction of power output.

The coupled pump model demonstrated that the use of an MEC force calculation is an adequate substitute for FEA and solves in a fraction of the time. While there was some error in the force evaluation, particularly at larger displacements of the optimized design, this error did not necessarily translate into reduced power output. As mentioned above, this is likely because the linear motor force only dominates mechanical dynamics, and therefore power output, at low displacements. Other forces begin to dominate at larger displacements, where the MEC has increased error. Inertance in the long delivery lines has an impact on pressure dynamics. To a certain extent, this is unavoidable because the manifolds are located far apart and must be combined to a common output.

The optimization demonstrated that an improvement of up to 400% in power density over state-of-the-art compact hydraulic power supplies is attainable. There is a

minimal tradeoff between power density and efficiency for the bulk of the Pareto-optimal front, suggesting that large gains in power density are attainable with a minimal decrease in efficiency. The high efficiency designs tended to have larger diameter pistons with lower velocities and peak-to-peak displacements, while the high power density designs used smaller pistons to develop larger velocities and displacements. This is reasonable considering that viscous drag was generally the highest power loss mechanism and was proportional to the square of velocity.

The experimental prototype with an off-the-shelf linear servo motor validated the mechanical dynamics model after a significant increase to the friction term. The tuning was necessary to account for the increased drag in the physical system, which was a result of losses in the linear ball bearings and misalignment in the piston-cylinder interface. With the friction tuned, the mechanical dynamics were predicted very well by the model. Future prototypes should be designed with better alignment between the piston and cylinder.

Additionally, the prototype was inhibited by poor check valve performance and inertance in the delivery lines. The delivery check valves were experiencing stiction at the valve opening events, resulting in very high transient pressures. The inertance in the delivery lines allowed these pressure spikes to propagate through the delivery lines. There was also a resulting ringing of the cylinder pressure. There might have been interference between these pressure waves that resulted in the volumetric efficiency varying as a function of frequency. Future work should consider check valves with reduced stiction and lower inertance delivery lines.

Overall, this thesis suggests that the linear electromagnetic piston pump concept is worth continued study. Pump modeling was validated for the quasi-static linear motor assumption, and the validated model was optimized to suggest significant improvements in performance metrics over the state of the art. The experimental prototype operated at fairly low output power and efficiency, but these effects were well captured by the adjustment of the modeled friction. A better mechanical design with lower friction and a lower moving mass would allow operation at higher resonant frequencies and therefore

higher power output. In general, the power output scaled with frequency. Losses also scale with frequency, and tended to be underpredicted in this thesis. Check valve dynamics also become significant at high frequencies. It is likely that linear pumps would therefore be better off operating larger diameter pistons at lower frequencies and lower power levels.

Most of the losses in the optimized linear electromagnetic piston pump, not including throttling across the check valve, were due to viscous drag and DC resistance in the windings. Around 35 W of resistive losses in the windings are likely unavoidable; decreasing resistance by increasing wire diameter will increase the current required for the same force output, and resistive losses scale with current squared. The viscous drag could be optimized further; the clearance seals modeled in this thesis were up to 6 μm, and the theoretical power loss through leakage is orders of magnitude less than viscous drag. Therefore, future designs could experiment with an increased clearance seal to decrease friction. However, a certain amount of mechanical friction in a physical system operating at a resonant frequency is probably unavoidable. As result, peak efficiencies likely would not exceed the 85% figures reported in the optimized designs. This is still a vast improvement over conventional rotary setups, particularly when the rotating electric machinery is operating at an off-peak angular speed.

5.3 Recommendations for Future Work

There are two aspects of future work that would be beneficial for study. The first is a fully coupled transient coupled finite element model. This would use a transient electromagnetics FEA excited in either current- or voltage-control mode and an external lumped parameter pressure dynamics model. The pressure dynamics could feed into the transient FEA as an external force acting on the piston in addition to the spring and viscous damping forces. This approach would help validate the quasi-static assumption that was necessary for using the MEC. This would also allow for a much more detailed calculation of magnetic losses and their effect on the mechanical dynamics.

A second aspect of future work is fabrication of a larger scale linear piston pump using an optimized geometry to experimentally validate the coupled model presented in

this thesis. The motor built for this thesis was a lower force design, with compromises for ease of manufacturing such as a 2 mm air gap, two stator poles, low-carbon steel stator sections, and no built-in return springs or piston heads. Constructing a larger scale, higher force linear motor with the springs built into the motor body would be a strong validation prototype for the linear piston pump coupled model as a whole. Fabricating additional prototypes would enable testing increased overall output and methods for achieving efficient variable displacement with all pumps still operating at resonance.

To conclude, this thesis successfully demonstrated that improvements are attainable in human scale mobile hydraulic power supply by increasing compactness and decreasing the number of energy conversions. The numerical models were validated through two separate experiments to confirm static electromagnetic and dynamic mechanical performance. Although more work must be done to fully demonstrate that the models accurately predict pump performance, and that the pump is capable of operating at a human-scale of power, this thesis provides a strong foundation for future work in this area.

6 References

[1] E. Guizzo and E. Ackerman, "Boston Dynamics' Marc Raibert on Next-Gen ATLAS: "A Huge Amount of Work"," 24 February 2016. [Online]. Available: http://spectrum.ieee.org/automaton/robotics/humanoids/boston-dynamics-marc-raibert-on-nextgen-atlas. [Accessed 24 April 2017].

[2] E. Ackerman, "ATLAS DRC Robot Is 75 Percent New, Completely Unplugged," 20 January 2015. [Online]. Available: http://spectrum.ieee.org/automaton/robotics/military-robots/atlas-drc-robot-is-75-percent-new-completely-unplugged. [Accessed 24 April 2017].

[3] B. C. Neubauer, J. Nath and W. K. Durfee, "Design of a Portable Hydraulic Ankle-Foot Orthosis," in *IEEE Engineering in Medicine and Biology Society*, 2014, 2014.

[4] T. Yu, P. Plummer, P. Iravani, J. Bhatti, S. Z. OBE and D. Moser, "The Design, Analysis and Testing of a Compact Electrohydrostatic Powered Ankle Prosthesis," in *Fluid Power Motion and Control*, Bath, 2016.

[5] F. Sup, A. Bohara and M. Goldfarb, "Design and Control of a Powered Transfemoral Prosthesis," *International Journal of Robotics Research,* vol. 27, no. 2, pp. 263-273, 2008.

[6] J. D. Smith and P. E. Martin, "Effects of Prosthetic Mass Distribution on Metabolic Costs and Walking Symmetry," *Journal of Applied Biomechanics,* vol. 29, pp. 317-328, 2013.

[7] K. A. Shorter, G. K. Kogler, E. Loth, W. K. Durfee and E. T. Hsiao-Wecksler, "A Portable Powered Ankle-Foot Orthosis for Rehabilitation," *Journal of Rehabilitation Research & Development,* vol. 48, no. 4, pp. 459-472, 2011.

[8] J. Xia and W. K. Durfee, "Analysis of Small-Scale Hydraulic Actuation Systems," *Mechanical Design,* vol. 135, pp. 091001-1-11, 2013.

[9] Concentric AB, "He Power Packs," July 2011. [Online]. Available: http://www.concentrichydraulics.com/_downloads/Catalogs/HEPOWERPACKS_C.pdf. [Accessed 17 April 2017].

[10] J.-P. Henderson, A. Plummer, D. N. Johnson and C. Bowen, "The Influence of Passive Valve Characteristics on the Performance of a Piezo Pump," in *Symposium on Fluid Power & Motion Control*, Sarasota, 2013.

[11] A. Chaudhuri and N. Wereley, "Compact hybrid electrohydraulic actuators using smart materials: a review," *Intelligent Material Systems and Structures,* vol. 23, no. 6, pp. 597-634, 2011.

[12] D. G. Lee, S. W. Or and G. P. Carman, "Design of a Piezoelectric-hydraulic Pump with Active Valves," *Journal of Intelligent Material Systems and Structures,* vol. 15, pp. 107-115, 2004.

[13] H. Tan, W. Hurst and D. Leo, "Performance modeling of a piezohydraulic actuation system with active valves," *Smart Material Structures*, vol. 14, pp. 91-110, 2005.

[14] C. Cadou and B. Zhang, "Performance Modeling of a Piezo-hydraulic Actuator," *Intelligent Material Systems and Structures*, vol. 14, pp. 149-160, 2003.

[15] R. Radebaugh, "Development of the Pulse Tube Refrigerator as an Efficient and Reliable Cryocooler," in *Institute of Refrigeration*, London, 1999-2000.

[16] R. Karunanithi, S. Jacob, A. S. Gour, C. Damu and M. Das, "Development of a Moving Magnet Type Linear Motor for Dual Piston Compressor for Pulse Tube Cryocooler," in *American Institute of Physics: Advances in Cryogenic Engineering*, Spokane, 2012.

[17] I. Ruhlich, M. Mai, C. Rosenhagen, A. Schreiter and C. Mohl, "Development of a Miniature Moving Magnet Cryocooler SX040," in *SPIE - The International Society for Optical Engineering*, San Diego, 2011.

[18] W. W. Wang, L. Y. Wang and Z. H. Gan, "Design of a Valved Moving Magnet Type Linear Compressor for a Joule-Thomson Cryocooler," in *Advances in Cryogenic Engineering*, Anchorage, 2014.

[19] Gast Manufacturing Inc., "Linear Compressors and Vacuum Pumps," 9 February 2012. [Online]. Available: http://gastmfg.com/uploads/catalogs/Linear_Catalog_Final_Rev_Feb09-2012_lores.pdf. [Accessed 26 April 2017].

[20] Thomas by Gardner Denver, "Linear diaphragm and vibrating armature pumps from Thomas," Gardner Denver Medical, 2017. [Online]. Available: https://www.gd-thomas.com/en/technologies/linear. [Accessed 26 April 2017].

[21] Nitto Kohki Co Ltd., "Air Compressors, Vacuum Pumps & Liquid Pumps," [Online]. Available: http://nitto-kohki.meclib.jp/Lk001/book/#target/page_no=3. [Accessed 26 April 2017].

[22] I. Boldea and S. A. Nasar, "Linear Electric Actuators and Generators," *IEEE Trans. Energy Conversion*, pp. 712-717, 1999.

[23] T. Yamada and K. Fujisake, "Basic Characteristic of Electromagnetic Force in Induction Heating," *IEEE Transactions on Magnetics*, vol. 44, no. 11, pp. 4070-4073, 2008.

[24] L. Tong and M. Lin, "Study on a high thrust force bi-double-sided permanent magnet linear synchronous motor," *Advances in Mechanical Engineering*, vol. 8, no. 3, pp. 1-10, 2016.

[25] X. Chen, Z. Q. Zhu and D. Howe, "Modeling and Analysis of a Tubular Oscillating Permanent-Magnet Actuator," *IEEE Transactions on Industry Applications*, vol. 45, no. 6, pp. 1961-1970, 2009.

[26] J. Wang, G. W. Jewell and D. Howe, "A general framework for the analysis and design of tubular linear permanent magnet machines," *IEEE Transactions on Magnetics*, vol. 35, no. 3, pp. 1986-2000, 1999.

[27] Z. Q. Zhu, P. J. Hor, D. Howe and J. Rees-Jones, "Calculation of Cogging Force in a Novel Slotted Linear Tubular Brushless Permanent Magnet Motor," *IEEE Transactions on Magnetics,* vol. 33, no. 5, pp. 4098-4100, 1997.

[28] S.-M. Jang, K.-H. Kim, K.-J. Ko, J.-H. Choi, S.-Y. Sung and Y.-B. Lee, "Improved thrust calculations of active magnetic bearings considering fringing flux," *Journal of Applied Physics,* vol. 111, pp. 07E726 - 1-3, 2012.

[29] A. R. Tariq, C. E. Nino-Baron and E. G. Strangas, "Iron and Magnet Losses and Torque Calculation of Interior Permanent Magnet Synchronous Machines Using Magnetic Equivalent Circuit," *IEEE Transactions on Magnetics,* vol. 46, no. 10, pp. 4073-4080, 2010.

[30] M.-F. Hsieh and Y.-C. Hsu, "A Generalized Magnetic Circuit Modeling Approach for Design of Surface Permanent-Magnet Machines," *IEEE Transactions on Industrial Electronics,* vol. 59, no. 2, pp. 779-792, 2012.

[31] V. Ostovic, Dynamics of Saturated Electric Machines, New York: Springer-Verlag, 1989.

[32] S. D. Sudhoff, *MEC 3.2 for MATLAB,* Lafayette: Purdue University, 2012.

[33] D. C. Hanselman, Brushless Permanent-Magnet Motor Design, New York: McGraw-Hill, 1994.

[34] S. Sudhoff, Power Magnetic Devices: A Multi-Objective Design Approach, Hoboken: Wiley, 2014.

[35] M. L. Bash, J. M. Williams and S. D. Pekarek, "Incorporatin Motion in Mesh-Based Magnetic Equivalent Circuits," *IEEE Transactions on Energy Conversion,* vol. 25, no. 2, pp. 329-338, 2010.

[36] E. Severson, R. Nilssen, T. Undeland and N. Mohan, "Magnetic Equivalent Circuit Modeling of the AC Homopolar Machine for Flywheel Energy Storage," *IEEE Transactions on Energy Conversion,* vol. 30, no. 4, pp. 1670-1678, 2015.

[37] C. Chillet and J.-Y. Voyant, "Design-Oriented Analytical Study of a Linear Electromagnetic Actuator by Means of a Reluctance Network," *IEEE Transactions on Magnetics,* vol. 37, no. 4, pp. 3004-3011, 2001.

[38] M. A. Batdorff and J. H. Lumkes, "High-Fidelity Magnetic Equivalent Circuit Model for an Axisymmetric Electromagnetic Actuator," *IEEE Transactions on Magnetics,* vol. 45, no. 8, pp. 3064-3072, 2009.

[39] G. M. Shane and S. D. Sudhoff, "Refinements in Anhysteretic Characterization and Permeability Modeling," *IEEE Transactions on Magnetics,* vol. 46, no. 11, pp. 3834-3843, 2010.

[40] ANSYS, Inc., *Inductance in Terms of Flux Linkage and Currents,* 2017.

[41] B.-H. Cho, H.-W. Lee and J.-S. Oh, "Estimation technique of air content in automatic transmission fluid by measuring effective bulk modulus," *International Journal of Automotive Technology,* vol. 2, no. 3, pp. 57-61, 2002.

[42] K. Deb, A. Pratap, S. Agarwal and T. A. M. T. Meyarivan, "A fast and elitist multiobjective genetic algorithm: NSGA-II," *IEEE Transactions on Evolutionary Computation,* vol. 6, no. 2, pp. 182-197, 2002.

[43] T. Sullivan, *Multi-Domain Multi-Objective Optimization of Mechanisms: A General Method with Two Case Studies,* Minneapolis: University of Minnesota, 2013.

[44] A. J. Chipperfield, P. J. Fleming and C. M. Fonseca, "Genetic Algorithm Tools for Control Systems Engineering," in *Adaptive Computing in Engineering Design and Control*, Plymouth, 1994.

[45] C.-Y. Lin and P. Hajela, "Genetic Algorithms in Optimization Problems with Discrete and Integer Design Variables," *Engineering Optimization,* vol. 19, pp. 309-327, 1992.

[46] Advanced Motion Controls, "DPEANIU-015S400," 2017. [Online]. Available: https://www.a-m-c.com/products/?page=product&cid=root&id=DPEANIU-015S400. [Accessed 3 May 2017].

[47] Hawe Hydraulik SE, *Check valve type RC - Product documentation,* 2016.

[48] A. L. Knutson and J. D. Van de Ven, "Modelling and experimental validation of the displacement of a check valve in a hydraulic piston pump," *International Journal of Fluid Power,* vol. 17, no. 2, pp. 114-124, 2016.

[49] C. Cadou and B. Zhang, "Performance Modeling of a Piezo-hydraulic Actuator," *J. Intelligent Material Systems and Structures,* vol. 14, pp. 149-160, 2003.

[50] H2W Technologies, Inc., "Non-Comm DC Voice Coil Linear Actuator - NCM08-35-450-3LB," 2017. [Online]. Available: https://www.h2wtech.com/product/voice-coil-actuators/NCM08-35-450-3LB. [Accessed 3 May 2017].

7 Appendix

A – Pump Manifold Drawing

This drawing documents the pump manifold designed and machined in-house. It contains a cylinder inlet, two BSPP-tapped holes for the inlet and delivery check vales, and an NPT-tapped hole for the pressure transducer. Two manifolds were made, one of which with inlet and delivery BSPP threads switched.

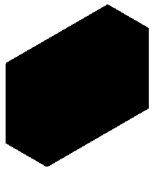

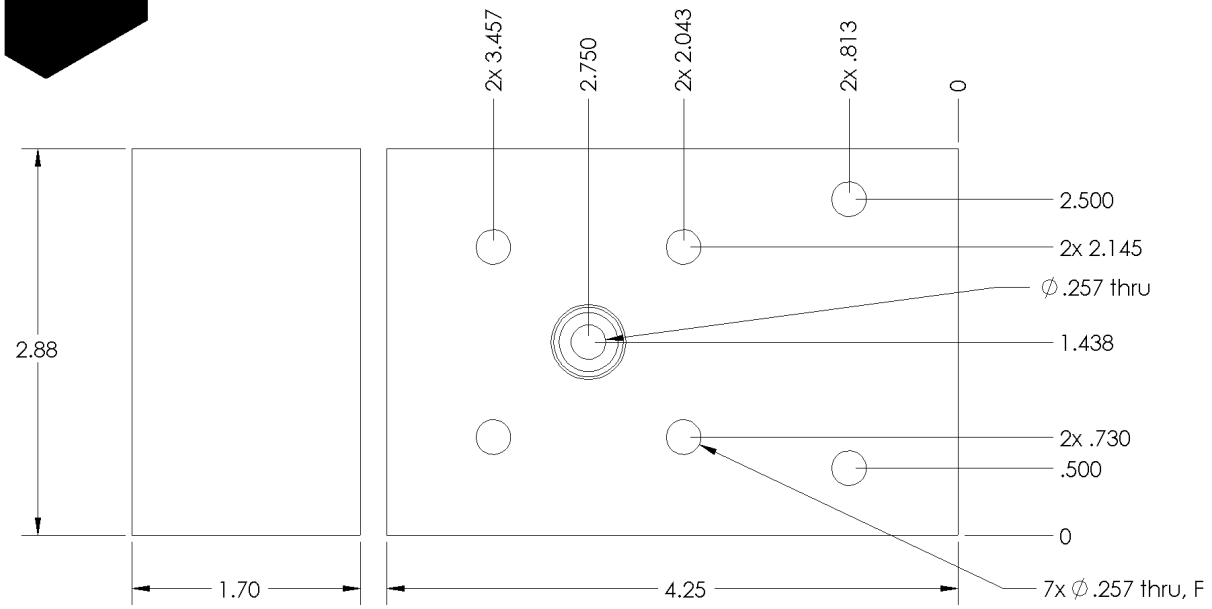

		UNLESS OTHERWISE SPECIFIED:		NAME	DATE
		DIMENSIONS ARE IN INCHES TOLERANCES: FRACTIONAL ± ANGULAR: MACH ± BEND ± TWO PLACE DECIMAL ± THREE PLACE DECIMAL ±	DRAWN		
			CHECKED		
			ENG APPR.		
			MFG APPR.		
		INTERPRET GEOMETRIC TOLERANCING PER:	Q.A.		
		MATERIAL	COMMENTS:		
NEXT ASSY	USED ON	FINISH			
APPLICATION		DO NOT SCALE DRAWING			

TITLE:
Manifold: Default
Qty 1
See reverse for tap directions

SIZE	DWG. NO.	REV
A	Man_Def	
SCALE: 1:1	WEIGHT:	SHEET 1 OF 2

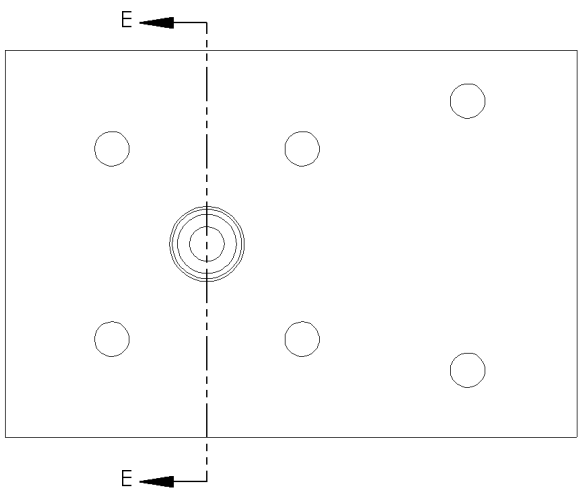

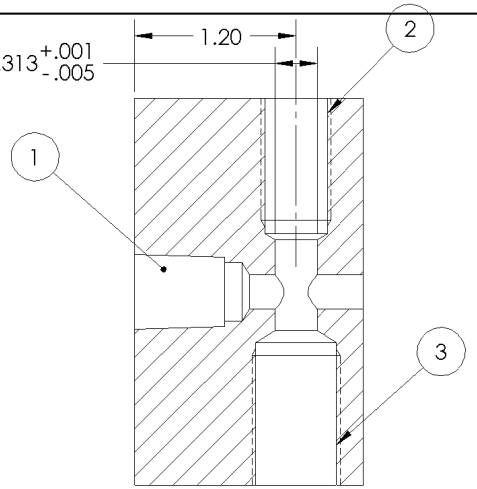

SECTION E-E
SCALE 1 : 1

Hole Num	Nom Size	Tap Drill Size	Drill Depth	Tap Depth
1	1/4" NPT	7/16"	0.93" +0.00/-0.01	0.67" (or 2/3 tap thread length)
2	G 1/4 (BSPP)	29/64"	1.144" +0.000/-0.005	0.91" +0.01/-0.00
3	G 3/8 (BSPP)	19/32"	1.243" +0.000/-0.005	0.96" +0.01/-0.00

NEXT ASSY | USED ON

APPLICATION

UNLESS OTHERWISE SPECIFIED:

DIMENSIONS ARE IN INCHES
TOLERANCES:
FRACTIONAL ±
ANGULAR: MACH ± BEND ±
TWO PLACE DECIMAL ±
THREE PLACE DECIMAL ±

INTERPRET GEOMETRIC TOLERANCING PER:

MATERIAL

FINISH

DO NOT SCALE DRAWING

	NAME	DATE
DRAWN		
CHECKED		
ENG APPR.		
MFG APPR.		
Q.A.		

COMMENTS:

TITLE:

For reverse manifold, switch G 1/4 and G 3/8 holes

SIZE A | DWG. NO. Man_Def | REV

SCALE: 1:2 | WEIGHT: | SHEET 2 OF 2

B – Cylinder Housing Drawing

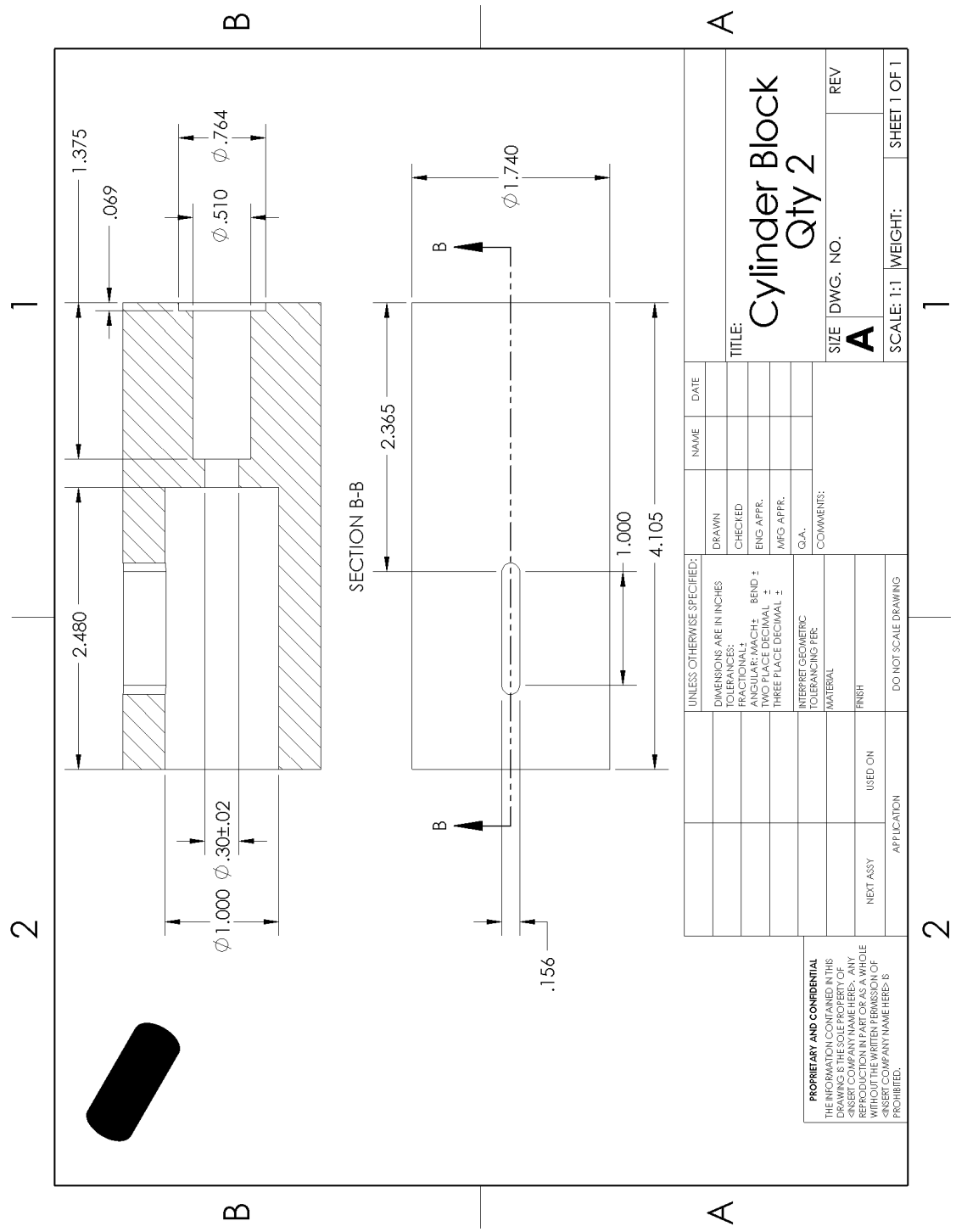

C – Spring Retainer

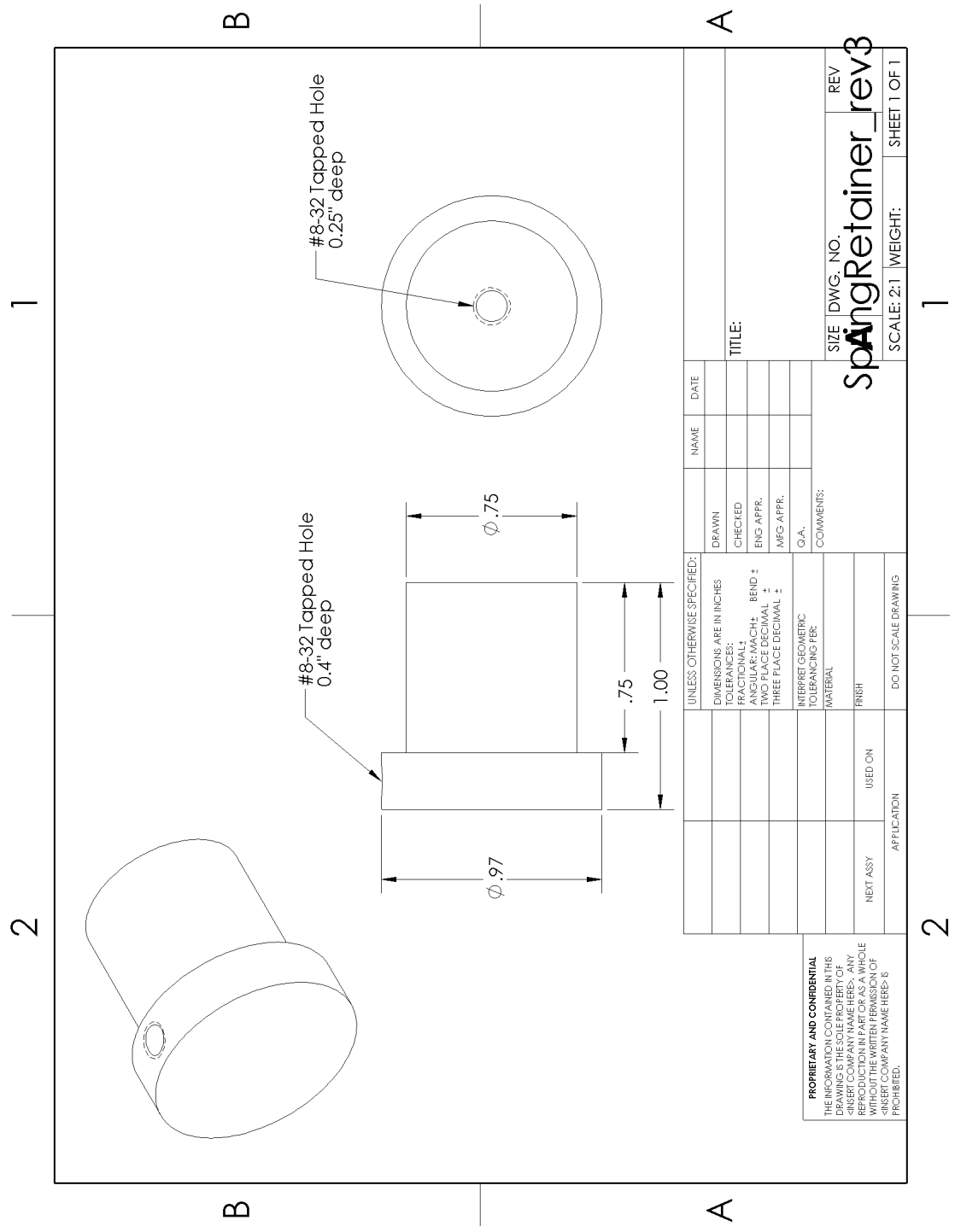

D – Servo Drive Schematic

The servo drive uses a single-phase, 208 VAC input from the wall outlet. Low voltage supply comes from a 24 VDC Extech supply. The shunt resistor is a 100 Ω, 220 W power resistor in series with a time delay 5 A fuse. The drive outputs motor power on A and B (C is disconnected). Communication with the computer occurs through the USB interface.

To minimize the transmission of 20 kHz PWM switching noise from the drive onto the motor leads and low voltage supply leads, it is important that a common ground be used in a star configuration. Shielded wires are used on motor and low voltage supplies and grounded at the drive. A high gage grounding wire connects the table ground and motor chassis to the bus bar within the HV enclosure. All grounds trace their way back to the PE ground through the outlet.

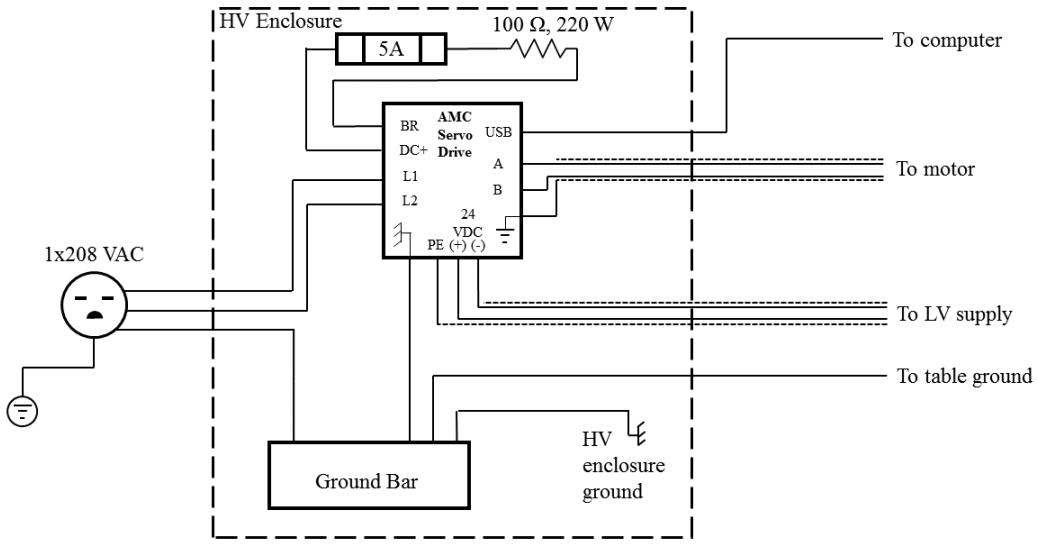

E – Stator Drawing

This drawing documents the custom stator sections designed and machined in-house. They were designed for machining with a 3-axis Haas CNC mill, with finishing work on a manual lathe. Three of the sections used thru-holes on the bolt circle, while the fourth had a ¼”-20 tap to allow the sections to be bolted together.

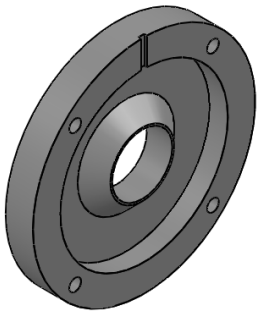

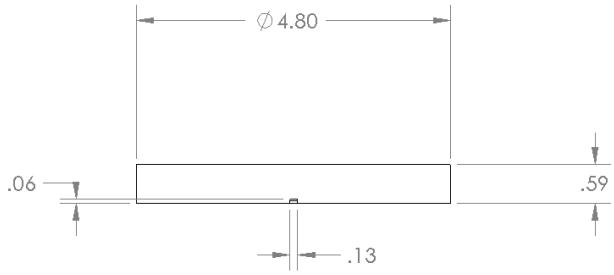

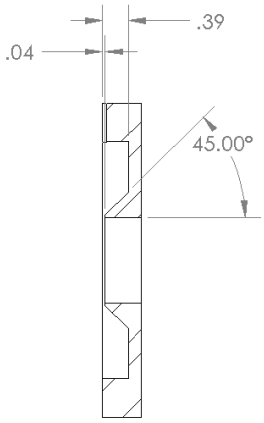

SECTION A-A

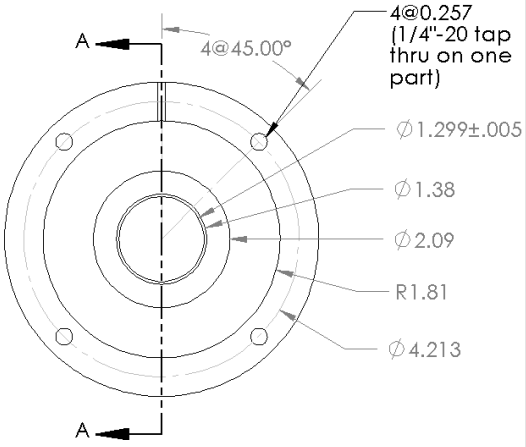

		DIMENSIONS ARE IN INCHES TOLERANCES: FRACTIONAL ± ANGULAR: MACH ± BEND ± TWO PLACE DECIMAL ±0.01 THREE PLACE DECIMAL ±0.001		NAME	DATE
			DRAWN		
			CHECKED		
			ENG APPR.		
			MFG APPR.		
		MATERIAL: 1018 Steel	Q.A.		
			COMMENTS:		
NEXT ASSY	USED ON	FINISH			
APPLICATION		DO NOT SCALE DRAWING			

PROPRIETARY AND CONFIDENTIAL

THE INFORMATION CONTAINED IN THIS DRAWING IS THE SOLE PROPERTY OF <COMPANY NAME>. ANY REPRODUCTION IN PART OR AS A WHOLE WITHOUT THE WRITTEN PERMISSION OF <COMPANY NAME> IS PROHIBITED.

Qty: 4
3 with clearance holes, 1 with tapped holes

SIZE	DWG. NO.	REV.
A	StatorSection	
SCALE:1:2	WEIGHT:	SHEET 1 OF 1

F – Bearing Housing

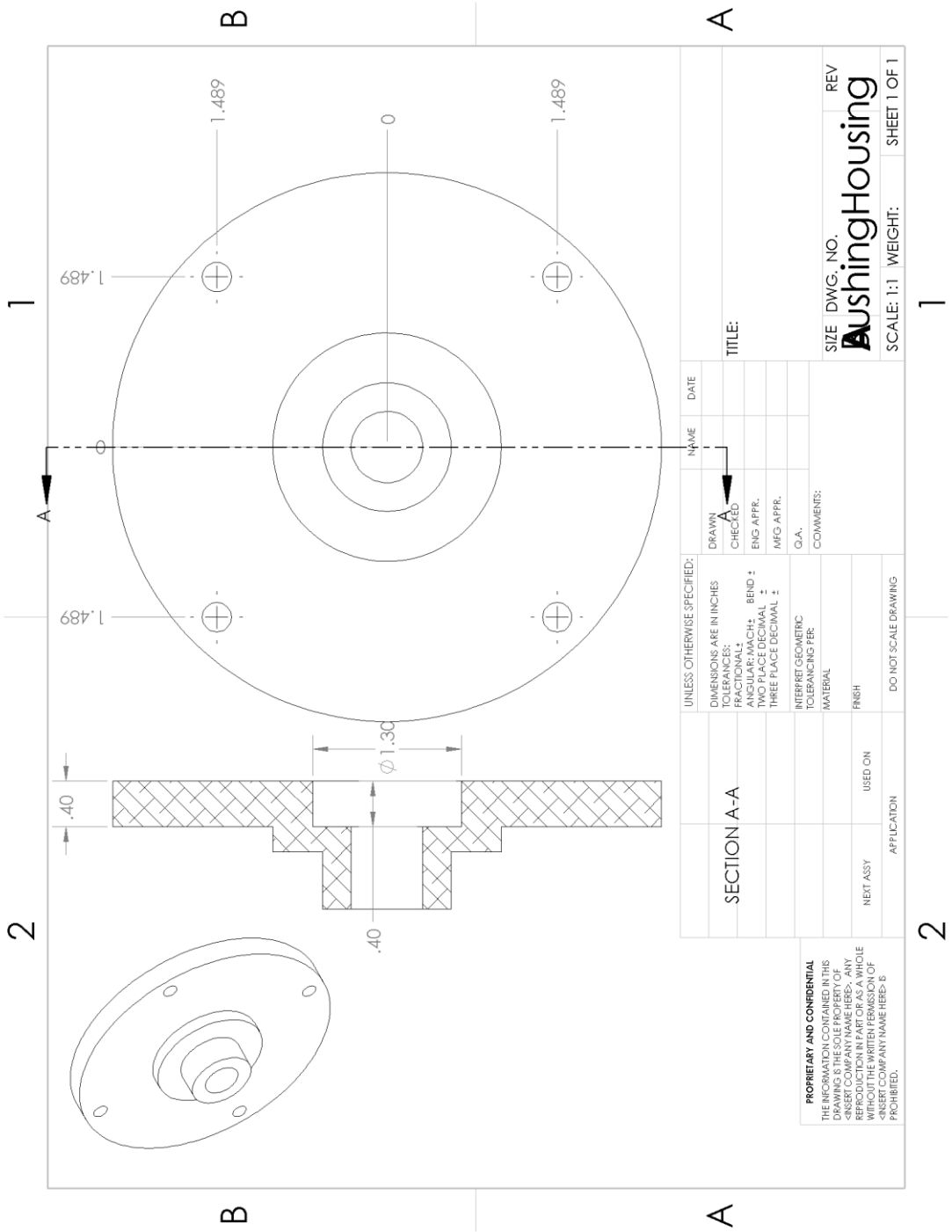

G – Motor Shaft